Preface

Special Issue on Design, Fabrication and Economy of Welded Structures

This special issue covers the papers presented at a joint seminar organized by members of the International Institute of Welding, Commission XV from Hungary, Korea, and Japan to exchange knowledge of the design, manufacturing, and maintenance of welded steel structures in mechanics and civil engineering. Research initiatives in these countries are introduced to foster strong linkages between them. This special issue provides a wide range of case studies, empirical research, and professional analysis based on the study of relevant sources to aid academic teachers, researchers, and professionals working in structural design. The special issue is unique in that it does not focus on a specific theme in structural engineering. Instead, it offers insights into the world and practices of co-disciplines that are inextricably related to structural engineering.

This edition contains articles from the field of contactless strain measurement at steel structures "Monitoring of strains and deflections of steel cantilever using a contactless measurement method", optimization of wheel column "Optimal Design of Wind Wheel Column", experimental measurements of steel elements in fire "Experimental validation of heat propagation: results of the numerical modeling for the real scale steel structural element and different assigned models subjected to a simulated fire", a new heat input model "Proposal of Heat Input Model for Heating Correction on Welded Steel Structural Members", design of stiffening plates "Optimized Trapezoidal Stiffened Plates under Uniaxial Compression and Suddenly Applied Pressure", effect of heating on high strength bolts "An Investigation on Axial Force Reduction of High-strength Bolts by Induction Heating for Paint-coating Removal", the steel cross-section comparisons at higher temperatures, "Comparison of different leg cross sections in case of fire," and damage identification "Improving optimization-based inverse analysis using direct inverse maps: A dynamic damage identification case study," fatigue tests on pipelines "Full-scale Fatigue and Burst Tests on Notched Pipeline Girth Welds under Complex Loading Conditions".

We are grateful to all of the writers and co-authors for their dedication to developing contributions for this special issue and sharing their findings with the journal. Last but not least, we would like to thank the editorial board of the journal Acta Polytechnica Hungarica, particularly Ms. Anikó Szakál, for technically preparing and managing this issue, as well as Prof. Imre J. Rudas and Prof. Levente Kovács, for their help in publishing this Special Issue.

Károly Jármai

Guest Editor

Monitoring of Strains and Deflections of a Steel Cantilever, using a Contactless Measurement Method

Ladislav Galdun [1, 2]**, Mohamad Al Ali** [3*]**, Peter Platko** [3]**, Stanislav Kmeť** [3⚕]**, Vincent Kvočák** [3]**, Rastislav Varga** [1, 2]

[1] RVmagnetics a.s., Nemcovej 30, 04001, Košice, Slovakia
galdun@rvmagnetics.com, varga@rvmagnetics.com

[2] Center for Progressive Materials, Technology and Innovation Park, Pavol Jozef Šafárik University in Košice, Tr. SNP 1, 04011 Košice, Slovakia

[3] Institute of Structural and Transportation Engineering, Faculty of Civil Engineering, Technical University of Košice,
Vysokoškolská 4, 04200, Košice, Slovakia
mohamad.alali@tuke.sk [*], peter.platko@tuke.sk, stanislav.kmet@tuke.sk

Abstract: The aim of the experimental and analytical work was to monitor and analyze the strains and deflections of steel cantilevers using a bistable glass-coated microwire, as a contactless measurement method. For verification and comparison, the results obtained from the applied bistable microwire ($Fe_{75}Si_9B_{10}P_5Tb_1$), the results of a standard resistance strain gauge and dial indicator were used. Since the microwire used, has a metallic (magnetic) core, verifying the possibility of separating the influence of the parasitic external magnetic field from the measured deformations, was the first goal of the implementation of the bending test on steel cantilevers. Another goal was to find a relationship between the switching field of the microwire and the strains measured by the strain gauge, depending on the applied load during the experimental test. Both goals were achieved within this research.

Keywords: Contactless; Bistable microwire; Magnetic field; Strain; Strain gauge

1   Introduction

Experimental tests with the application of resistance strain gauges, dial indicators and similar conventional sensors are used for monitoring and recording the stress state and strain development in tested structural members, as well as to support the results of theoretical and numerical analyzes of such members [1-5]. During experimental tests and loading processes, conventional sensors must be

permanently connected to computers and evaluation devices using various types of data acquisition systems - data buses [6-9]. This fact limits the possibility of using strain gauges and dial indicators only for laboratory conditions. The need to protect sensing technologies from weather effects have limited their outdoor use for monitoring existing structural members and structures. In addition, the necessity of permanently connecting the recording devices until the end of the measurement process makes it impossible to use these devices simultaneously in another experimental investigation.

Since contactless methods allow monitoring and recording the stress state of the investigated members without the need for their permanent connection to recording devices, these methods are becoming more convenient and flexible for structural engineers and researchers. One of the possibilities of contactless measurement is the use of bistable glass-coated microwires [10-12]. Due to their magnetic properties, it is possible to perform contactless measurements of strains by means of an induction method via a sensing unit. The microwire, as a passive part of the system, can be placed at any location; moreover, it can even be embedded inside the material of the tested member [13-15].

The mentioned disadvantages of standard strain gauges can be avoided by using a bistable microwire, as the presented research shows. On the other hand, the analyzes presented in this work represent a new concept of contactless strain measurement applied to a steel (ferromagnetic) structural member. As stated in the paper, this method allows for separation of the influence of parasitic magnetic fields that can occur when measuring magnetic materials.

2   Applied Microwire and Method of Analysis

In the performed experiment, a glass-coated microwire $Fe_{75}Si_9B_{10}P_5Tb_1$ with a metal core of 10 µm in diameter and a total diameter of 30 µm was used. Figure 1 shows a typical micrograph of a microwire with a partially removed glass coating.
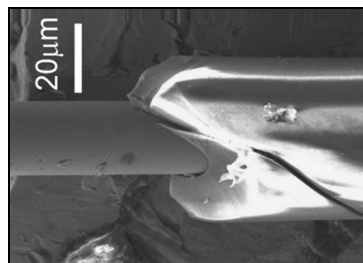

Figure 1

Micrographic configuration of a glass-coated microwire

2.1   Microwire Response Measurement

The magnetic response of the bistable glass-coated microwire is given by the switching field H_{SW}. The induction method was used to measure this magnetic response. A typical square magnetic hysteresis loop and switching field H_{SW} is illustrated in Figure 2, where M_S is the saturation magnetization and H is the magnetic field.
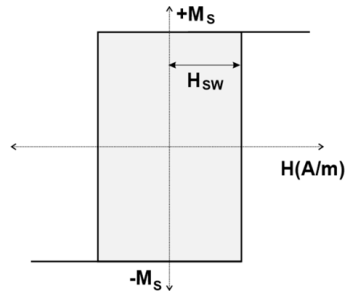

Figure 2
Magnetic hysteresis loop with switching field H_{SW}

Monitoring the response of the microwire was realized using a sensing system placed above the microwire. The 70x20x20 mm sensing system has two tapes to create a gap of about 2 mm between the sensing system and the microwire, as shown in Figure 3. The height of the tape depends on the required height of the gap and the type of microwire used. So, the distance between the sensing system and the microwire can be increased to about 50 mm.
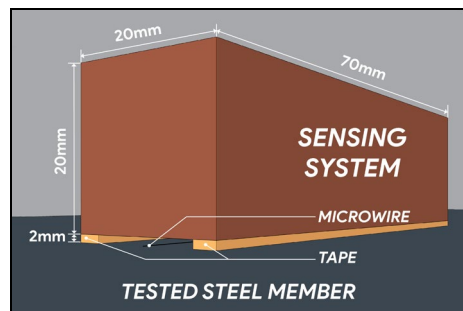

Figure 3
Illustration of the sensing system

A pair of coils is integrated in the sensing system. The first of these is the excitation coil. This coil generates a magnetic field for the magnetization reversal process of the microwire. To achieve the magnetization reversal process, the excitation coil was powered by a triangular AC voltage with a frequency of 100 Hz and 7.44 V amplitude. The second one is the pickup coil, in which the

magnetization reversal process of the microwire is detected and transformed into the sensing signal. Figure 4 presents the above-mentioned magnetization reversal process. The yellow lines represent the excitation signal, while the sensing signal with two maximum and minimum peaks is blue. t_1 and t_2 are the time occurrence of positive and negative switching between two states of magnetization $\pm M_S$ (the time of the magnetization reversal of the microwire).
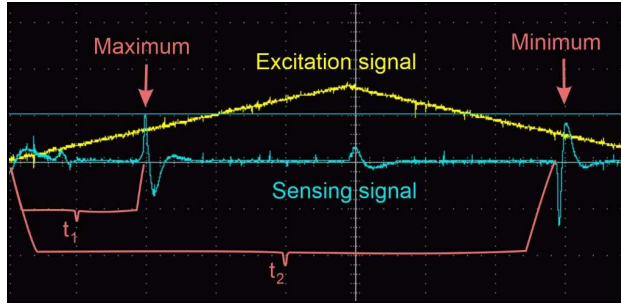

Figure 4
Graphical visualization of the excitation and sensing signal

2.2   Application of the Induction Method

As mentioned in the previous chapter, a triangular AC voltage was used to create the magnetic field. The obtained switching field H_{SW} is commensurable to the stress caused by the applied load, under conditions of constant temperature and excitation field frequency [11]:

$$H_{SW} = \frac{\sqrt{A \cdot \lambda_S \cdot \sigma}}{\mu_0 \cdot M_S} \tag{1}$$

where: A is the exchange constant

λ_S is the saturation magnetostriction

σ is the stress caused by the applied load

μ_0 is the vacuum permeability

M_S is the saturation magnetization

Because of the positive magnetostriction of the metallic core, the microwire is sensitive to the strain ε, transmitted from the applied load and corresponding stress. The strain follows Hooke's law. It follows that the switching field is proportional to the relative elongation of the tested member, to which the microwire is fixed (glued). The switching field H_{SW} is also proportional to the switching time t_{SW} (see Figure 4), which is the magnetization reversal time of the microwire:

$$t_{\text{SW}} = t_1 + t_2 \qquad\qquad\qquad\qquad\qquad\qquad\qquad\qquad (2)$$

Equation 2 is also applicable in the case when an additional parasitic external magnetic field is present. The external magnetic field does not influence the width of the hysteresis loop (H_{SW}) and, thus, the t'_{SW} (Equation 3). On the other hand, the position of the hysteresis loop is shifted depending on the direction of the magnetic field, Figure 5 [12]. In other words, when an external magnetic field is present, the center of the hysteresis loop (Figure 2) shifts, as shown in Figure 5.
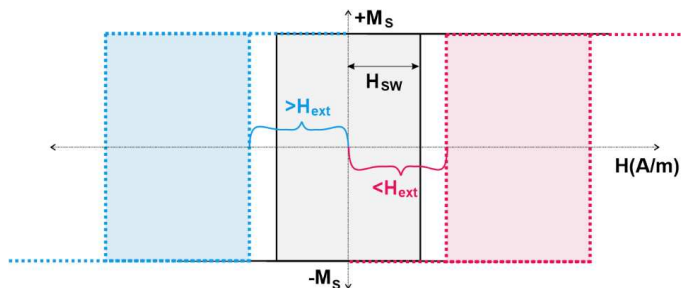

Figure 5
The shift of the hysteresis loop caused by parasitic external magnetic field

This phenomenon provides the possibility of identifying the direction and amplitude of the external magnetic field. The difference in the switching time t'_{SW}, which is proportional to the external magnetic field, can be achieved using Equation 3 [12]:

$$H_{\text{ext}} \approx t'_{\text{SW}} = t_2 - t_1 \qquad\qquad\qquad\qquad\qquad\qquad\qquad (3)$$

According to the presented approach, it can be concluded that it is possible to separate the magnetic influence of the environment (parasitic external magnetic field) from the required measurements, which is very necessary when testing magnetic (steel) material.

3 Preparation for the Experimental Test

3.1 Production of Experimental Test Components

Three specimens made from sheet material of low-carbon steel S 235 were fabricated to perform the bending test of the cantilever. The specimens have a cross-section of 80x3 mm and a length of 600 mm. A hole was drilled on one side of the specimens to fix the pre-prepared loading mechanism. Figure 6 shows the steel specimen prepared for the test, including the place of the cantilever fixing,

the position of sensing devices and the location of the loading mechanism connection (hole).

Figure 6
Steel specimen prepared for bending test

A special loading mechanism was designed and produced for experimental tests, as shown in Figure 7. This mechanism, made of galvanized steel, consists of two parts:

- Load carrier, designed to ensure the vertical action of the force during the cantilever deflection process, thanks to the hinge connection that allows the system to rotate. The load carrier weighs about 787 g

- Weights with dimensions 80x84x5 mm, having holes in the middle. The length of approximately 84 mm has been adjusted so that each weight had a mass of 250 g (± 2 g). The holes allow for easy increase and/or decrease of load size.

Figure 7
Loading mechanism - load carrier and loading weights

3.2 Preparation of Supporting Materials

The preparatory works included numerical analysis to estimate the theoretical elastic resistance moment of the steel cantilever, strains and deflections. A schematic representation of the cantilever with the measurement locations of strains (x_s), deflections (x_f) and the position of the applied force (x_f) is in Figure 8.

The used steel has nominal values of material properties: f_y = 235 MPa (Yield stress), f_u = 360 MPa (Ultimate stress) and Young's modulus E = 210 000 MPa [16] [17].
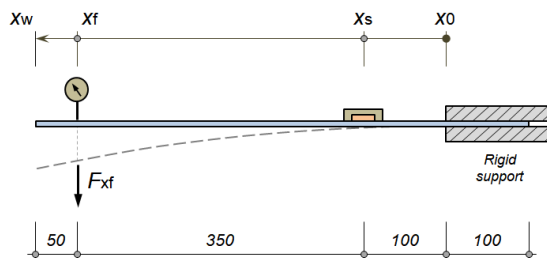

Figure 8
Schematic representation of the cantilever

According to the above-mentioned material properties and Figure 8, the cross-sectional elastic resistance moment was determined at the fixed point (x_0) and had the value: $M_{el,Rd}$ = 28.20 Nm. This moment was achieved from the applied force $F_{xf,max}$ = 57.43 N. At this load level, the deflection in the position (x_w) had a value of 57.74 mm.

To ensure the elastic behavior of the cantilever, the maximum load for the experimental test was set to about 70% of the theoretically determined maximum load $F_{xf,max}$, i.e., $F_{xf,70}$ = 40.20 N. According to $F_{xf,70}$, a sequence of load steps was created and divided into 15 load cases (LC) as shown in table 1. Table 1 also contains the calculated values of the applied force, corresponding stress and strain for each load case.

Table 1
Load cases with relevant forces, stresses and strains

Load case	Acting force F_{xf} [N]	Normal stress σ_{x0} [kPa]	Strain ε_{xs} [%]
LC1 = G	-	19625	0.006
LC2 = $G + F_0$	7.87	49138	0.017
LC3 = $G + F_0 + F_1$	10.37	58513	0.020
LC4 = $G + F_0 + F_2$	12.87	67888	0.024
LC5 = $G + F_0 + F_3$	15.37	77263	0.027
LC6 = $G + F_0 + F_4$	17.87	86638	0.031
LC7 = $G + F_0 + F_5$	20.37	96013	0.034
LC8 = $G + F_0 + F_6$	22.87	105388	0.038
LC9 = $G + F_0 + F_7$	25.37	114763	0.041
LC10 = $G + F_0 + F_8$	27.87	124138	0.045
LC11 = $G + F_0 + F_9$	30.37	133513	0.048
LC12 = $G + F_0 + F_{10}$	32.87	142888	0.052

LC13 = $G + F_0 + F_{11}$	35.37	152263	0.055
LC14 = $G + F_0 + F_{12}$	37.87	161638	0.059
LC15 = $G + F_0 + F_{13}$	40.37	171013	0.062

Where: G is the dead load of the cantilever, F_0 is the weight of the load carrier, F_i is the applied force achieved by gradually adding weights in the respective load case ($i = 1$ to 13).

4   Implementation of the Bending Test

In the beginning, bistable glass-coated microwire $Fe_{75}Si_9B_{10}P_5Tb_1$ was fixed on the surface of the steel specimen using glue X60 based on methyl-methacrylate. Strain gauge FLAB-6-11 was glued, using the same type of glue, close to the microwire to obtain comparable results. Moreover, a dial indicator (DI) was added to the measurement system, near the free end of the cantilever, to monitor the deflections. The layout of the test and the locations of the measuring devices are illustrated in Figure 9.
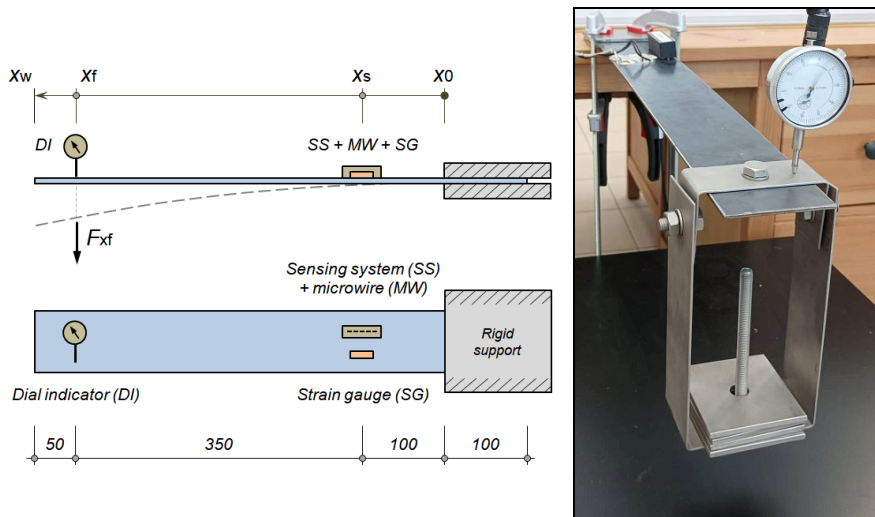

Figure 9
General view of the test arrangement

The switching time was obtained by placing the sensing system (SS), connected to an oscilloscope, over the microwire (MW) to monitor its response (Figure 3). Then the sensing signal was displayed on the oscilloscope (Figure 4) in the shape of minimum and maximum peaks. After that, the position of the peaks was determined manually, taking into account the time range of the oscilloscope.

The strains were measured by connecting the strain gauge to a computer via calibrated data-bus MX1615B. A quarter-bridge was used to connect the strain gauge (SG) to the data-bus. Catman Easy V5.1.3 software was used for data recording and evaluation.

The strain, deflection and switching time measuring devices were set to zero before the load carrier was installed, and this state was considered the first load case. As a second load case, after installing the load carrier, a weight of 787 g was set, and the changes in strain, deflection and microwire switching time values were recorded. Then the load was gradually increased up to 4037 g by sequentially adding 13 weights, see table 1, while simultaneously recording the changes in strain, deflection and switching time of the microwire step by step. After reaching a weight of 4037 g, the test continued with the unloading process by sequentially removing the 13 weights, so the load returned to a weight of 787 g (load case no. 2).

The load was applied only within the elastic zone of the used steel, i.e., the plasticization and hardening zones with plastic strains were not reached.

5   Results and Discussion

The measured output data from the experimental test during the loading and unloading process are presented in Figures 10, 11 and 12. The relationship between the applied forces and deflections, in relation to individual load cases, is given by Figure 10. Figure 11 illustrates the development of the strains, and Figure 12 shows the variation of the microwire switching time.

As shown in the graphs, the strains (measured by strain gauge) and deflections (measured by dial indicator) have a linear shape, which ensures that the measurement was carried out within the elastic zone of the material used (S 235). The switching time of the microwire obtained by the contactless measurement method has a quasi-linear character in a similar shape, compared to the deflections and strains. At the maximum load of 40.37 N (load case no. 15), the deflection reached a value of 41.7 mm at a measured strain value of 0.065% and the maximum change of the switching time was 0.4 ms.

Using the results to determine the relationship between the strains and the switching times, the correlation for linear fit was determined as $y=0.14x-1.38$ (Fig. 13). The black spots are experimental results and the orange line is the correlation between switching time (X-axis) and strains (Y-axis).

As part of their previous experimental research, the authors already proved the possibility of using the above-mentioned contactless method for measuring the strains of a non-magnetic material via a bistable microwire [18]. The possibility of

using this method for magnetic material was experimentally investigated and presented in this paper.
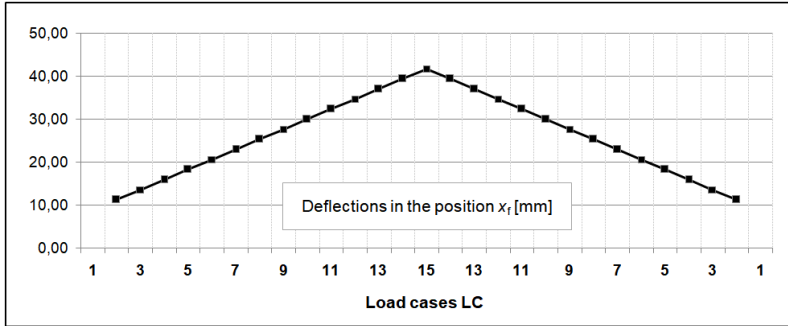

Figure 10
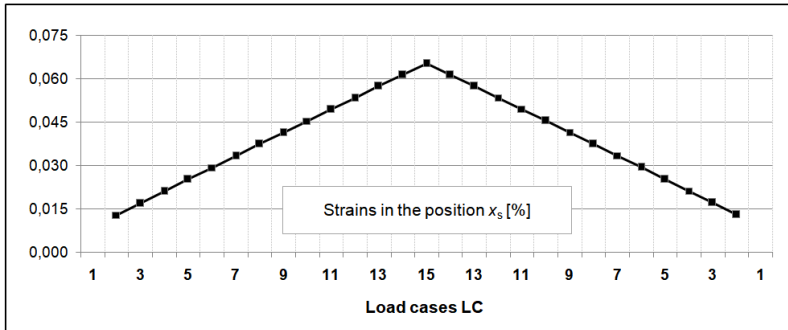Relationship between the applied forces and deflections

Figure 11
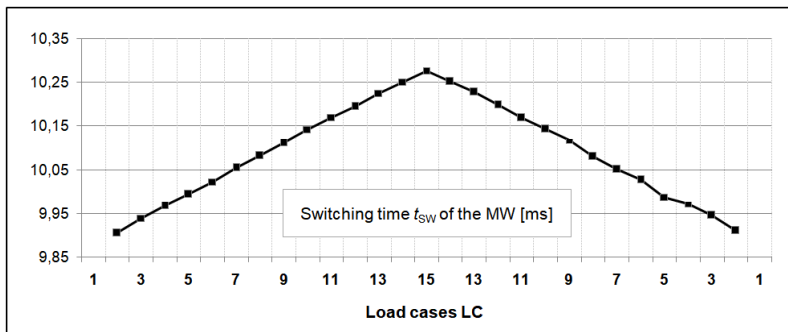Relationship between the applied forces and strains

Figure 12
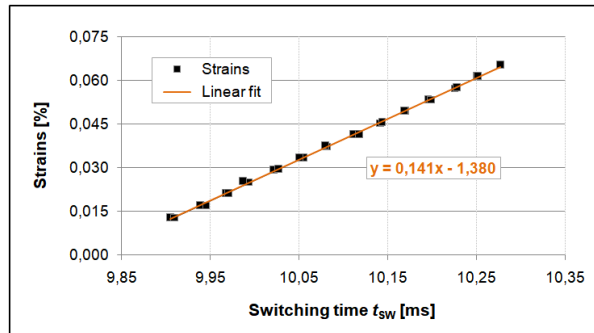Relationship between the applied forces and switching time

Figure 13
Dependence of switching time on strains

Conclusions

As presented and proven in this paper, thanks to the magnetic bistability of the microwire, it was possible to perform a contactless measurement, on a metal member with magnetic properties.

The obtained results also demonstrated a comparable character in the behavior of the applied sensing devices (strain gauge, dial indicator and microwire) during the loading and unloading process. Furthermore, due to the linear nature of the results, the relationship between strains and switching time for this relevant case was determined, as shown in Figure 13.

Taking into account the above-mentioned results, glass-coated bistable microwires can be considered as suitable candidates for contactless measurement of elastic strains, when investigating materials of ferromagnetic character.

After achieving adequate results in the elastic zone of the used material, future research work will be focused on the application of glass-coated bistable microwires, to measure strains within the elasto-plastic and hardening zones of the various materials that make up structural members.

Acknowledgement

References

[1]   Wang B., Ke X., Du K., Bi X., Hao P., Zhou C., A novel strain field reconstruction method for test monitoring, International Journal of Mechanical Sciences, 243 (2023)

[2]   Zhou C., Xia M., Xu Z., Design and optimization of a quadrupedal dynamic disturbance force measurement platform using strain gauges, Mechanical Systems and Signal Processing, 188 (2023)

[3] Mokhtari E., Palermo M., Laghi V., Incerti A., Mazzotti C., Silvestri S., Quasi-static cyclic tests on a half-scaled two-storey steel frame equipped with Crescent Shaped Braces at both storeys: Experimental vs. numerical response, Journal of Building Engineering, 62 (2022)

[4] Hu X., Li Y., Zhang H., Yu Y., Kang Z., Design and Application of Automatic Calibration Device for Multi-Channel Resistance Strain Gauge Indicator, Journal of Physics: Conference Series, 2113/1 (2021)

[5] Daou A., Chehab G., Saad G., Hamad B., Experimental and numerical investigations of reinforced concrete columns confined internally with biaxial geogrids, Construction and Building Materials, 263 (2020)

[6] Meyland M. J., Eriksen R. N. W., Nielsen J. H., A modified split-Hopkinson pressure bar setup enabling stereo digital image correlation measurements for flexural testing, International Journal of Impact Engineering, 173 (2023)

[7] Gioiosa A., Bonventre R., Donati S., Flumerfelt E., Horton-Smith G., Morescalchi L., O'Dell V., Pedreschi E., Pezzullo G., Spinella F., Uplegger L., Rivera R. A., Slow control and data acquisition systems in the Mu2e experiment, Proceedings of Science, 380 (2022)

[8] Yang T., Wang W., Huang Y., Jiang X., Zhao X., Accurate Monitoring of Small Strain for Timbre Recognition via Ductile Fragmentation of Functionalized Graphene Multilayers, ACS Applied Materials and Interfaces, 12/51 (2020)

[9] Doggett W., Vazquez S., Architecture for real-time interpretation and visualization of structural sensor data in a laboratory environment, AIAA/IEEE Digital Avionics Systems Conference - Proceedings, 2 (2000), pp. 6.D.2-1-6.D.2-8

[10] Praslicka D., Blazek J., Smelko M., Hudák J., Cverha A., Mikita I., Varga R., Zhukov R. A., Possibilities of measuring stress and health monitoring in materials using contact-less sensor based on magnetic microwires, IEEE Trans. Magn. 49 (2013) 128-131

[11] Varga R., Gamcova J., Klein P., Kovac J., Zhukov A., Tailoring the switching field dependence on external parameters in magnetic microwires, IEEE Trans. Magn. 49 (2013) 30

[12] Jacko P., Jurč R., Galdun L., Hvizdoš L., Kováč D., Varga R., Linear position sensor using magnetically bistable microwire. Sens. Actuators A Phys. (2023), 349, 114017

[13] Kohan M., Varga R., Hudak R., Schnitzer M., Ferencik N., Dancakova G., Lancos S., Anonymous Pilot study: Measurement of mechanical load using a glass-coated microwire for implantology applications. SAMI 2021 - IEEE 19th World Symposium on Applied Machine Intelligence and Informatics, Proceedings (2021), 267-272

[14]   Olivera J., Aparicio S., Hernández M. G., Zhukov A., Varga R., Campusano M., Echavarria E., Velayos J. J. A., Microwire-based sensor array for measuring wheel loads of vehicles. Sensors 2019, 19, (21), 4658

[15]   Sabol R., Klein P., Ryba T., Hvizdos L., Varga R., Rovnak M., Sulla I., Mudronova D., Galik J., Polacek I., Zivcak J, Hudak R., Novel Applications of Bistable Magnetic Microwires. Acta Phys. Pol. 131 (4): 1150-1152

[16]   STN EN 1993-1-1 Eurocode 3: Design of steel structures, Part 1-1: General rules and rules for buildings, SÚTN, 2006

[17]   STN EN 10025-2:2019. Hot rolled products of structural steels. Part 2: Technical delivery conditions for non-alloy structural steels

[18]   Al Ali M., Platko P., Bajzecerova V., Kmet S., Galdun L., Spegarova A., Varga R., Monitoring the strain of beech plywood using a bistable magnetic microwire, Sens. Actuators A: Phys. 326 (2021) 112726

Optimized Trapezoidal Stiffened Plates under Uniaxial Compression with a Sudden, Rapidly Applied Pressure

Sándor Szirbik

Institute of Applied Mechanics, University of Miskolc, H-3515 Miskolc, Hungary, sandor.szirbik@uni-miskolc.hu

Zoltán Virág

Institute of Mining and Geotechnical Engineering, University of Miskolc, H-3515 Miskolc, Hungary, zoltan.virag@uni-miskolc.hu

Abstract: This paper is devoted to the forced vibration analysis of optimized trapezoidal stiffened plates with simple supported conditions on the four edges of the base plate. The purpose of the finite element analysis is to investigate the transient forced vibrations of stiffened structures subjected to uniaxial compression due to the reason of rapidly applied pressure over their base plates, thereby identifying potentially dangerous cases and minimizing the possibility of failure. In this study, the numerical analysis is performed for such a design of this kind of welded plates which have already been optimized for lateral pressure and uniaxial compression as static loadings. The objective function of the optimization to be minimized performed with the Excel Solver program is the cost function which contains material and fabrication costs for Gas Metal Arc Welding (GMAW) welding technology. The eigenvalue extraction is used to calculate the natural frequencies and mode shapes based on the Lanczos iteration method then the transient response is determined using the modal superposition method from the first few mode shapes. The welded structure is made of two grades of steel, which are described with different yield stress while all other material properties of steel remain the same.

Keywords: trapezoidal stiffener; FEA; modal analysis; transient forced vibration

1   Introduction

Stiffened plates are commonly used in various engineering applications because they are able to resist buckling and provide additional stability and rigidity to the structure. Welded stiffened plates are an important component of many engineering structures, including shipbuilding, offshore platforms and civil

engineering, such as, bridges. An assessment of their free and forced responses is also generally very important for the safe and rational structural design of these members of structures. These plates are made of thin metal sheets that are reinforced by stiffeners, which are typically placed parallel to the plate's surface, and they are formed by welding stiffeners on bare plates. The stiffeners provide increased strength and stability, enabling the plate to better withstand loads such as bending, torsion, and buckling. The shape of plates can be square rectangular, circular, trapezoidal, etc. They can be stiffened in one or two directions with stiffeners of flat, L, box, trapezoidal or other shapes. The central deflection of simple supported stiffened plates subjected to transverse and axial load can be estimated, as well as the influence of parameters such as the number of longitudinal and transverse stiffeners and the ratio between their height and thickness. In recent years, there has been a growing interest in improving the design of stiffened plates to make them lighter, stronger and more cost-effective.

To this end, researchers have been exploring new materials, new fabrication techniques, and new design strategies, which remain a widely researched topic. Several researchers have studied the dynamic responses of rectangular plate systems having different sets of edge constraints and loading cases [1] [2]. The refined empirical formulation proposed to predict the ultimate strength performance or ultimate limit state of flat-bar type steel stiffened panels under longitudinal compression [3]. Stability issues have a significant impact on welded structures in terms of local, general and torsional buckling [4].

Nowadays, an important field of application of stiffened plates is ship architecture and offshore engineering, where they are basic structural members. Various loads on a ship's structure are complex phenomena that have been the subject of extensive research in the field of naval architecture. The design of a ship's hull, as well as its stability and strength, are greatly affected by wave loads, which arise from the interaction between the ship and the ocean waves. The intensity and frequency of wave loads depend on various factors such as the ship's speed, wave height, and frequency, as well as the ship's geometry, displacement, and type of loading. The understanding of wave loads is important for the design and safe operation of ships, as well as for the prediction of the response of ships to these loads, including structural deformation, slamming, and stress. The frequency response of plates with openings subjected to point excitation force and enforced acceleration at boundaries is analyzed by using developed in-house code for the mode superposition method [5]. Yang et. al. [6] dealt with the dynamic ultimate strength of ship bottom stiffened plates under uniaxial compression and lateral pressure. The dynamic ultimate strength of a tested specimen was calculated based on the nonlinear FEA.

The forced vibration analysis of optimized trapezoidal stiffened plates with simple supported conditions on the four edges of the base plate provides valuable insights into the transient dynamic behavior of the structure. Drawing the conclusion from finite element analysis, this circumstance greatly affects the result.

The optimization process used in this study ensures that the final design is both economically and structurally efficient, while the use of the Lanczos iteration method provides a reliable and efficient way to calculate the natural frequencies, mode shapes, and the modal superposition method is an effective technique for reducing the computation time when performing dynamic response analyses of linear structures like transient force vibration analyses [7]. Dynamic analysis of time response is widely used in various engineering problems to study the effect of vibrations on the members of structures [8] [9].

In the present study, the focus is on the forced vibration analysis of optimized trapezoidal stiffened plates with simple supported conditions on the four edges of the base plate. Forced vibration analysis is a critical aspect of structural engineering and is essential in ensuring the safety and reliability of structures subjected to dynamic loads. The aim of the finite element analysis is to investigate the transient forced vibrations of the stiffened structures subjected to uniaxial compression from sudden and rapidly applied pressure, over the base plates [10]. This study is essential in identifying potentially dangerous cases and eliminating the possibility of failure. The optimization process used in this study minimizes the cost function that contains material and fabrication costs for Gas Metal Arc Welding (GMAW) welding technology. The optimization was performed with the Excel Solver program to ensure that the final design is both economically and structurally efficient.

2 Optimum Design of Stiffened Plates

The structural optimization of different stiffened plates and shells has been worked out by Farkas and Jármai [11]. The optimum design of stiffened plates involves finding the optimal combination of plate and stiffener geometry, material properties, and loading conditions that meet the desired mechanical performance while minimizing weight.

The design of stiffened plates requires a detailed understanding of plate buckling, plate-stiffener interaction, and stress distribution. Plate buckling occurs when the plate experiences a compressive load that exceeds its critical buckling strength. The buckling behavior of a plate can be influenced by its geometry, boundary conditions, and material properties. Plate-stiffener interaction refers to the interaction between the plate and the stiffener, which can enhance the plate's resistance to buckling. The distribution of stress in a stiffened plate is influenced by the plate-stiffener interaction and the loading conditions.

The optimum design of stiffened plates can be performed using various numerical methods, such as finite element analysis (FEA), boundary element analysis (BEA), and multi-objective optimization algorithms. FEA and BEA allow for a

detailed analysis of the plate-stiffener interaction and the stress distribution in the plate, while multi-objective optimization algorithms allow for an efficient search of the design space to find the optimal solution.

In the optimum design of stiffened plates, various design objectives must be considered, such as minimizing weight, maximizing strength, reducing deflection, and minimizing stress concentration. These design objectives may conflict with each other, and the optimum design must find a trade-off that satisfies all objectives. The trade-off can be performed using multi-objective optimization algorithms, such as genetic algorithms, particle swarm optimization, and ant colony optimization.

The material properties of the plate and the stiffener also play an important role in the optimum design of stiffened plates. The material properties, such as yield strength, elastic modulus, and Poisson's ratio, can influence the plate's resistance to buckling and the distribution of stress in the plate. The use of advanced materials, such as composite materials, can significantly improve the mechanical performance of stiffened plates, but also increase their complexity and cost. The composite structures are also a way to reduce the mass of the structure [12].

The boundary conditions of the plate and the stiffener also play a crucial role in the optimum design of stiffened plates. The boundary conditions, such as fixed-end, simple supported, and clamped, can influence the plate's buckling behavior and the distribution of stress in the plate. The boundary conditions must be carefully selected to ensure that the plate's buckling behavior and stress distribution are consistent with the desired mechanical performance.

In conclusion, the optimum design of stiffened plates is a complex process that involves finding the optimal combination of plate and stiffener geometry, material properties, and loading conditions that meet the desired mechanical performance while minimizing weight. The optimum design requires a detailed understanding of plate buckling, plate-stiffener interaction, and stress distribution, as well as the use of numerical methods and multi-objective optimization algorithms. The design objectives, material properties, and boundary conditions must also be carefully considered to ensure that the optimum design satisfies the desired mechanical performance.

With a better understanding of the optimum design of stiffened plates, engineers can design structures that are lighter, stronger more cost-effective and contribute to the development of sustainable/efficient engineering solutions [13].

In the following calculation, the base plate has a width of $B = 4000$ mm and a length of $L = 6000$ mm. Young's modulus is $E = 2.1 \times 10^5$ MPa, material density is $\rho = 7.85 \times 10^{-9}$ t/mm3. The stiffeners are welded to the base plate with fillet welds to reinforce the plate. The design variables, the thicknesses of the base plate (t_F) and stiffener (t_S) and the number of ribs (φ-1). The numerical results for uniaxial compression and magnitude of lateral pressure are summarized in Tab. 1,

in which the columns contain the optimized main geometrical data. The geometric designs of the structures, based on Table 1, were used for the transient vibration analysis in this paper, in which the pressure is considered to be suddenly applied. The objective of the forced vibration analysis is to investigate whether the optimization objective functions are also satisfied under dynamic effects.

Table 1

Optimum dimensions for trapezoidal stiffener at three different lateral pressures (p) and constant uniaxial compression ($N = 1.974 \times 10^7$ N) in case of two yield stresses (f_Y)

No.	p [MPa]	f_Y [MPa]	t_F [mm]	t_S [mm]	$\varphi - 1$ [-]
1	0.02	235	23	9	3
2	0.01	235	23	8	3
3	0.005	235	22	8	3
4	0.02	355	17	10	4
5	0.01	355	18	8	5
6	0.005	355	15	8	5

The dimensions with numerical values in Figure 1 are fixed in the calculations, while the other dimensions of stiffeners can be derived from the optimized results of Table 1 based on [13].
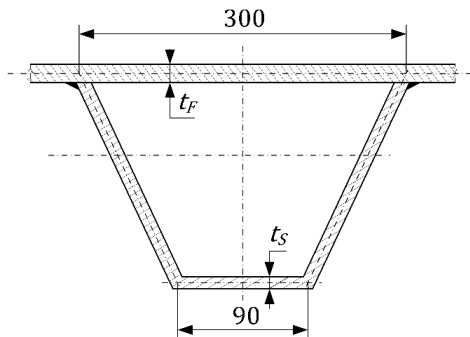

Figure 1

Geometrical designs of the trapezoidal stiffener profiles with the optimized thicknesses

3 Finite Element Analysis

The finite element analysis (FEA) is used to numerically solve differential equations arising in engineering and modelling problems such as vibration analysis problems. The main concept is that the geometry of structures subdivides into non-overlapping smaller parts, called finite elements, which are implemented

by the construction of a mesh. The conventional element types possess simply shaped geometry with well-defined stress displacement relationships. If applied loads or geometric nonlinearity were considered so that the best choice is the first-order elements. Thus, the sufficiently refined mesh needs to ensure that the results from simulations are adequate. Concerning shell structures such as our stiffened plate, the Reissner-Mindlin equations are used to model the bending of the plate so that thin and moderately thick plates can be modeled by structural optimization.

According to FE theory, the trapezoidal stiffened plates are meshed into finite elements with fine mesh resolutions, which are four-node reduced integration shell elements (S4R in Abaqus). The approximate global size is specified as 40 mm and yields enough accurate solutions.

3.1   Boundary Conditions

The material is assumed to be isotropic elastic. In our investigation, the stiffened plate is made of steel, provided that the steel grade is characterized by yield stress from Table 1, Young's modulus of $E = 2.1 \times 10^5$ MPa, Poisson's ratio of $v = 0.3$ and density of $\rho = 7.85 \times 10^{-9}$ t/mm^3.

The uniform thickness plate is stiffened by some trapezoidal-shaped stiffeners and simple support conditions are subjected on all the edges (SSSS) of the base plate. Figure 2 is depicted highlight, the side lengths of the quarter of the base plate parallel to the x-symmetry axis and y-symmetry axis are given by $L/2$ and $B/2$, respectively.
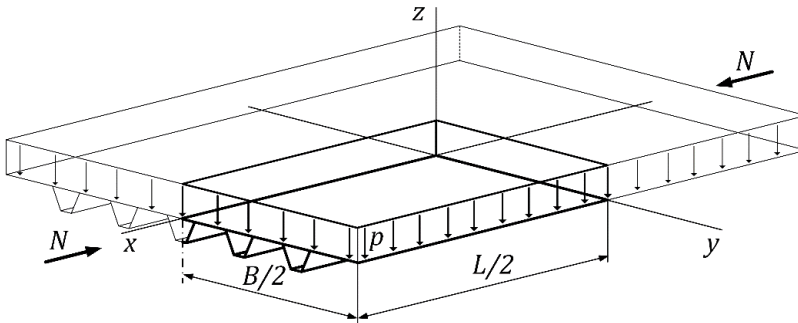

Figure 2
Design of trapezoidal stiffened plate

By exploiting the symmetries of the plate design and loadings, the displacement boundary conditions on the FE model are described on the highlighted quarter structure in Figure 2. The displacement boundary conditions for the points of one-quarter of the stiffened plate are $u_y = \phi_x = \phi_z = 0$ in the z-x plane and in the y-z plane $u_x = \phi_y = \phi_z = 0$ and simply prescribed supports are at the edge of $x = L/2$

according to $u_z = \phi_x = 0$ and at the edge of $y = B/2$ according to $u_z = \phi_y = 0$, where u_x, u_y, and u_z denote the displacements of a point in the mid-plane of the trapezoidal stiffened plate along the x, y, and z directions i.e. longitudinal, transverse and vertical directions, respectively. ϕ_x, ϕ_y, and ϕ_z are the rotations of the normal to the mid-plane at the same point of the structure.

3.2   Modal Analysis and Mode Superposition

To investigate transient vibration analysis for the stiffened plate with trapezoidal stiffeners is performed with these steps, using the commercial software Abaqus. The eigenvalue extraction to calculate the natural frequencies and mode shapes is based on the Lanczos iteration method described in [14], which is used to perform the frequency response analysis or to investigate the eigenvalues for buckling prediction and is applied to extract natural frequencies and modes. Two analysis steps are used for the mode shapes belonging to the trapezoidal stiffened plate subjected to uniaxial compression. The compression, exerted by the force N, is constant at each step. In the first step, the uniaxial compression and geometric nonlinearity are considered so that in the second step, the load stiffness is determined at the end of the first general analysis step and can be included in the eigenvalue extraction.

The rapidly applied pressure on the base plate also causes transient vibrations of the structure, which can be examined by the third step with mode superposition. The first twelve mode shapes in the mode superposition method by the third step are given by creating the second step with static loading.

3.3   Transient Vibration Analysis

Figures 3-5 show the transient responses of the stiffened plates at the center of the base plate, i.e., at the origin of the xyz coordinate system. The damping ratio is considered for the FE models of the welded stiffened plates. Note here that when damping is given as a fraction of critical damping associated with the first sixteen mode shapes, the values used are in the range of 1% to 10% of critical damping [14]. As expected, the peak dynamic deflection values are nearly twice the amount for the critical damping of 1%.

Peak dynamic deflection is a parameter to evaluate deformation upon a sudden applied pressure, and it is calculated as the distance between the front of the system before percussion and its maximum displacement after percussion, which are the absolute values that can be read as the first peak in Figures 3-5. The numerical results of the FE analysis for static and dynamic deflection are summarized in Table 2, which contains the stress values of the peak dynamic deflections at the center of the base plates. Therefore, optimization objective

functions [13], such as the central deflections below 1% of length *L,* are also satisfied under dynamic effects, due to sudden, applied pressure.
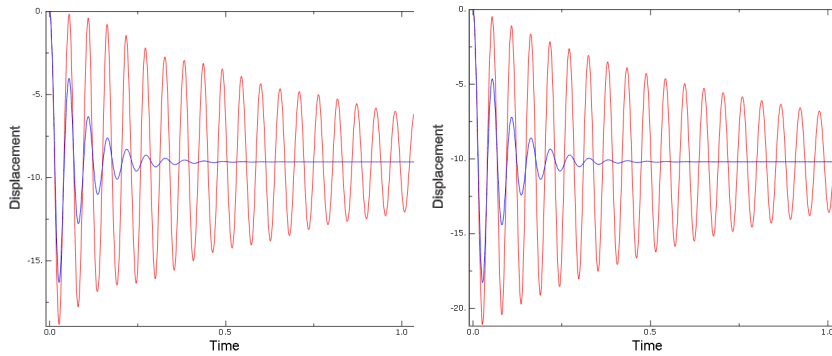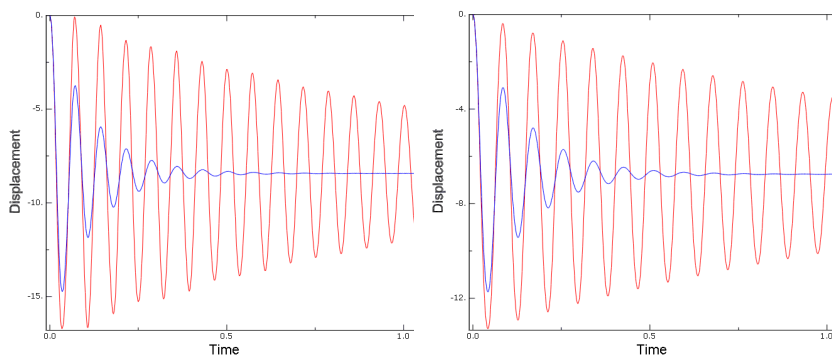

Figure 3

Displacement time-history curve for the critical damping fractions 0.01 (red solid line) and 0.1 (blue solid line) for the magnitude of p = 0.02 MPa and yield stresses f_Y = 235 MPa and f_Y = 355 MPa at the center of the base plate
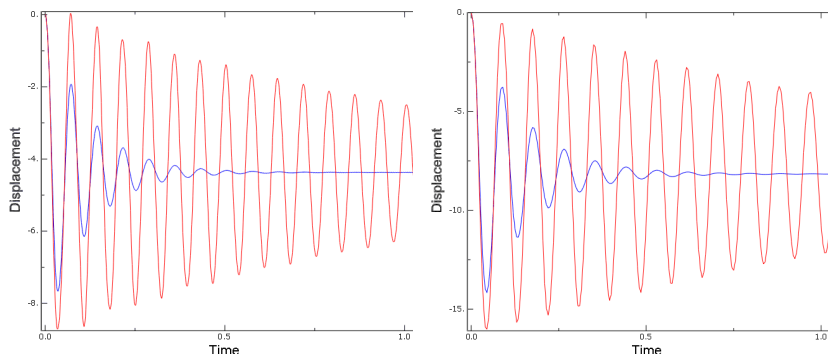

Figure 4

Displacement time-history curve for the critical damping fractions 0.01 (red solid line) and 0.1 (blue solid line) for the magnitude of p = 0.01 MPa and yield stresses f_Y = 235 MPa and f_Y = 355 MPa at the center of the base plate

Figure 5

Displacement time-history curve for the critical damping fractions 0.01 (red solid line) and 0.1 (blue solid line) for the magnitude of $p = 0.005$ MPa and yield stresses $f_Y = 235$ MPa and $f_Y = 355$ MPa at the center of the base plate

Table 2

Comparison of peak dynamic and static deflection as well as stress values for dynamic deflection according to the critical damping fraction in the midpoint of the base plate

No.	Static deflection [mm]	Peak dynamic deflection [mm]		stress at midpoint [MPa]	
		$\xi = 0.01$	$\xi = 0.1$	$\xi = 0.01$	$\xi = 0.1$
1	9.05	18.85	16.31	51.71	45.69
2	8.42	16.72	14.74	38.12	33.46
3	4.37	8.72	7.66	20.20	17.72
4	10.2	21.08	18.28	70.79	62.08
5	6.75	13.28	11.73	32.38	28.54
6	8.16	16.02	14.17	42.74	37.56

Due to the structural design, the stresses in Table 2 do not coincide with the maximum value of von Mises stress because the stress concentrations occur at the base of the ribs in the vicinity of the supports. The effect of the optimized ribs and plate thicknesses on the dynamic deflection values is complex, as shown in Table 2, so some finite element analyses are required to clarify the relationships.

Conclusions

The modal superposition method is used in this paper to calculate the transient response of plates accurately and efficiently by applying the shapes modes. The study concludes that the effect of the optimized ribs and plate thicknesses on the dynamic deflection values is complex, so some finite element analyses are required to clarify the relationships. The critical damping fraction is considered for the FE models of the welded stiffened plates the values used commonly used limits of the accepted range.

Other important circumstances are the choice of steel grade which greatly affects the results of dimensions of the optimized stiffened plates and the finite element analysis which predicts the behavior of a structure under a sudden and rapidly applied pressure. This finding highlights the importance of considering material properties when performing forced vibration analysis and underscores the need for careful selection of materials in engineering design. The results of the simulations show that peak dynamic deflections remain below the deflection condition specified in the optimization which is one percent of length L. In general, the plate is suitable for sudden pressure applications, as it has sufficient reserve capacity.

The study highlights the importance of considering material properties in the analysis of forced vibration and emphasizes the need for careful selection of materials in engineering design. From the numerical investigations, it is concluded that FEA can be used safely, to identify the dynamic characteristics of welded stiffened structures. In future work, we will compare the FEA with the experimental results, which can help validate the model results.

References

[1]   D. S. Cho, J.-H. Kim, T. M. Choi, B. H. Kim, N. Vladimir, "Free and forced vibration analysis of arbitrarily supported rectangular plate systems with attachments and openings", Eng. Struct., Vol. 171, pp. 1036-1046, 2018, https://doi.org/10.1016/j.engstruct.2017.12.032

[2]   Y. Mochida, S. Ilanko, "Transient vibration analysis of a completely free plate using modes obtained by Gorman's superposition method", J. Sound Vib., Vol. 329, Issue 10, pp. 1890-1900, https://doi.org/10.1016/j.jsv.2009.11.029

[3]   J. K. Paik, A. K. Thayamballi, B. J. Kim, "Large deflection orthotropic plate approach to develop ultimate strength formulations for stiffened panels under combined biaxial compression/tension and lateral pressure", Thin-Walled Struct., Vol. 39, No. 3, pp. 215-246, 2001, https://doi.org/10.1016/S0263-8231(00)00059-8

[4]   H. S. Kim, Y. M. Park, B. J. Kim, K. Kim, "Numerical investigation of buckling strength of longitudinally stiffened web of plate girders subjected to bending", Struct. Eng. Mech., Vol. 65, No. 2, pp. 141-154, 2018, DOI: https://doi.org/10.12989/sem.2018.65.2.141

[5]   D. S. Cho, B. H. Kim, J.-H. Kim, N. Vladimir, T. M. Choi, "Frequency response of rectangular plates with free-edge openings and carlings subjected to point excitation force and enforced displacement at boundaries", Int. J. Nav. Archit., Vol. 8, Issue 2, pp. 117-126, 2016, https://doi.org/10.1016/j.ijnaoe.2015.06.001

[6]   B. Yang, J.-M. Wu, C. G. Soares, D.-Y. Wang, "Dynamic ultimate strength of outer bottom stiffened plates under in-plane compression and lateral

pressure", Ocean Eng., Vol. 157, pp. 44-53, 2018, https://doi.org/10.1016/j.oceaneng.2018.03.051

[7]   K. J. Bathe, Finite Element Procedures, Englewood Cliffs, NJ, USA, Prentice-Hall Inc., 1996

[8]   F. D. Popescu, S. M. Radu, K. Kotwica, A. Andraș, I. Kertesz Brînaș, S. Dinescu, "Vibration analysis of a bucket wheel excavator boom using Rayleigh's damping model", New Trends Prod. Eng., Vol. 2, No. 1, pp. 233-241., 2019, https://doi.org/10.2478/ntpe-2019-0024

[9]   A. Andraș, S. M. Radu, I. Brînaș, F. D. Popescu, D. I. Budilică, E. B. Korozsi, "Prediction of Material Failure Time for a Bucket Wheel Excavator Boom Using Computer Simulation", Materials, Vol. 14, No. 24, 7897, 2021, https://doi.org/10.3390/ma14247897

[10]   J. Błachut, O. R. Jaiswal, "Instabilities in torispheres and toroids under suddenly applied external pressure", Int. J. Impact Eng., Vol. 22, pp. 511-530, 1999, https://doi.org/10.1016/S0734-743X(98)00067-0

[11]   J. Farkas, K. Jármai, "Economic Design of Metal Structures", Millpress, Rotterdam, 2003

[12]   Gy. Kovács, J. Farkas, "Minimum cost design of overhead crane beam with box section strengthened by CFRP laminates", Struct. Eng. Mech., Vol. 61, No. 4, pp. 475-481, 2017, https://doi.org/10.12989/SEM.2017.61.4.475

[13]   Z. Virág, K. Jármai, "Optimum design of stiffened plates for static or dynamic loadings using different ribs", Struct. Eng. Mech, Vol. 74, No. 2, pp. 255-266, 2020, https://doi.org/10.12989/sem.2020.74.2.255

[14]   Abaqus 6.13 Online Documentation; Dassault Systems, 2015. Available online: http://130.149.89.49:2080/v6.13/index.html

A Proposal of a Heat Input Model, for Heating Correction, on Welded Steel Structural Members

Guan Xiaoyu, Tokumaru Yujiro, Hirohata Mikihito[*]

Graduate School of Engineering, Osaka University
2-1, Yamada-oka, 5650871, Suita, Osaka, Japan;
x-guan@civil.eng.osaka-u.ac.jp; y-tokumaru@civil.eng.osaka-u.ac.jp;
hirohata@civil.eng.osaka-u.ac.jp (corresponding author)

Mukawa Satoshi, Okada Seiji

IHI Infrastructure Systems, 3-17-12, Shibaura, Minato-ku, 1080023, Tokyo,
Japan; mukawa7877@ihi-g.com; okada0269@ihi-g.com

Abstract: A series of experiments and analyses were conducted for evaluating a simple heat input model, for heating correction on welded steel structural members. The heating experiment on steel plates, with different thicknesses, was simulated using thermal elastic–plastic analysis. The temperature histories, deformations and residual stresses of plates could be simulated by the simplified heat source model, proposed in this study. The applicability of the heat source model was verified, by simulating the heating correction for T-shaped fillet welded joints.

Keywords: Welding; Steel structures; Deformation; Heating correction; Finite element analysis

1   Introduction

Welding is widely used to manufacture factory and on-site joints as a joining method for the fabrication of steel structural members. Compared with other joining methods, such as high-strength bolting, welding has the advantages of greater design freedom, higher workability in narrow spaces, and the ability to reduce the weight of structures. However, there are drawbacks, such as deformation due to heat input from the weld, generation of residual stress, and the risk of defects and cracks in the weld. Welding deformation adversely affects assembly accuracy and strength; therefore, if the deformation exceeds the allowable value, it must be corrected.

There are several correction methods, such as fixing the shrunken part using a hammer, heating the stretched part with gas burners, and correcting the deformation using the temperature difference between the front and back surfaces of the member (heating correction), etc. Among these methods, heating correction is generally used owing to its high workability. The heating position and time depend on the experience of the skilled technicians. With the reduction in the number and aging of technicians, the difficulty of transferring technical expertise to the next generation of technicians has become an important issue.

Many studies have been conducted on the relationship between heat input conditions and deformation, when steel structural members are heated with gas burners [1] [2]. The heating correction of welded assembly parts is similar to that of the bend processing technology [3]. However, the size and curvature of the deformation for the heating correction of welded members differ from those of the bending operation of hull structures. The estimation of the relationship between the heat input condition and correction effects using a numerical simulation based on the finite element method can contribute to the efficiency and automation of heating correction work. A method for precisely modeling the heat input owing to a gas flame, which simulates the heat input for plate bending using the finite element method, has been proposed [4-5].

However, for the heating correction simulation of large, welded assembly parts, a simpler and more versatile heat input model is necessary.

In this study, heating experiments and simulations were performed to develop a simple heat input model based on a previous study [6]. Heating-correction experiments and simulations of T-joint members were conducted to validate the proposed model. This study contributes to the establishment of an effective simulation method for reproducing the heating-correction process. The heat input model introduced in this study is a simple and versatile model that can be used for the heating correction simulation of welded assembly parts, thus being potentially useful in various engineering areas.

2 Experiment

2.1 Specimen

To simulate the heating correction process in this study, a thermal elastic–plastic analysis was performed using the finite element method. Moreover, to propose a simple heat input model of a gas flame for heating correction, basic gas-flame heating experiments and simulations were conducted.

The steel plates used for the experiment were square, 200mm on each side. The plate thicknesses were 9, 12, and 25 mm, respectively. Figure 1 shows the shapes and dimensions of the specimens. Six specimens were used. Two specimens of different thicknesses were prepared. The plate was made of general structural steel SM400A, as specified by JIS G3106. Table 1 lists the mechanical properties of the materials, including their yield strength, tensile strength, and elongation, as illustrated in the mill test reports. The specimens were annealed before heating to remove the initial residual stress caused by rolling.
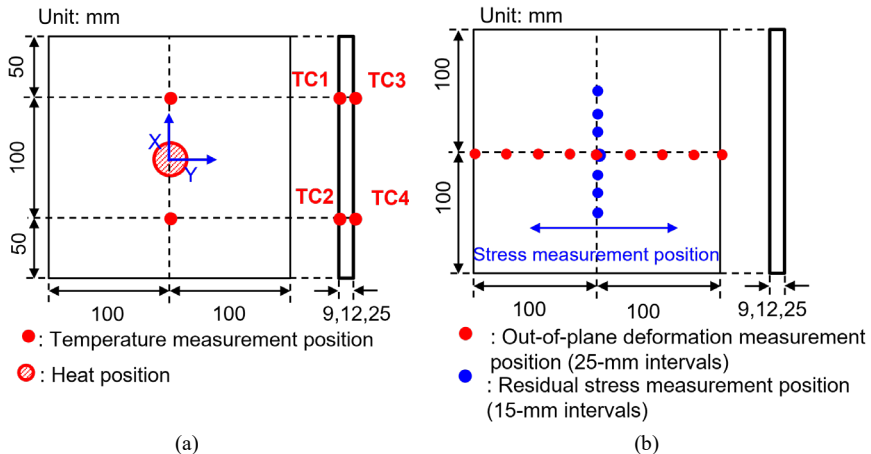
Figure 1

Shapes and dimensions of steel plate specimens and measurement positions of (a) temperature and (b) out-of-plane deformation and residual stress on the steel plate specimens

Table 1

Mechanical properties of materials for steel plate specimens

Thickness (mm)	Yield strength (N/mm²)	Tensile strength (N/mm²)	Elongation (%)
9	333	442	30
12	294	422	34
25	301	442	33

2.2   Experimental Procedure

According to the Specifications for Highway Bridges (II Steel Bridges/Steel Members Edition) [7], the surface temperature of steel materials in heating correction should be below 750 °C for tempered steel to suppress changes in the metal structure of steel materials. In this experiment, the target temperature of the heated surface of the steel plate by the gas burner was set at 500–600 °C. The burner used propane as the fuel and oxygen as the oxidizer; the flame length was 70 mm,

and the gas flame temperature was 1,500–1,800 °C. The heat input to the specimen was located at the center of one of its sides, and heating was performed for 20 s. The gas flow velocity was adjusted appropriately while the flame conditions were checked. After heating, the specimens were allowed to cool naturally.

To measure the temperature history of the specimens, thermocouples were attached at two locations on the front and back surfaces (front surface: TC1 and TC2; back surface: TC3 and TC4). Figure 1 (a) shows the positions of the thermocouples. The thermocouples were of K-type used for relatively high-temperature ranges. In addition, the central temperatures of the front and back surfaces of the specimens were measured using the InfRec R450Pro infrared camera. The temperature history during the heating process was measured using thermocouples and an infrared camera, whereas that during the cooling process was measured only using thermocouples.

Figure 2 shows the installation and heating conditions of the specimens. The specimens were fixed using a magnet during heating. After heating, the specimens were removed from the burner installation table and left unrestrained during cooling. As the specimen and thermocouples were covered by a gas flame jet on the surface during heating, the temperature of the specimen could not be measured accurately using an infrared camera and thermocouples at the front surface. Therefore, in this experiment, the temperature history of the back surface of the specimen was used as the simulation target, as described later.
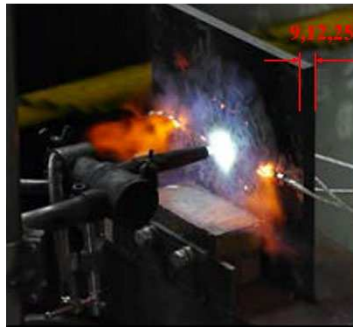
Unit: mm

Figure 2
An image of heating experiment on steel plate specimen

After heating and cooling, the out-of-plane deformation was measured using a dial gauge at nine points (25-mm intervals) on the centerline in the horizontal direction of the specimen. The out-of-plane deformation was also measured before heating, and the out-of-plane deformation due to heating was obtained as the difference in deformation before and after heating (Figure 1 (b)). The residual stress was measured via X-ray diffraction (μ-X360s, Pulstec Industrial Co., Ltd.) at seven points (15-mm intervals) on the centerline in the vertical direction of the steel plate (Figure 1 (b)). The radiation source for the X-ray diffraction method was chromium.

The collimator diameter was 1.0 mm. The voltage and current of the X-ray tube were 30 kV and 0.5 mA, respectively.

3   Flame Simulation by Thermal Fluid Analysis

3.1   Analysis Method

To construct a heat input model for thermal elastic–plastic analysis (described later), thermal fluid analysis was performed to examine the heat flow velocity distribution affecting the range of heat input to the steel plate owing to the gas flame.

Previous studies have shown that the shape of the heat flux distribution can be classified according to the ratio of the burner diameter B (mm) to the distance H (mm) from the heated steel material [8]. In this study, the diameter was 14mm, and the distance between the specimen and gas burner was 20mm. A feature of the heat flux distribution when $0.5 < H / B < 7$ is that the maximum temperature appears outside the heating center. In addition, the flame temperature directly above the steel plate significantly affects the determination of the heat input to the steel plate. The temperature directly above the steel plate is proportional to the heat input [9]. In this study, to determine the maximum point of the heat flux distribution, the temperature distribution directly above the steel plate was calculated using thermal fluid analysis [10] [11] based on the approximate solution method, as shown below.

The basic equations for a turbulent combustion field in an axisymmetric two-dimensional plane are the continuity equation, two-way Navier–Stokes equation, and conservative scalar equation shown in Equations (1), (2) and (3), respectively. To introduce a conserved scalar quantity, the ratio of the Lewis number (temperature diffusion coefficient and concentration diffusion coefficient) was set to 1, and the fluid was assumed to be incompressible by the low Mach approximation.

$$\frac{\partial u}{\partial x} + \frac{\partial v}{\partial y} = 0 \tag{1}$$

$$\frac{\partial V}{\partial t} + u\frac{\partial V}{\partial x} + v\frac{\partial V}{\partial y} = \frac{\partial p}{\partial x} + \frac{1}{Re}\left(\frac{\partial^2 u}{\partial x^2} + \frac{\partial^2 v}{\partial y^2}\right) \tag{2}$$

$$\frac{\partial T}{\partial x} + \frac{\partial}{\partial x}(VT) = a\frac{\partial T}{\partial x \partial y} \tag{3}$$

where V is the velocity (m/s), u and v are the velocity components in the x and y directions (m/s), respectively, t is time (s), p is pressure (Pa), Re is the Reynolds number, T is temperature (degrees), and a is the thermal diffusion coefficient (m^2/s).

Assuming that u, v, and p at an arbitrary time t are known, calculating v, u, and p after an infinitesimal time of Δt s using the fractional step method solves Equation (1) and Equation (2) step-by-step. Subsequently, the obtained velocity was substituted into Equation (3) to calculate the temperature. The fractional step method was used for correction by adding the pressure term after calculating the provisional velocity and excluding the pressure term. Eliminating the pressure term from the Navier–Stokes equation yields Equation (4) (two-dimensional Burger's equation).

$$\frac{\partial V}{\partial t} + u\frac{\partial V}{\partial x} + v\frac{\partial V}{\partial y} = \frac{1}{Re}\left(\frac{\partial^2 u}{\partial x^2} + \frac{\partial^2 v}{\partial y^2}\right) \tag{4}$$

These equations can be decomposed into advection and diffusion equations, and the velocities can be easily calculated using the finite-difference method. Using the obtained velocity as the provisional velocity, Equations (5) and (6) are obtained from the difference between the Navier–Stokes equations with and without the pressure term, as follows:

$$u' = u^* - \frac{\partial p}{\partial x}\Delta t \tag{5}$$

$$v' = v^* - \frac{\partial p}{\partial y}\Delta t \tag{6}$$

where u^* and v^* are tentative velocities, u' and v' are true velocities corrected by pressure after Δt s.

The true velocities were corrected by pressure in Equations (5) and (6). Equation (7) (Poisson's equation) was obtained by substituting these equations into the continuity equation. In addition, pressure p' after Δt s was obtained by solving this equation using an iterative method (SOR method) until the discrepancy falls within an acceptable error range.

$$\frac{\partial^2 p'}{\partial x^2} + \frac{\partial^2 p'}{\partial y^2} = \frac{1}{\Delta t}\left(\frac{\partial u^*}{\partial x} + \frac{\partial v^*}{\partial y}\right) \tag{7}$$

By substituting the obtained pressure and calculating the Navier–Stokes equation, the velocities u and v after Δt s can be obtained.

The temperature distribution was calculated by substituting the velocity obtained from the above calculations into the conservative scalar equation. Considering the symmetry of the steel plate, the analysis range was 20–100 mm, which was the heating distance in the horizontal direction. The mesh size was 0.1 mm^2, Δt was 0.02 s, u, v, and p, at time 0 s was set as 0, and the burner flow velocity was provided only to the part adjacent to the port.

3.2   Analysis Result

The position at which the temperature was at its maximum and the distribution tendency of the temperature were calculated. Under this analysis condition, the

maximum temperature was observed at approximately 22 mm from the center of the steel plate. Figure 3 shows the temperature distributions obtained from the experiment at 1 and 6s from the start of heating. Thermal fluid analysis showed the temperature distribution directly above the steel plate (front surface) exposed to the gas flame. The maximum temperature could not be compared because the temperature on the back side of the steel plate was measured in the experiment. The distance was approximately 22 mm from the center of the steel plate, which agrees with the thermal fluid analysis results. This position corresponds to the maximum point of the aforementioned heat-flux distribution.
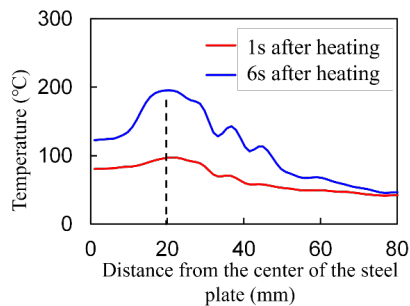
Figure 3
Temperature distributions obtained by the experiment from a 9-mm-thick specimen

4 Thermal Elastic–Plastic Analysis

4.1 Analysis Model

The heating experiment was simulated using thermal elastic–plastic analysis based on the finite element method. Temperature–displacement coupled analysis was performed using the commercial software ABAQUS. The entire specimen was modeled using 4-node shell elements. The temperature dependence of the mechanical properties and physical constants of the materials (Figure 4) was determined by referring to previous literature [12] [13]. The heat transfer from the model surfaces into the air was considered as the thermal boundary condition. Fixing the rigid-body displacement was considered as the mechanical boundary condition.
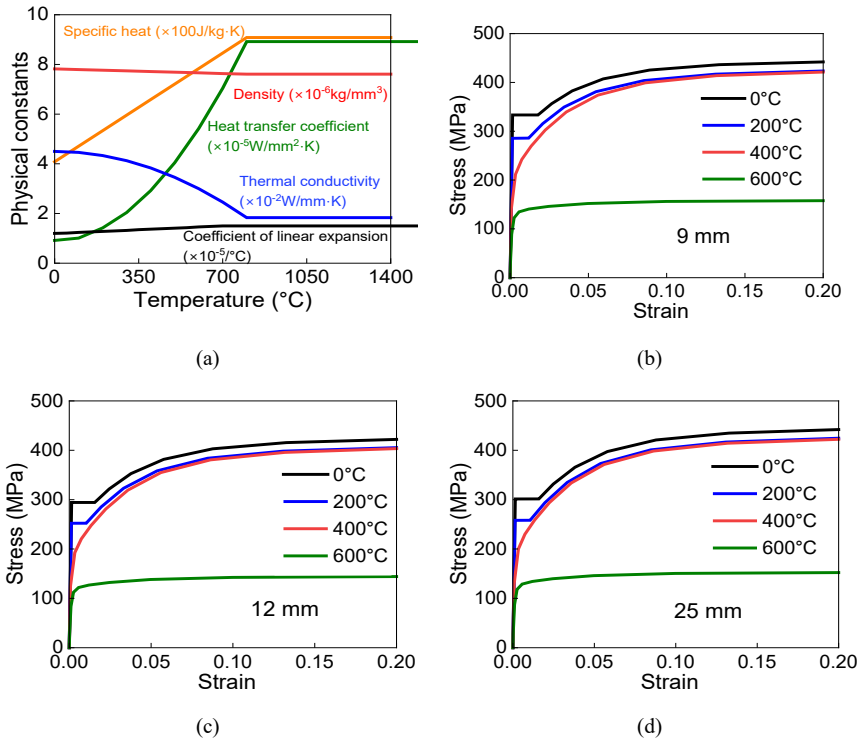
Figure 4

(a) Temperature-dependent physical constants and stress–strain relationships for (b) 9-mm-thick specimens, (c) 12-mm-thick specimens, (d) 25-mm-thick specimens

To construct a simple heat input model, the area affected by the heat input of the gas flame was examined based on the state of the jet flow during heating (Figure 2) and the specimen surface after heating (Figure 5).

Figure 6 shows the analysis model and heat input regions. The heat flux from the gas flame to the steel plate had a maximum value of 22 mm from the center of the steel plate. The heat flux then tended to decrease in proportion to distance. Based on this tendency, the area affected by the heat input was divided into two parts: the region directly affected by the jet, and the region affected by the jet that collided with the steel plate and diffused (diffusion region).

Furthermore, because the structure of a gas flame consists of inner and outer flames that generate a circulating airflow, the part that directly receives the jet was divided into inner and outer flames. The size of each part (the radius of the circle) was determined by referring to the surface of the steel plate after heating (Figure 5). The heat input (surface heat flux) was normally distributed in each part. However, in this analysis, for simplicity, the magnitude of the surface heat flux given to each

part (central inner flame area, q_1; maximum inner flame region, q_2, outer flame region, q_3; and diffusion region, q_4) were set as constants. The surface heat flux values were adjusted such that the temperature history obtained from the experiment could be reproduced. The diffusion radius r_4 of the heat-input-affected region was determined as 74 mm according to the experimental conditions. Radius r_3 was an intermediate value between r_4 and r_2.

Thickness: 9 mm

Figure 5
The surface of the steel plate after heating

(a)

(b)
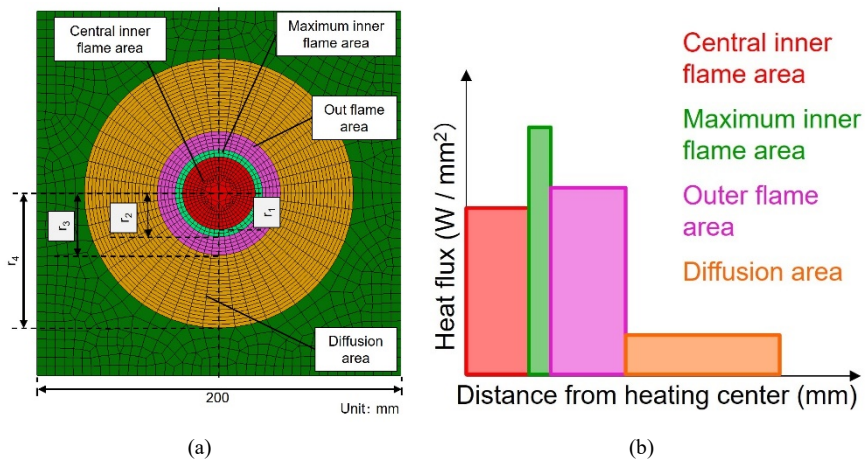
Figure 6
(a) Analysis model with heated regions and (b) heat flux distribution

4.2   Experimental and Analytical Results

4.2.1   Temperature History

Figure 7 plots the temperature histories at the center of the back surfaces of the specimens during heating measured by the infrared camera ($x = 10, 24, 35$ (mm)) and the temperature history at a position 50 mm away from the center ($x = 50$ (mm)) of the back surface of the specimen during heating and cooling measured by the thermocouple. As two specimens were used for each thickness, the average value and range were obtained and are shown in the figure. The solid line in Figure 7 shows the analysis results using the proposed heat input model. By applying the heat input of 0.7 W/mm^2 to the central inner flame region, 1.5 W/mm^2 to the maximum inner flame region, 0.6 W/mm^2 to the outer flame region, and 0.15 W/mm^2 to the diffusion region, the experimental results could be reproduced for each plate thickness. The surface temperature at the heat input position in the analysis was 574.4 °C, which was confirmed within the target temperature range (500–600 °C) in the experiment.
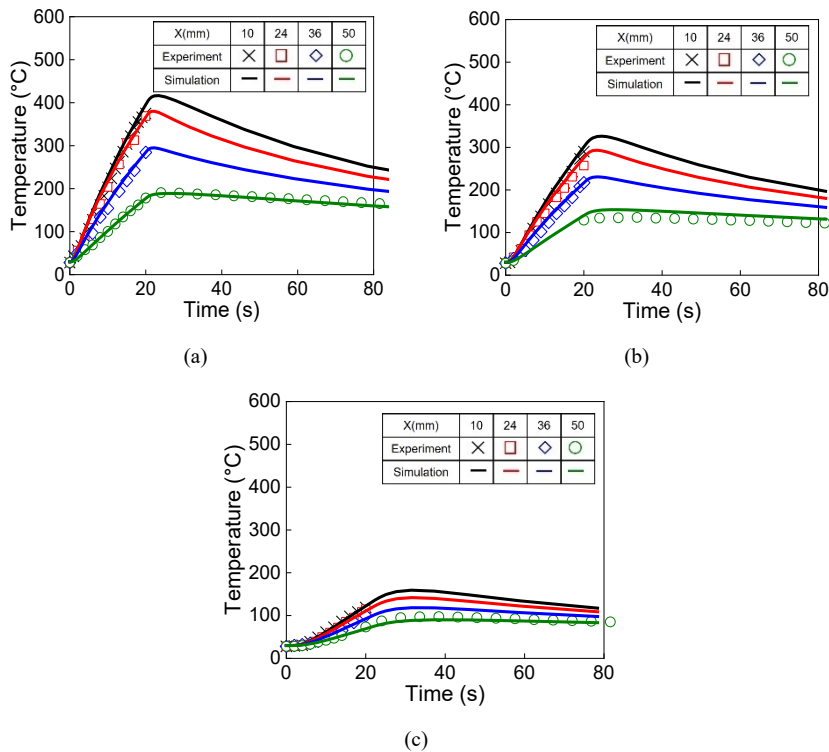

(a)

(b)

(c)

Figure 7
Temperature histories of (a) 9-mm thick, (b) 12-mm thick, and (c) 25-mm thick steel plates

4.2.2   Out-of-Plane Deformation

Figure 8 shows the measured results of the out-of-plane deformation and the simulated results of the analysis. For each specimen thickness, the averages of the measurements of the two specimens were used as the experimental results. The tendency of out-of-plane deformation obtained from the experiment for each plate thickness was reproduced by the analysis. The out-of-plane deformation increased with a thinner plate, and all the specimens tended to be convex on the front surface side, heated directly by the gas flame. During the heating process, the temperature of the front surface was higher than that of the back surface, resulting in a greater thermal expansion. During the cooling process, the temperature difference between the front and back surfaces, i.e., the difference in shrinkage between the front and back surfaces, decreased. It was presumed that the thermal expansion on the front surface during heating became dominant, and the front surface deformed into a convex shape.
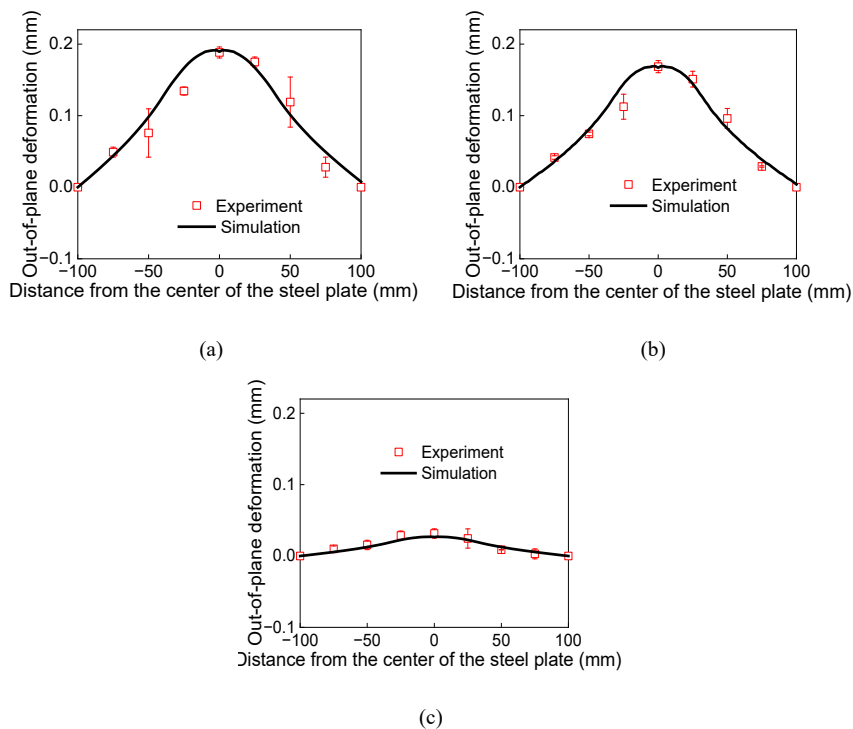

(a)

(b)

(c)

Figure 8

Out-of-plane deformations of (a) 9-mm thick, (b) 12-mm thick, and (c) 25-mm thick steel plates

4.2.3   Residual Stress

Figure 9 shows the measurement results of the residual stress and the results of reproduction by the analysis. The residual stress on the nonheated (back) surface was measured through X-ray diffraction because the metal structure at the directly heated surface affected the measurement accuracy. The average values of the residual stress of the two specimens for each thickness were measured using the experimental results shown in Figure 9. The tendency of the residual stress obtained experimentally for each plate thickness was reproduced by the analysis. The residual stress decreased with increasing plate thickness because the temperature at the back surface decreased with increasing plate thickness.
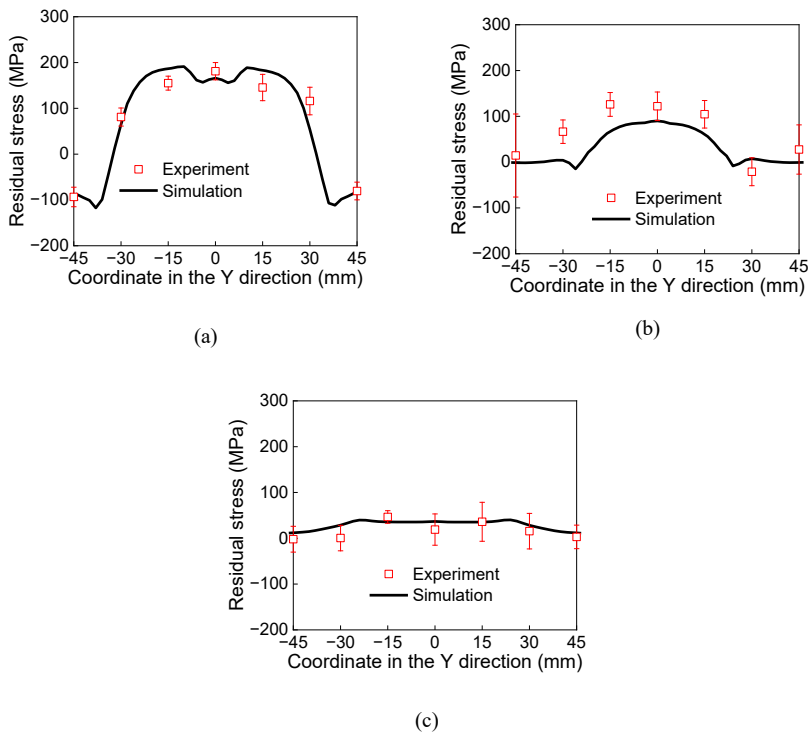

(a)

(b)

(c)

Figure 9

Residual stresses of (a) 9-mm thick, (b) 12-mm thick, and (c) 25-mm thick steel plates

5   Case Study

5.1   Specimen and Experimental Procedure

To investigate the applicability of the proposed heat input model, a heating correction experiment and simulation were performed on a T-shaped welded joint specimen as a case study. A T-shaped joint was fabricated using gas metal arc welding. Figure 10 shows the shapes and dimensions of the specimens. The base plate was square, with the side measuring 250 mm. A rib plate of height 80mm was welded to the midspan of the base plate. The thicknesses of the plates were 9 and 12 mm. The material used for the rib plate was SM400A with different thicknesses. Table 2, lists the mechanical properties of the materials, including yield stress, tensile strength, and elongation, as illustrated in the mill test reports. The out-of-plane welding deformation, was measured at the midspan of the specimen crossing the weld line.
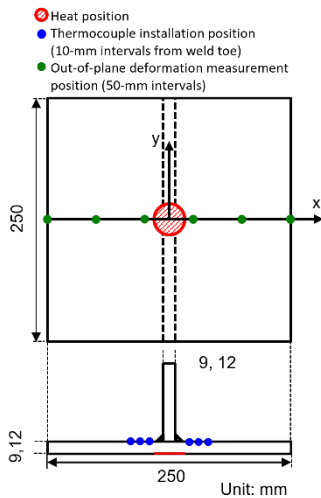

Figure 10

Shape and dimension of T-joint fillet-welded specimens

Figure 11

Image of the heating experiment on the T-joint specimen

Table 2

Mechanical properties of materials for the T-joint fillet-welded specimens

Thickness (mm)	Yield strength (N/mm^2)	Tensile strength (N/mm^2)	Elongation (%)
9	355	463	30
12	353	471	28

The heating experiment was conducted with the target temperature of the heated surface of the base plate ranging from 500 to 600 °C, wherein the rib plate was not welded. Propane and oxygen were used as the gases to heat the specimens. The distance between the specimen and the burner port was 30 mm, the flame length was 60 mm, and the gas flame temperature was 1,500 to 1,800 °C. The distance between the steel plate and the burner port was 20 mm, and heating was performed for 7–8 s. After heating, natural cooling was performed.

Thermocouples were installed on both sides of the weld toe to measure the temperature history of the specimens (Figure 10). There was a 10-mm spacing between every pair of thermocouples. The thermocouple closest to the weld toe was located 10 mm from the weld toe. Figure 11 shows the installation and experimental conditions of the specimens. Out-of-plane deformation was measured before and after heating along the centerline, as shown in Figure 10.

5.2   Numerical Simulation Procedure

The heating correction experiment of the T-joint specimen was simulated via thermal elastic–plastic analysis using the proposed heat input method. The basic analysis conditions were identical to those used for the steel plates. Figure 12 shows the analysis model with 4-node shell elements. Based on the experimental results, the welding out-of-plane deformation was considered as the initial deformation of the model.

The heating region was divided into four regions based on the proposed heat input model. The radius of each region was determined (r_1, r_2, r_3, r_4 = 12, 16, 42, and 74 mm) as per the thermal fluid analysis with heating conditions (heating distance of 30 mm and flame length of 60 mm). The magnitude of the heat flux in each region was examined to reproduce the experimentally-obtained temperature histories.
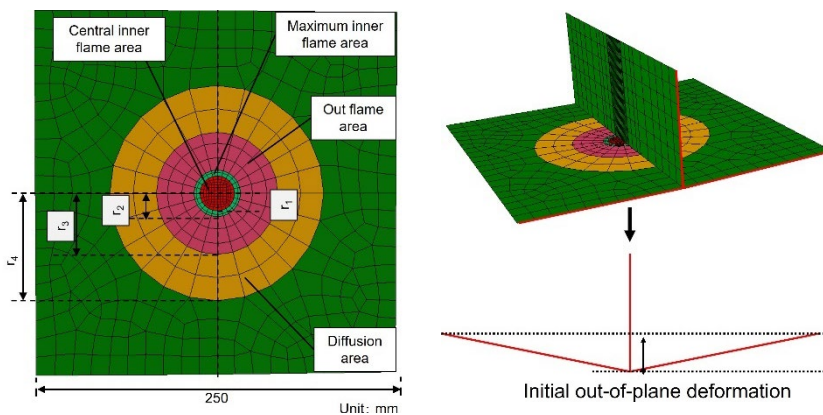

Figure 12
Analysis model for the T-joint specimen

5.3   Results and Discussion

Figure 13 shows the temperature histories obtained from the experiments and analysis. As the measurement results for each thickness of the two specimens showed little variation, only one of the data points for each is shown. This analysis was repeated to reproduce the experimental results by varying the heat flux magnitude. Finally, the experimental temperature history was reproduced using the magnitude of the heat flux as q_1: q_2: q_3: q_4 = 1.8:2.2:1.5:0.7 (W/mm^2). Figure 14, shows the out-of-plane deformations obtained from the experiments and analyses. The correction effect of the out-of-plane deformation in the experiment was reproduced in the analysis. Thus, the heat input model proposed in this study is applicable even to T-shaped welded joints.

It was natural that the smaller the plate thickness of the base plate, the greater the change in corrected out-of-plane deformations when the applied heat input was uniform. The magnitude of the corrected out-of-plane deformation for the 9 mm-thick T-joint specimen was larger than that for the 12 mm-thick T-joint specimen in the experiment. However, this tendency was not observed in the simulation results. The simulation result of the amount of out-of-plane deformation for the 9 mm-thick T-joint model was a little greater than that for the 12 mm-thick T-joint model. The reason might be that the T-joint model was built without initial residual stress. The initial residual stress will affect the results of the amount of out-of-plane deformation. In the future, the model with initial residual stress will be built for further verification.
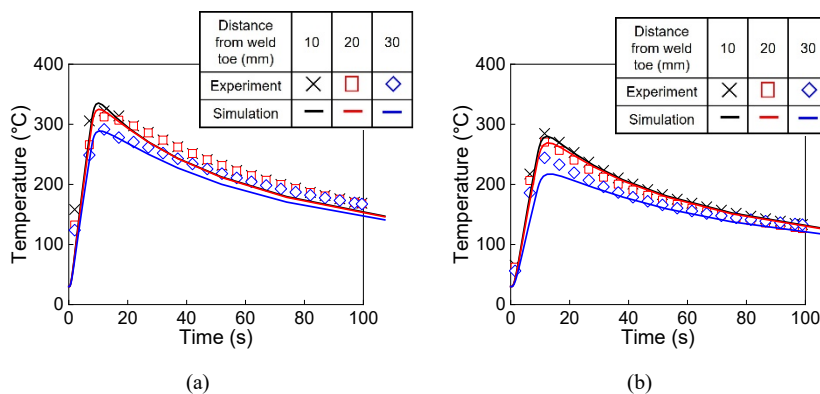

Figure 13

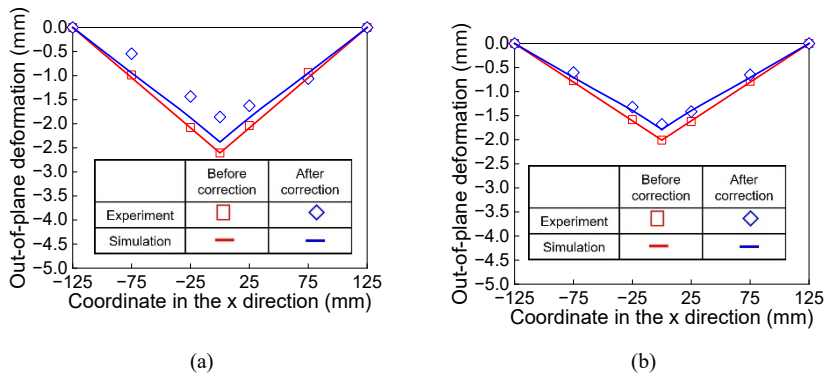Temperature histories for T-joint specimen of (a) 9 mm thickness and (b) 12 mm thickness

(a)   (b)

Figure 14

Out-of-plane deformations for the (a) 9-mm thick and (b) 12-mm thick T-joint specimens

Conclusions

In this study, a series of experiments and numerical simulations were performed to propose a simple heat input model for the heating correction of the welding deformation of steel plate members, by Finite Element Analysis (FEM). The main findings of this study are as follows:

(1) The characteristics of the heat input distribution of a gas flame were investigated through a heating experiment on steel plate specimens and thermal fluid analysis. Based on these, a heat input model was developed that provided different surface heat fluxes by dividing the heat input region into four types: inner flame region, maximum region, outer flame region, and diffusion region.

(2) To confirm the validity of the heat input model, a heating experiment was simulated using a thermal elastic–plastic analysis. The temperature history, out-of-plane deformation, and residual stress in the experiment were measured by applying heat to three different thicknesses with the target temperature of the heating surface ranging from 500 to 600 °C. The experimental results could be reproduced through analysis using the proposed heat input model.

(3) To examine the applicability of the proposed heat input model, experiments were conducted on fillet-welded T-section specimens. The temperature history owing to the heating correction and correction effect of the welding deformation could be reproduced by the analysis.

In this study, a thermal fluid analysis was performed, according to the heating conditions and a method was presented to determine the heat input distribution shape. However, because the magnitude of the heat flux for the heat input

distribution shape was determined based on the experimental results, its validity is limited and its generality has not been fully discussed.

For the actual application of this model, it is necessary to conduct a parametric study has to be conducted under various heat input conditions. Future work, to verify the general applicability of the heating correction model, experiments and analyses using larger specimens, with welding deformation, will be conducted.

Acknowledgment

References

[1]   Seong W J, Na S J: Systematization of heat straightening process of stiffened plate by surface flattening. Journal of Materials Processing Technology, 2022, 299: 117333

[2]   Gyura L, Gáspár M, Balogh A: The effect of flame straightening on the microstructure and mechanical properties of different strength steels. Welding in the World, 2021, 65(3): 543-560

[3]   Seong W J, Jeon Y C, Na S J: Ship-hull plate forming of saddle shape by geometrical approach. Journal of Materials Processing Technology, 2013, 213(11): 1885-1893

[4]   Shin J G, Woo J H: Analysis of heat transfer between the gas torch and the plate for the application of line heating. J. Manuf. Sci. Eng., 2003, 125(4): 794-800

[5]   Ferreño D, Carral J P, Calderón R L, et al.: Development and experimental validation of a simplified Finite Element methodology to simulate the response of steel beams subjected to flame straightening. Construction and Building Materials, 2017, 137: 535-547

[6]   Tokumaru Y, Hirohata M, Mukawa S, et al.: A proposal of simulation method for heating correction of welded members. Proceedings of Constructional Steel. 2020, 28, 731-738 (in Japanese)

[7]   Japan Road Association: Specifications for Highway Bridges (II) Steel Members Edition. 2017 (in Japanese)

[8]   Kumada M, Nakatogawa T, Hirata K: Heat and mass transfer by Impinging Jet. Journal of Japan Society of Mechanical Engineers.1973, 76, 822-830 (in Japanese)

[9]   Okano S, Tsuji H, Mochizuki M: Temperature distribution effect on relation between welding heat input and angular distortion. Science and Technology of Welding and Joining, 2017, 22(1): 59-65

[10] Tomita Y, Hashimoto K, Osawa N, et al.: Study on approximate analysis of convective heat transfer during line-heating process. Journal of the Society of Naval Architects of Japan. 1998, 184, 465-472 (in Japanese)

[11] Cotta R M, Lisboa K M, Curi M F, et al.: A review of hybrid integral transform solutions in fluid flow problems with heat or mass transfer and under Navier–Stokes equations formulation. Numerical Heat Transfer, Part B: Fundamentals, 2019, 76(2): 60-87

[12] Kim Y, Lee J, Inose K: The high accurate prediction of welding distortion generated by fillet welding. Quarterly journal of the Japan welding society. 2005, 23(3), 431-435 (in Japanese)

[13] Nakagawa H, Suzuki H: Ultimate temperatures of steel beams subjected to fire. Steel construction engineering. 1999, 6(22), 57-65 (in Japanese)

Full-scale Fatigue and Burst Tests on Notched Pipeline Girth Welds, under Complex Loading Conditions

János Lukács[*], Ahmad Yasser Dakhel

Institute of Materials Science and Technology, Faculty of Mechanical Engineering and Informatics, University of Miskolc
H-3515 Miskolc-Egyetemváros, Hungary
janos.lukacs@uni-miskolc.hu, metyaser@uni-miskolc.hu
* Corresponding author

Abstract: Hydrocarbon transporting pipelines contain a large number of girth welds, which are made under field conditions. The construction and the long-term operation often result in additional stresses to the internal pressure in these girth welds. The experience of the damage that has occurred and the requirement for safe operation necessitate full-scale tests to model and analyze these effects. The article presents a test system developed to investigate full-scale pipeline sections subjected to cyclic internal pressure and static external bending. The results obtained from tests of girth welds, with artificial circumferential and axial notches, are described herein. The results are used to draw conclusions on the load bearing capacity and integrity of the girth welds.

Keywords: transporting pipeline; full-scale test; complex loading; cyclic pressure; static bending; safety factor

1 Introduction

Hydrocarbon transport pipelines have a strategic importance within a country, but also between countries and nowadays even between larger geographical entities. The failures of these pipelines, for whatever reason, usually causes longer or shorter disruptions to the energy balance of a geographical unit. The direct consequence of this is that different levels of laws and standards of varying scope apply to all stages of the life-cycle of the pipelines [1-5].

Transporting pipelines are typically made up of 12-18 m long pipe strands and are joined by welding, in case of both seamless and longitudinally welded. A pipeline several hundred kilometers long will therefore have thousands of such girth welds, typically made by welding on site. The logical consequence of this is that different

standards apply to the welding tasks and the assessment of the completed circumferential welds, too [6] [7].

A statistical-like study [8] summarizes the reportable incidents of a 6.5-year research process. Figure 1 shows the cause distribution of all incidents (621 items), of not weld defects (571 items) and of weld defects (50 items). Because we do not have reason to assume that welds have a more favorable position from the point of view of corrosion and external force than the other pipeline parts, it can be stated that welds are the more damageable parts. However, the construction defects and material discontinuities occur in a much higher ratio in welds than in the other parts of the pipelines.
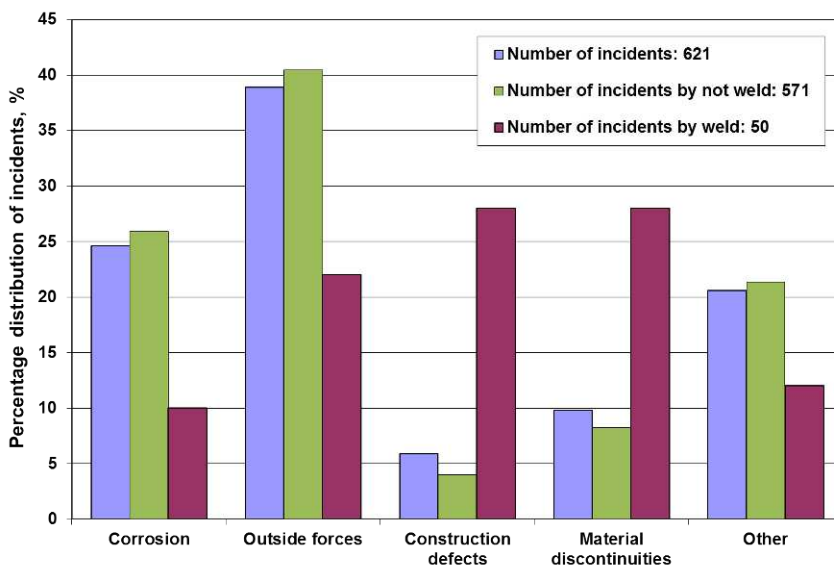
Figure 1
Pipeline incident distributions by cause [8]

Unfortunately, the Hungarian failure statistics [9] demonstrate a more negative picture than the international data. The comparison of the international and the Hungarian data show, on the one hand, that the ratio of the weld defects in Hungarian hydrocarbon transporting pipelines is higher than the international practice; on the other hand, weld defects typically occur in girth welds. This statement can be applied to both the past and the present.

The following figures show three examples of damages on girth welds in Hungary. Figure 2 illustrates a DN400, Figure 3 a DN600, and Figure 4 a DN800 gas transmission pipeline girth weld damage.

Figure 2

The damaged area of a girth weld on a Hungarian DN400 pipeline: crack in a repaired girth weld.
Pipeline materials designation by API 5L: Grade B and X52

Figure 3

The damaged area of a girth weld on a Hungarian DN600 pipeline: crack caused by repair and
unforeseen (not planned) cyclic loads. Pipeline materials designation by API 5L: X52 and X60

Figure 4

The damaged area of a girth weld on a Hungarian DN800 pipeline: crack caused by geometrical irregularities and unforeseen (not planned) cyclic loads, and initiated in the intersection point of a girth weld and spiral weld. Pipeline material designation by API 5L: X65

The different defects of girth welds can be classified into three groups of acceptability [10-12]: (i) defect acceptable by the assessment rules (workmanship criteria) of welded joints; (ii) defect unacceptable by the assessment rules of welded joints, but having no influence on the Fitness for Purpose (FfP) or Fitness for Service (FfS) of the welded joint; (iii) defect influencing the FfP or FfS of the welded joint. Based on the pipeline girth welds characteristics, these groups require different approaches [13] [14]. The girth weld integrity puzzle (see Figure 5 [15]) summarizes these characteristics, and demonstrates that the girth weld integrity depends on several interacting factors.

Forasmuch as there are several influencing factors on the failures, consequently on the integrity of pipeline girth welds, there are different opportunities for prevention of the damages, too. These opportunities can be divided into three groups [16]: (i) observance of the technological discipline and prescriptions; (ii) applying Engineering Critical Assessment (ECA) methods; reinforcing the girth welds, primarily using additional non-thermal, non-welded methods (e.g., composite wrap systems, non-welded sleeves as temporary or permanent repairs). The ECA methods reflect the operational experiences, demonstrate and endorse the compromise of rational risk and striving for safety, apply the results of the non-destructive testing (NDT), and should be validated by the results of full-scale tests on relevant pipeline sections. As the girth welds of pipelines are subjected to external loads in addition to internal pressures due to construction and operational reasons (e.g., ground movement), full-scale tests should be carried out taking this into account.
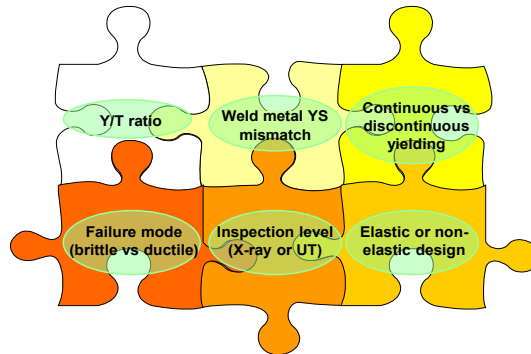
Figure 5
Puzzle of girth weld integrity [15]

The purpose of this article is twofold. On the one hand, we present a test system developed to investigate full-scale pipeline sections subjected to cyclic internal pressure and static external bending. On the other hand, we describe the results obtained from tests of girth welds with artificial notches. The results are used to draw conclusions on the load bearing capacity and integrity of the girth welds.

2   Experimental Setup and Testing Circumstances

Full-scale tests have important role during the assessing of the integrity of girth welds. These investigations should reflect the real operating conditions. This means that, in addition to internal pressure and its variation, external loads need to be modelled.

2.1   Experimental Setup

There are two testing systems for pressure vessels and piping at the Institute of Materials Science and Technology, University of Miskolc. Both systems are computer controlled electro-hydraulic setups; the newest system can be used up to 100 bar, and the oldest up to 700 bar internal pressure. The investigated pressure vessels or pipeline sections are located in a pit outside the laboratory building; all other components of the systems are located inside. The block diagrams of the lower-pressure and the higher-pressure systems are shown in Figures 6 and 7, respectively. The logical structure of the two systems is identical; the regulation and the control of the pressure were implemented during the whole tests in a closed loop.

J. Lukács *et al.*
Full-scale Fatigue and Burst Tests on Notched Pipeline Girth Welds
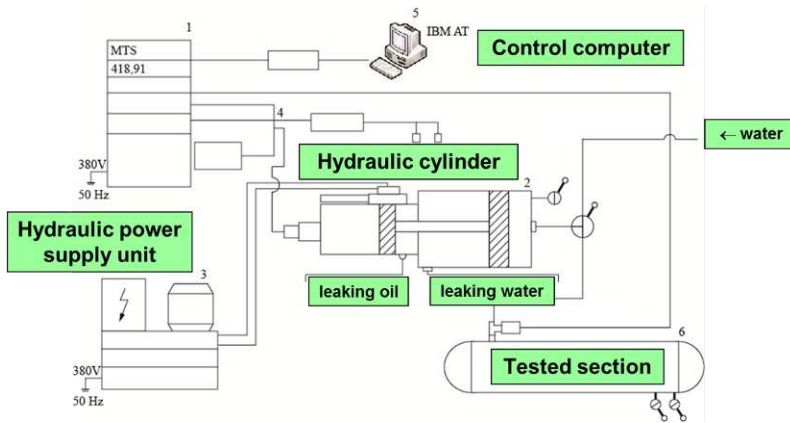under Complex Loading Conditions

Figure 6

The block diagram of the lower-pressure testing system with a maximal applicable pressure of 100 bar
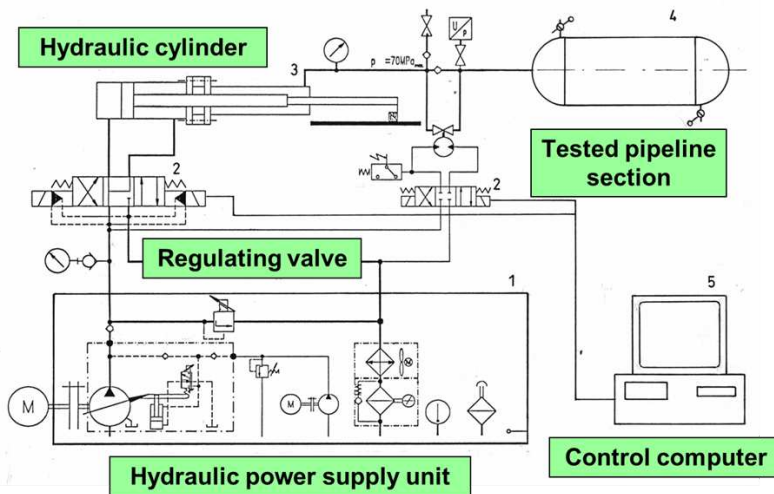

Figure 7

The block diagram of the higher-pressure testing system with a maximal applicable pressure of 700 bar

Based on these capabilities, a unique testing system has been developed for the complex loading of pipeline sections, applying cyclic internal pressure and superimposed external bending. In the three-point bending (3PB) layout, the tested girth weld was positioned in the middle of a nominal 4 meters long pipeline section. The experimental setup can be seen in Figure 8.
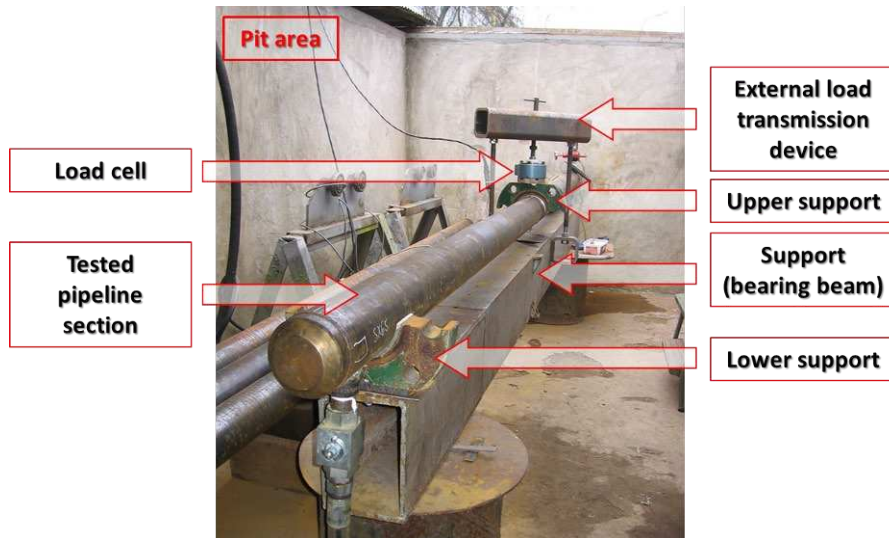
Figure 8

The pit area of our developed system for testing of pipeline sections under complex loading

The superimposed bending load was set via a load cell and checked by using a deflection meter (see Figures 9 and 10).
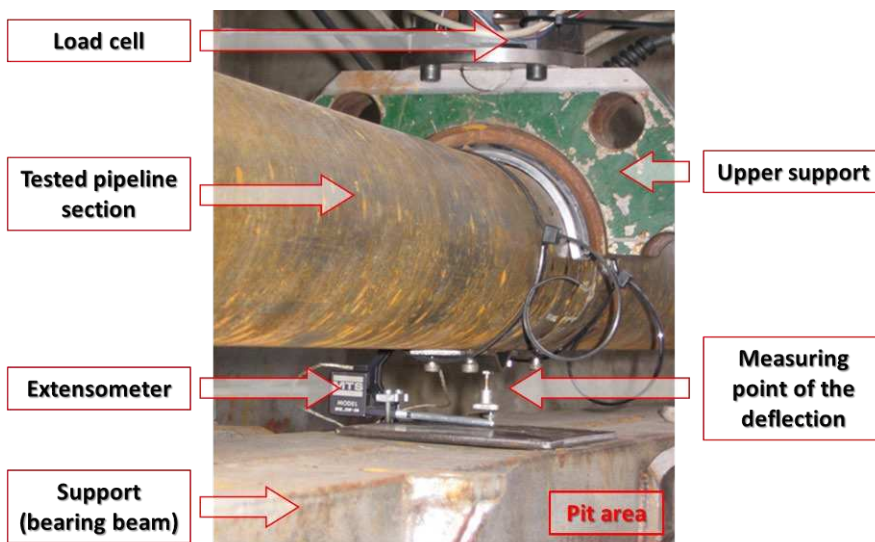

Figure 9

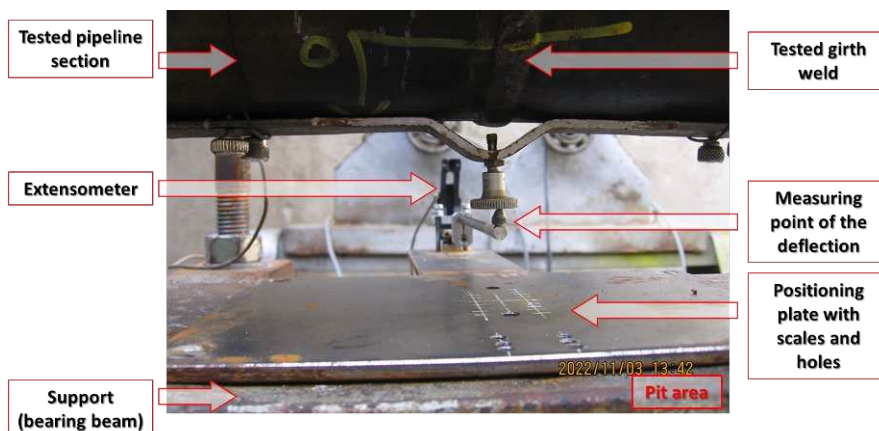Setting the deflection by load cell and its measuring by extensometer

Figure 10
Measuring the deflection by extensometer

Two video cameras were used for the recording of the burst process; the one recorded the process parallel and the other one perpendicular to the longitudinal axe of the investigated pipeline.

2.2   Testing Circumstances

The investigated pipeline sections were made of P355NH steel [17] with a nominal diameter of DN100 (114.3 mm) and with a nominal wall thickness (t) of 5.6 mm. The chemical composition of the pipe material can be found in Table 1.

Table 1
Chemical composition of the pipe material based on inspection certificate, weight%

C	Mn	Si	P	S	Cu	Cr
0.18	1.24	0.22	0.016	0.009	0.19	0.08
Ni	**Al**	**Mo**	**Ti**	**V**	**Nb**	**N**
0.06	0.027	0.02	0.001	0.004	0.000	0.090

The tested girth welds were made by manual metal arc welding (MMAW). The chemical composition of the used welding electrodes were summarized in Table 2, and the main characteristics of the welding process can be found in Table 3.

Table 2
Chemical composition of the applied filler metals based on company specifications, weight%

Filler metal	C	Si	Mn	Mo
Böhler FOX CEL – E 38 3 C 2 1	0.12	0.14	0.5	N/A
Böhler FOX CEL Mo – E 42 3 Mo C 2 5	0.1	0.14	0.4	0.5

Table 3
Main characteristics of the manual metal arc welding process

Layer	1st (root)	2nd	3rd
Position	PH	PJ	PJ
Filler metal	Böhler FOX CEL	Böhler FOX CEL Mo	
Diameter, mm	3.2	3.2	3.2
Current, A	DC/EN 45-55	DC/EP 55-70	DC/EP 50-65
Voltage, V	21.8-22.2	22.2-22.8	22.0-22.6
Welding speed, cm/min	7-12	15-20	10-15

The girth welds were inspected before the investigations by visual testing (VT), liquid penetrant testing (PT), and radiographic testing (RT). Only girth welds that have been produced to an acceptable quality level based on the specification of the Hungarian pipeline system operator (FGSZ Ltd.) have been tested. Consequently, the evenly high quality of the girth welds made it possible to investigate the impact of not resulting from welding influencing factors on the failure characteristics.

Five pipeline sections were tested, one of them without and four with artificial notches. The notches were cut using a hand grinding machine and located either in the heat-affected zone (HAZ) of the girth weld (circumferential direction) or through the girth weld (axial direction). Transporting pipeline operator experiences have shown that external undercuts and lack of fusions (between the base materials and weld metals) are common in poor quality girth welds. These defects were modelled using circumferential notches. Furthermore, transporting pipeline operator experiences have demonstrated the high incidence of longitudinal defects and their increased risk in welds (girth and spiral welds). The interaction of these defects with girth welds were modelled by longitudinal notches. Since the notches were made with the same hand grinder, their maximum nominal width was 2 mm. The shape of the notches followed the shape of the grinding wheel, with the width dimension narrowing slightly in the direction of depth (see left part of Figure 11).

For all pipeline sections, external bending loads were applied during the cyclic loading (100,000 cycles) and the burst test. The cyclic internal pressure was varied between 60% and 100% of the maximum allowable operating pressure (MAOP, 64 bar) with the lower-pressure system (see Figure 6). The applied axial stress from bending was four times and six times the axial stress from the maximum internal pressure ($\sigma_a = 29$ MPa), and were designated as 4 sigma and 6 sigma in relevant figures of the manuscript. The applied frequency during the fatigue test was 0.2 Hz. Furthermore, the testing media during both the fatigue and the burst tests was water, and the testing temperature was 15-25 °C. Due to changes in the ambient temperature, the test temperature was varied within a narrow range throughout the whole test program, this change in itself had no significant effect

on the behavior of the tested pipeline sections, their fracture mode was not changed. Table 4 summarizes the main characteristics of the full-scale tests.

Table 4

Main characteristics of the full-scale pipeline tests

Pipeline section ID	Applied bending stress	Notch location	Notch direction	Notch depth	Notch length, mm
Y6	$4 * \sigma_a$	N/A	N/A	N/A	N/A
Y7	$4 * \sigma_a$	girth weld HAZ	circumferential	$0.37 * t$	29
Y8	$4 * \sigma_a$	through girth weld	axial	$0.5 * t$	41
Y9	$4 * \sigma_a$	girth weld HAZ	circumferential	$0.67 * t$	40
Y10	$6 * \sigma_a$	girth weld HAZ	circumferential	$0.5 * t$	30

Figure 11 shows a notch in a girth weld HAZ (Y9 pipeline section) and through a girth weld (Y8 pipeline section) as examples.

Figure 11

Notch in the girth weld HAZ of the Y9 pipeline section (left) and through the girth weld of the Y8 pipeline section (right)

For the fatigue tests, the system with a maximum applicable pressure capacity of 100 bar was used (see Figure 6). Before starting the fatigue tests, the axial stress value from bending was set for each pipeline section separately. During this time, the load-deflection data pairs were continuously recorded to check the consistency of the theoretical and practical values. These curves are shown in Figure 12. On the one hand, the curves show the differences in deflection due to the difference in external load, and on the other hand, they demonstrate the almost identical behavior of the pipe sections under external load.

During the fatigue tests, the changes in the internal pressure and the deflection values and their variation were continuously monitored. These values were

recorded using a data acquisition system every 5,000-10,000 cycles, applying a time interval of 50-70 fatigue cycles (equal to 250-350 s). In Figures 13 and 14 can be seen examples from the Y10 pipeline section. Figure 13 illustrates the consistency of internal pressure and deflection variation, and both figures confirm the stability of the deflection variation. (It should be remembered that the fatigue tests were carried out over a period of more than four days per pipe section.)
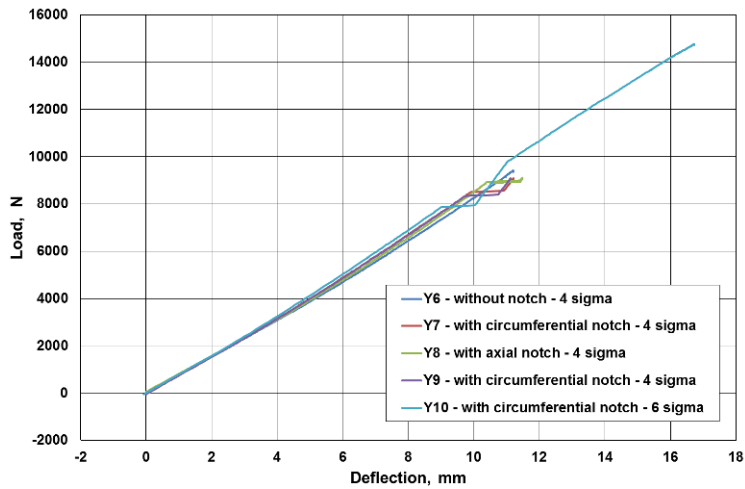

Figure 12

Load-deflection curves before the fatigue tests for setting the axial stress values from bending: the applied axial stress from bending was four times (4 sigma) and six times (6 sigma) the axial stress from the maximum internal pressure

Figure 13

Part of the screen of the MTS control system: main testing parameters, sinusoidal type programmed internal pressure (blue curve), recorded displacement from the extensometer (red curve)
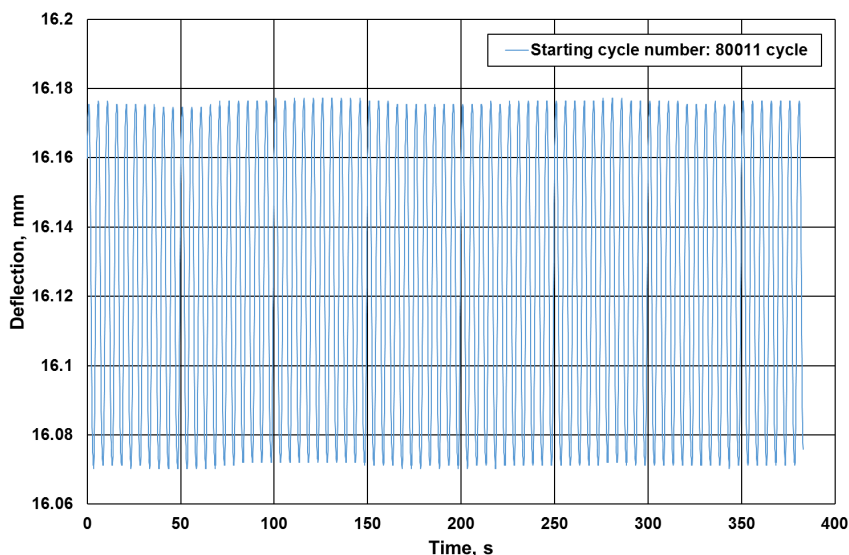
Figure 14

Change of deflection value during fatigue test (Y10 pipeline section) from number of cycles 80011, on the fourth day of the continuous fatigue test

After the fatigue tests, visual testing (VT) and liquid penetrant testing (PT) were performed, and the radiographic testing (RT) was repeated; the results showed no changes in any of the cases. This means that the fatigue stage did not cause a significant change in the quality of the girth welds tested.

For the burst tests, the system with a maximum applicable pressure capacity of 700 bar was used (see Figure 7). The internal pressure values were registered during the burst tests per second.

3   Results

The following diagrams and figures (Figures 15-17) introduce the results of the full-scale burst tests; furthermore, a table (Table 5) summarizes the results.

Figure 15 illustrates the average deflection vs. fatigue cycle number curves for each pipeline section, which are derived from the systematic processing of diagrams similar to the type of diagrams shown in Figure 14. The curves for both the 4 * σ_a and 6 * σ_a stresses and the circumferential and axial notches are clearly distinguished in the figure. It is remarkable that the curves have the same trend and are consistent with the approach.
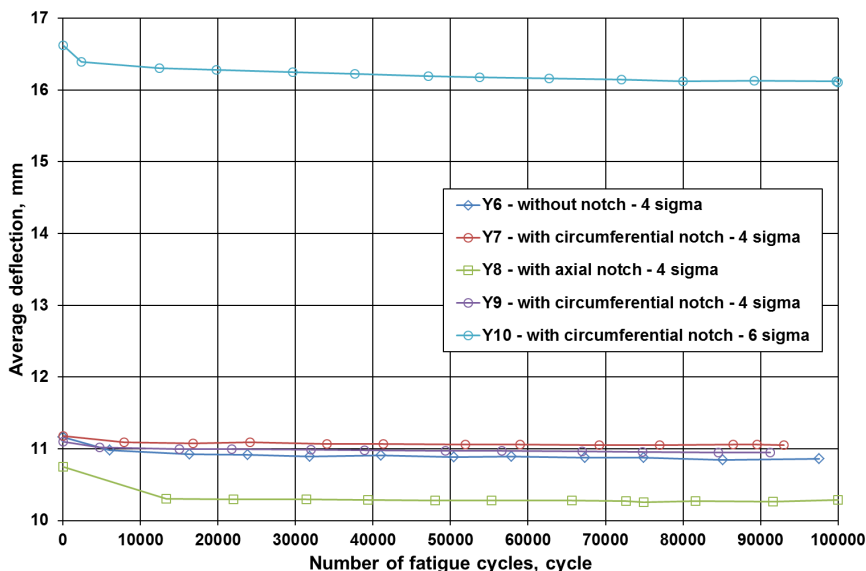
Figure 15
Change of the average deflection values during the fatigue tests

Figure 16 introduces the internal pressure vs. burst test time diagrams for the investigated pipeline sections. The average pressure growth rate values in the first stage can be evaluated as quasi-static values; therefore, the change in pressure cannot be considered as a dynamic effect. The other characteristics of the diagrams are the same, except for the diagram of the Y8 pipeline section. The tines-like changes of the diagrams demonstrate the volume increase of the pipeline sections in a consequence of the elastic-plastic deformation; during these periods, the system draws water from the water supply network. The damage to the tested pipeline sections, with the exception of the Y8 pipeline section, occurred on the pipe surface away from the investigated girth weld. The exception, pipeline section Y8, was damaged by splitting at the axial notch without significant volume increase. This is the reason for the lack of tines-like sections in the Y8 curve in Figure 16, and furthermore, for the shorter burst test or failure time.

The different failure behavior of the Y8 pipeline section compared to the other sections also highlighted the differences in the behavior of the different directions of the defects (in our case, notches) and their hazardousness. Of course, there is a close correlation between the location and size of the notches and the burst pressure, assuming other conditions are constant. The investigations confirmed that axial defects carry a higher risk than circumferential defects.
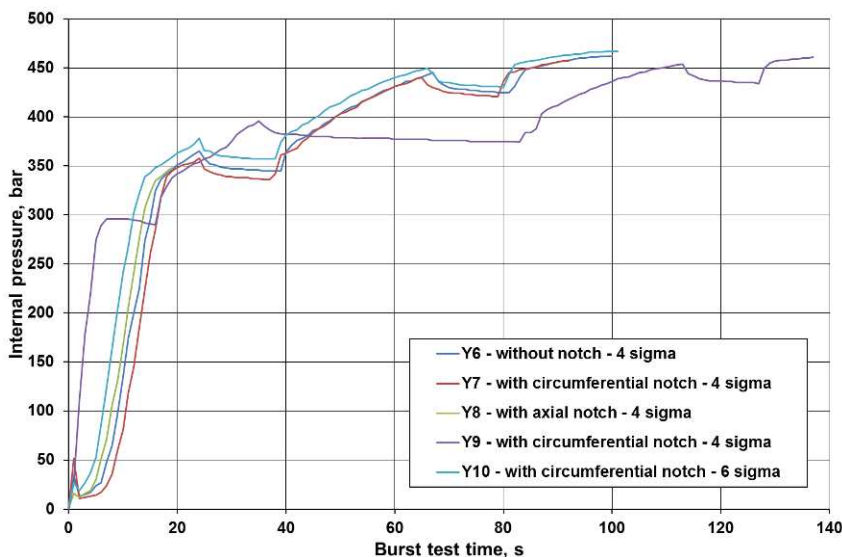
Figure 16

Internal pressure vs. burst test time diagrams of the investigated pipeline sections

A safety factor was defined to characterize the failure of the pipeline sections, with the following equation:

Safety Factor = Burst Pressure / Maximum Allowable Operating Pressure   (1)

Table 5 summarizes the notch characteristics; the burst pressure and the safety factor values of the investigations. The safety factor of the pipeline sections containing notch but not burst at the girth weld was almost the same.

Table 5

Notch characteristics, burst pressure and safety factor values of the full-scale pipeline tests.

Pipeline section ID	Notch characteristics	Burst pressure, bar	Failure location	Safety factor, –
Y6	N/A	462	pipe surface	7.22
Y7	circumferential in girth weld HAZ	457	pipe surface	7.14
Y8	axial through girth weld	348	axial notch through girth weld	5.44
Y9	circumferential in girth weld HAZ	461	pipe surface	7.20
Y10	circumferential in girth weld HAZ	467	pipe surface	7.30

The investigated pipeline sections at the end of their burst tests, at the moment of their failures, can be seen in Figure 17. The details of the figure show same

characteristics, only the pipeline section containing the longitudinal notch remained in place until the end of the burst test.

Y6 pipeline section

Y7 pipeline section

Y8 pipeline section

Y9 pipeline section

Y10 pipeline section

Figure 17
The pipeline sections at the moment of their failures

Figure 18 shows a closer look of the damaged area of the Y8 pipeline section.

Figure 18
The damaged area of the Y8 pipeline section after the fatigue and burst tests

Conclusions

The developed test system (Section 2.1) is suitable for testing full-scale pipeline sections with girth welds, subjected to cyclic internal pressure and superimposed external bending.

The failure of the tested unnotched and circumferentially notched pipeline sections occurred similarly, in all cases, away from the investigated girth weld and in the pipe surface, regardless of the notch depth and the magnitude of additional stress from bending. Failure of the pipeline section containing the axial notch in the investigated girth weld occurred in the notch at significantly lower pressures in the other pipeline sections.

The executed full-scale tests and the determined safety factor have confirmed the high load-bearing capacity of the girth welds produced to the required quality. This also implies that previous industrial damages have occurred in girth welds of unacceptable quality and/or subjected to significantly higher overloads.

The investigations and their results have confirmed that further full-scale tests should be executed in the near future, as follows. Pipeline sections with girth weld should be investigated applying higher axial stresses from the superimposed external bending as well as using deeper and/or longer artificial notches on the tensile bending stress side of the girth weld. The effect of temperature should also be investigated, given that the temperature at the laying depth is 8 °C and that the pipelines have above-ground sections. As the explicit intention is to blend hydrogen into the natural gas transporting system [18], it is necessary to extend the full-scale tests, to the transported medium. Although it seems realistic to consider these impacts separately, in the near future, in the medium term, we should be prepared to consider them together.

Acknowledgement

References

[1]   ASME B31.4: Pipeline Transportation Systems for Liquids and Slurries, The American Society of Mechanical Engineers, 2022

[2]   ASME B31.8: Gas Transmission and Distribution Piping Systems, The American Society of Mechanical Engineers, 2022

[3]   API Recommended Practice 1111: Design, Construction, Operation, and Maintenance of Offshore Hydrocarbon Pipelines (Limit State Design), American Petroleum Institute, September 2015

[4]   MSZ EN 1594: Gas supply systems. Pipelines for maximum operating pressure over 16 bar. Functional requirements, 2009

[5]   26/2022. (I. 31.) SZTFH rendelet a szénhidrogén szállítóvezetékek biztonsági követelményeiről és a Szénhidrogén Szállítóvezetékek Biztonsági Szabályzatáról (SZTFH regulation on safety requirements for hydrocarbon transmission pipelines and on Safety Regulations for Hydrocarbon Transmission Pipelines)

[6]   API Standard 1104: Welding of Pipelines and Related Facilities, American Petroleum Institute, July 2021

[7]   EPRG Guidelines on the Assessment of Defects in Transmission Pipeline Girth Welds – Revision 2014, European Pipeline Research Group e.V., 2014,   https://www.eprg.net/fileadmin/EPRG_public/eprg-docs/guidelines/EPRG_Weld_Defect_guidelines.pdf

[8]   Eiber, R. J., Jones, D. J.: An analysis of reportable incidents for natural gas transmission and gathering lines, June 1984 through 1990. Technical Report, NG-18/200, Battelle, Columbus, 1992

[9]   Chován, P.: Safety philosophy in the construction of gas pipelines. XXV. DUNAGÁZ Szakmai Napok Konferencia és Kiállítás (XXV. DUNAGÁZ Trade Days, Conference and Exhibition), Visegrád, Hungary, 2017. április 19-20 (In Hungarian)

[10]   Denys, R. M.: Girth-weld defect qualification methods need to be rationalized. Part 1: Focusing on mechanical properties in Engineering Critical Assessment saves money. Pipe Line and Gas Industry, Vol. 82, No. 9, September 1999. pp. 35-41

[11]   Denys, R. M.: Weld-defect acceptance models need more validated inputs. Part 2: Using good mechanical, toughness and defect-size data could reduced unneeded repairs. Pipe Line and Gas Industry, Vol. 82, No. 10, October 1999. pp. 59-64

[12]   Denys, R. M.: Standard weld-defect judging model needs some research. Part 3: Industrywide cooperation could lead the way to fewer unneeded repairs of girthweld defects. Pipe Line and Gas Industry, Vol. 82, No. 11, November 1999. pp. 69-74

[13]   Denys, R. M.: Consensus on judging multi-level weld defects would benefit all. Part 4: Economics may eventually be the lever to bring a change from current assessment methods. Pipe Line and Gas Industry, Vol. 82, No. 12, December 1999. pp. 60-65

[14] BS 7910: Guide to methods for assessing the acceptability of flaws in metallic structures, British Standards Institution, 2019

[15] Nagy, Gy., Lukács, J., Török, I.: Assessment of Methods in Girth Welds of Steel Pipelines, Materials Science Forum, Vol. 473-474, pp. 243-248, 2005, https://doi.org/10.4028/www.scientific.net/MSF.473-474.243

[16] Dakhel, A. Y., Lukács, J.: How to prevent damages of transporting pipeline girth welds? Multidiszciplináris tudományok, Vol. 11, Is. 4, pp. 208-217, 2021, https://doi.org/10.35925/j.multi.2021.4.25

[17] MSZ EN 10216-3: Seamless steel tubes for pressure purposes. Technical delivery conditions Alloy fine grain steel tubes, 2013

[18] Hungary's National Hydrogen Strategy – Strategy for the Introduction of Clean Hydrogen and Hydrogen Technologies to the Domestic Market and for Establishing Background Infrastructure for the Hydrogen Industry, 2021, https://cdn.kormany.hu/uploads/document/a/a2/a2b/ a2b2b7ed5179b17694659b8f050ba9648e75a0bf.pdf

Improving Optimization-based Inverse Analysis using Direct Inverse Maps: A Dynamic Damage Identification Case Study

Grant Stephens and Daniel Nicolas Wilke

Emerging Engineering Technology Laboratory, Department of Mechanical and Aeronautical Engineering, University of Pretoria, Pretoria, South Africa, 0086; grant@stephens.co.za; nico.wilke@up.ac.za

Abstract: Inverse problems in engineering form routinely part of larger engineering simulations. Therefore, the quality of the solution to an inverse problem directly influences the quality of the larger simulation and, ultimately, the ability to solve an engineering problem. Inverse problems can be challenging and time-consuming to solve, as most inverse strategies require iteration due to the non-linear nature of the problem. As a result, they often remain poorly solved before proceeding to the larger analysis. The quality of the solution to an inverse problem is influenced by the inverse strategy, scaling of the problem, scaling of the data, and initial guesses employed for iterative strategies. Research has focussed considerably on inverse strategies and scaling. However, research into strategies that improve initial guesses of an inverse problem has been largely neglected. This study proposes an elegant strategy to improve the initial guesses for conventional optimization-based inverse strategies, namely direct inverse maps (DIMs) or inverse regression. DIMs form part of modern multivariate statistics. DIM approximates the solution to an inverse problem using regression; popular choices are linear regression, e.g., partial least squares regression (PLSR). These strategies are not iterative but require several independent a-priori simulations to have been conducted. As they are not iterative, one way to improve the solution is to increase the number of independent a-priori simulations to be conducted. Our proposed strategy is to use DIM to generate initial guesses for optimization-based inverse strategies. We conduct a parameter investigation on a truss structure's virtual vibration-based damage identification problem.

Keywords: Inverse Problem; Virtual Inverse Problem; Direct Inverse Maps; Partial Least Squares Regression; Optimization; Starting Point; Initial Guess

1 Introduction

Inverse analysis is prevalent in engineering analysis, as the characterization of models is routinely part of a larger analysis or simulation. The characterization of the models significantly influences the simulation quality. It is common for

engineers to focus on the analysis or simulation without properly characterizing some of the models used in simulations.

Inverse problems in engineering form routinely part of larger engineering simulations. Therefore, the quality of the solution to an inverse problem directly influences the quality of the larger simulation and, ultimately, the ability to solve an engineering problem. Inverse problems can be challenging and time-consuming to solve, as most inverse strategies require iteration due to the non-linear nature of the problem. As a result, they often remain poorly solved before proceeding to a larger analysis. The implication is usually disastrous, as conclusions drawn from the numerical work may not be valid. In addition, the solution quality for an inverse problem can be influenced by the inverse strategy, loss surface complexity, scaling of the data, and initial guesses employed. Most research has focused on inverse strategies and scaling of data. However, research into strategies that improve initial guesses of an inverse problem has been largely neglected.

This study focuses on and proposes an elegant strategy to improve the initial guesses for the ubiquitous optimization-based inverse strategies using the lesser-known direct inverse maps or direct inverse regression strategies [1]. DIMs can be broadly categorized as either iterative optimization-based or non-iterative regression-based approaches.

Optimization-based inverse strategies are well-known and ubiquitous in research and industry; in particular, weighted least-squares are considered a classical inverse analysis approach. Optimization-based inverse strategies start from an initial guess and iteratively improve the model parameters by minimizing some non-linear error and quantifying the difference between experimental and simulated responses until convergence. The sum of the error squared is a classical error measure often employed. Optimization-based inverse solution strategies can become computationally expensive when multiple local minima exist. Confidence in the solution is usually ensured by conducting multiple minimizations using gradient-based and evolutionary strategies in a multi-start procedure. In extreme cases, a multi-start approach may be required to obtain a converged or feasible solution, for instance, when an optimizer traverses model parameters that fail to analyze along a search path. However, a significant benefit of the minimization-based inverse strategies is that the error between the predicted and experimental response is reduced iteratively.

DIMs, in turn, are not so well known as they are rooted in modern multi-variate statistics [1, 2]. These strategies regress the experimental response directly to the model parameters without the need to iterate. Although these strategies are not iterative, they require a regression set of model parameters and their respective responses, usually constructed by simulation. DIM is, therefore, susceptible to extrapolation from the regression set when noise (aleatoric) and model (epistemic) mismatches exist between the experimental response and simulated responses in the regression set. The simulated response can then be computed using the model

parameters. Supplementing the regression set with additional simulated responses may improve the regression quality, but it is not guaranteed. The improvement depends on the similarity between the simulated responses in the regression set and the experimental responses regressed to the model parameters. The benefits and pitfalls of DIMs are detailed in [1]. Mature strategies quantify and address both aleatoric (noise) and epistemic (model mismatches) errors.

They include principal component regression (PCR) [3-5] and partial least squares regression (PLSR) [3, 6-8]. The optimization-based iterative and regression-based non-iterative inverse strategies are utilized in isolation [2, 9, 10]. The classical optimization-based inverse approach usually uses uniform or normally distributed initial starting points over an anticipated model parameter space [11]. Alternatively, judgment, experience, or exploiting physics can inform suitable starting guesses, but this requires focused and qualified analysts. Alternatively, DIMs merely regress the response to the model parameters using a regression set [2, 9, 12]. Essentially, when these strategies are used in isolation, we have

1) multiple minimizations that are conducted in isolation and

2) large sets of independent simulated responses are generated to make up the regression set.

This study proposes a complementary unified approach from these two approaches. We use DIM to predict starting points for a gradient-based inverse procedure that iteratively minimizes some nonlinear scalar error measure, which in this study is demonstrated for the sum of the error squared.

The benefit is that the computational cost to solve an inverse problem may be reduced and the robustness enhanced. We specifically consider partial least squares regression (PLSR) to predict the initial starting point when minimizing the sum of errors squared using a gradient-based minimizer. The robustness and the computational cost of solving optimization-based inverse problems are directly related to the quality of the initial starting points supplied to the optimizer. Of course, numerous strategies exist to improve the robustness of solving inverse problems. Examples include response surfaces [23] and lower fidelity models [21], which will benefit from improved starting points for the minimization strategy.

We consider a virtual inverse problem [21-22, 1] where we simulate the problem with and without simulated noise (aleatoric uncertainty) on the computed response. The benefit of knowing the solution is that we can properly quantify the performance of the various strategies in identifying the correct parameters. Since the considered approaches see the same problem, we can draw sensible conclusions in our comparisons between approaches. This study evaluates the dynamic identification of damage in a 25-bar truss structure [13].

2   Minimisation Inverse Strategy

Minimization-based inverse strategies predict the unknown model parameters by minimizing some scalar error measures between the experimental and simulated response.

The difference between the experimental and predicted response results in an error vector. The error vector can be reduced into a scalar form, e.g., the sum of the errors squared or stated as the square of the L_2-norm, resulting in the familiar least squares problem. The least squares problem is an unconstrained minimization problem usually solved using a Quasi-Newton minimizer [23].

Alternatively, the error vector can be the constraint in a min-max optimization problem where the maximum error is minimized. Here, the L_∞ norm is usually minimized [15]. The objective function is linear by construction, but each point in the predicted response is a constraint. This constrained problem is generally solved using an augmented Lagrangian strategy [23].

This study is limited to least squares minimization but can be applied to various error measures.

3   Direct Inverse Maps

DIM regresses an observed experimental response to unknown model parameters. Various DIM strategies exist. The most popular are based on high dimensional linear regression constructed from a regression set. The regression set contains model parameters and their respective responses. The regression set is usually computed by simulation of a representative model. The regression strategies include principal component regression (PCR) [3-5, 8] and partial least square regression (PLSR) [3, 6-8].

These approaches are not susceptible to co-linearity problems like multi-linear regression (MLR) as they also reduce the dimension of the problem by projection. Hence, many high-dimensional points can be used in the regression set [24]. Both PCR and PLSR require the size of the reduced dimension (number of modes or loadings) to be selected by the user [24]. For regression, it is often suggested to use the lowest number of modes such that the responses in the regression set describe the experimental response well. This implies that the projected experimental response onto the modes can be expressed by interpolating between the responses in the regression set that are also projected onto the modes. This is opposed to extrapolation, which indicates the response is an outlier to the points in the regression set.

In this study, we only consider partial least square regression. PLSR solves the following problem: and is given by the following algorithm PLSR is available in most numerical software packages such as Matlab (function `plsregress` in the Statistics and machine learning toolbox), R (`pls` package), and Python (module `PartialLeastSquares`).

4   Combined Strategy

Optimization inverse analysis and DIMs are generally used in isolation due to their historical origins. Instead of comparing these two approaches for their benefits and pitfalls, we demonstrate the potential benefits when unifying them to solve inverse problems. This approach can be applied when the simulation model is evaluated directly [22] or via a response surface [24]. In this study, we only consider the former approach to allow us to assess its merit without introducing additional complexities and uncertainties, such as the quality of the response surface. We note that should this approach prove beneficial in the absence of response surfaces, the additional benefits are evident when including response surfaces [23 - 25]. The simulated data points to construct a response surface can also generate initial starting points that might be less susceptible to local minima and more likely to lie within the global basin [26].

Our proposed strategy under investigation uses the PLSR as a DIM to compute the initial starting point for a classical Quasi-Newton gradient-based minimization algorithm. This process is repeated until convergence. Consider the algorithmic outline of our approach:

1 Estimate the expected domain for each input parameter X of the model. Initialize an empty design of experiments (DOE) XY. Choose N_{DOE} and N_{OPT}.

2 Compute N_{DOE} points and augment the DOE XY, using augmented Latin Hypercube Sampling (ALHS) over the expected parameter domain.

3 Predict the model input parameters X_P, from the experimental response Y_{EXP} using PLSR.

4 The predicted response is then used as an initial starting point for an iterative minimization approach $x0 = XP$ when there is a lower error than the best point in the regression set. Otherwise, the point with the lowest error in the regression set is used as an initial starting point. The minimizer is limited to N_{OPT} iterations. Here, we can include or discard the responses computed at each iteration to be used in the regression set for the next PLSR. In this study, we only include the point at iteration N_{OPT}.

5 Repeat steps 2-5 until convergence.

Note that if we choose $N_{DOE} = 1$, we recover an optimization-based inverse strategy with a single initial random guess. By choosing $N_{OPT} = 0$, we recover PLSR solely. This allows us to quantify the benefits of the independent and various blends of the unified strategy.

An additional parameter to N_{DOE}, $N_{OPT,}$ and the convergence criteria is the number of modes N_{MODES} to use for the PLSR. The number of modes N_{MODES} are estimated as follows:

1   Compute the participation coefficients (scores) of each mode (loading) for each point in the regression set.

2   For each loading estimate, the expected ranges for the participation coefficients.

3   Project the experimental response Y_{EXP} onto the first mode using standard least squares regression and compute the participation coefficient.

   a. If the participation coefficient of the first mode falls outside the expected range, use the data point in the set used to construct the PLSR with the least error as an initial optimization starting point; otherwise, continue.

4   Include the next mode in the projection and compute the participation coefficients.

5   Conduct the following convergence checks

   a. Check if the participation coefficients fall within the expected ranges.

   b. Check that the norm of the difference between the current and previously predicted model parameters decreased.

   c. Continue until a check fails and use all modes, excluding the last mode that failed a check.

6   Repeat 1-5 until a convergence check fails.

5   Numerical Investigation

We conduct a numerical investigation to assert the feasibility of solving inverse problems using the proposed approach of combining DIMs and minimizing the sum of the errors squared. By appropriately selecting N_{DOE} and N_{OPT}, we can investigate the two strategies in isolation and combined. In this study, we restrict ourselves to a virtual inverse problem [21-22, 1], using simulated experimental data instead of actual experimental data. The benefit is that we can critically assess the quality of the estimated model parameters and the responses' quality.

We effectively turn an unsupervised learning problem into a supervised learning problem through modeling.

We conduct the inverse analysis with simulation in the loop instead of the typical and appropriate response surface-based strategy [25-26]. This is done deliberately to investigate the proposed approach without adding the additional complexity and uncertainty that response surfaces may introduce into the investigation.

We consider the vibration-based damage identification of a 25-bar truss. We aim to estimate the mass of 25 trusses from the first two vibration modes given by the nodal displacements of the six nodes of the truss structure, resulting in a 36-dimensional response vector. We consider the simulated experimental response vector with and without simulated measurement noise.

5.1 Vibration-based Damage Identification of a 25-bar Truss

Vibration-based damage identification approaches aim to assess the integrity of structures non-destructively [13, 16-18]. Modal parameters (natural frequencies, mode shapes, damping, and modal strain energy) of a structure depend on the physical properties of the structure, i.e., mass, stiffness, and damping. The premise behind vibration-based damage identification is that changes in the physical properties manifest in changes to the modal parameters. Hence, changes in modal parameters can be used to locate and identify damage in a structure.

We consider a simple example in which we aim to estimate the effective mass (or equivalently, area) of the truss members from only the first two structural modes of a structure in a corrosive environment. The geometry and material properties are assumed to be known. A truss analysis without damping is considered sufficient to describe the dynamics of the structure, i.e., a lightly damped structure. The nodal displacements of the six nodes in three-dimensional space for two modes result in a 36-dimensional response vector.

The 25-bar truss structure [19] is depicted in Figure 1(a), and the first two modes are in Figures 1(b) and (c), respectively. The structure is fully constrained (in all three translational directions) at the four ground supports, as indicated in Figure 1(a). The truss modal analysis is conducted using an in-house finite element analysis code with direct and adjoint analytical sensitivities developed by Wilke for his Optimum Design (MOO780) graduate course at the University of Pretoria, South Africa, which solves the generalized eigenvalue problem

$$(K_{ff} - \lambda M_{ff})y = 0, \tag{1}$$

with K_{ff} and M_{ff}, the assembled system stiffness and mass matrices with the associated unconstrained degrees of freedom of the system. The experimental data in this vibration-based damage identification problem is simulated using the same code to conduct a virtual inverse problem.

This study considers simulated experimental data with and without measurement noise, i.e., aleatoric uncertainty. A normally distributed measurement noise of 2% for the first standard deviation was assumed. The experimental data is simulated for 1 kg masses for each of the 25 truss members, which results in a 487 Hz fundamental frequency and a second mode at 530 Hz. An unknown parameter range of 100% around the solution is considered for this study. The parameters to be estimated were normalized by the solution [20]. The error norm for the calculated response is 0.0 (within machine precision) in the absence of noise and around 0.5102 when 2% measurement noise is assumed.

(a) Undeformed truss structure with fixed points denoted by red dots.

(b) First (fundamental) vibration mode of the truss structure (487 Hz).

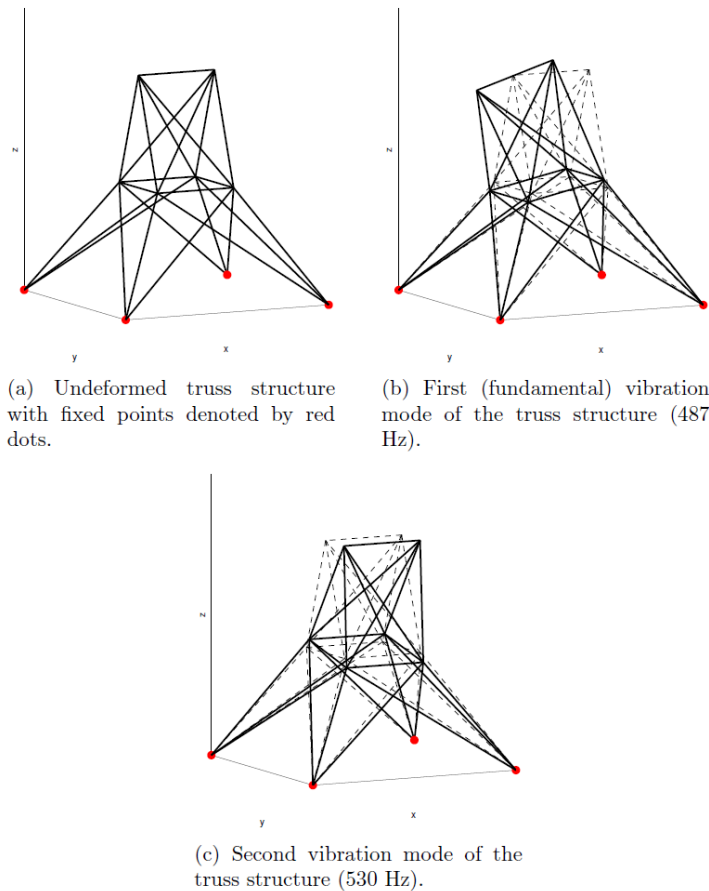(c) Second vibration mode of the truss structure (530 Hz).

Figure 1
(a) The undeformed truss structure and associated (b) fundamental at 487 Hz and (c) second mode at 530 Hz. The base (indicated by the solid red dots) is fixed to resist any translation.

6   Numerical Results

The numerical investigation aims to quantify our proposed strategy's performance and sensitivity to divide the effort between adding points to the N_{DOE} to improve starting points instead of allowing additional optimization iterations N_{OPT}. We investigate the benefits of splitting effort between the PLSR and iterative optimization without explicitly considering the associated computational cost to avoid distracting from this study. We limit ourselves to 500 function evaluations and consider the cost of each optimization iteration to be one function evaluation. Similarly, each point added to the DOE is regarded as one function evaluation. The benefit of this choice is that a user can scale the associated computational cost of an optimization iteration to DOE point computation independently afterward.

We consider a purely sequential computational framework, but the benefits of parallel environments are evident when increasing the number of points of the DIM, as it is embarrassingly parallel as opposed to the sequential nature of a classical gradient-based algorithm. However, these questions warrant an independent study to explore when a multi-core, GPU, or parallel computational architecture is considered. The implicit assumption of our choice is that function computations dominate the computational cost of these two problems, with sensitivities being available computationally efficiently either analytically or by differentiating a response surface representation of the cost function. In this study, adjoint analytical sensitivities are computed.

To conduct our study, we consider distinct ratios $N_{OPT}:N_{DOE}$ of the number of optimization iterations N_{OPT} to Latin hypercube sampled N_{DOE} points. The ratios we consider for both problems are 0:9, 1:9, 4:9, 1:1, 9:4, 9:1, and 100:1. A ratio of 0:9 implies that no optimization is conducted, and the response is computed using only PLSR. In turn, a ratio of 100:1 effectively results in an optimization strategy using random initial starting points. We conduct this for increments of $\Delta N_f = \{10, 25, 50, 100, 250, 500\}$ function evaluations per iteration for our combined strategy. When only PLSR is considered, we compute exactly ΔN_f function evaluations, whereas the optimization strategy with random initial starting points is limited to a maximum number of ΔN_f function evaluations. This is repeated until the maximum of 500 function evaluations is reached. Table 1 indicates the number of function evaluations available for PLSR and the least squares minimization strategy for the different choices of $N_{OPT}:N_{DOE}$ and ΔN_f.

The optimization algorithm used in this study is Matlab's SQP algorithm in the `fmincon` function. The convergence tolerance for the optimization algorithm was set to 10^{-6} for changes in updates or function values between updates.

Table 1

The available number of function evaluations (N_{DOE}, N_{OPT}) for the combined strategy per iteration for the selected ratios $N_{OPT}:N_{DOE}$ and ΔN_f

		ΔN_f					
		10	25	50	100	200	500
	0	(10,0)	(25,0)	(50,0)	(100,0)	(200,0)	(500,0)
	1 : 9	(9,1)	(22,3)	(45,5)	(90,10)	(180,20)	(450,50)
	4 : 9	(7,3)	(17,8)	(35,15)	(69,31)	(139,61)	(346,154)
$\frac{N_{OPT}}{N_{DOE}}$	1 : 1	(5,5)	(12,13)	(25,25)	(50,50)	(100,100)	(250,250)
	9 : 4	(3,7)	(8,17)	(15,35)	(31,69)	(61,139)	(154,346)
	9 : 1	(1,9)	(3,22)	(5,45)	(10,90)	(20,180)	(50,450)
	100 : 1	(0,10)	(0,25)	(0,50)	(1,99)	(2,198)	(5,495)

For each selected setting, we repeat the optimization run 100 times and depict the results in box plots for choices of ΔN_f. The box plots show the median (solid red line), with the box representing half the data points. The whiskers extend to the extreme data points that are statistically unimportant. Lastly, the red crosses indicate all the outliers.

We quantify the analyses' robustness and solutions' quality. The analyses of the 25-bar truss always succeeded.

6.1 Vibration-based Damage Identification of a 25-bar Truss

The final residuals obtained for the 100 independent runs after 500 total function evaluations are presented in Figures 2(a)-(g) and 3(a)-(g) for the noiseless and noisy simulated experimental data, respectively. Figure 4 shows the results after only 100 function evaluations to highlight the relative improvement from 100 to 500 function evaluations. In Figure 2(a), the PLSR predictions vary between two error levels. It is evident from the median position that divides the data points at the top or bottom of the box. In Figure 2(a), as expected, the same response for all ΔN_f is evident when considering the size and position of each box.

There is a definite benefit to selecting a lower NOPT:NDOE ratio for the noiseless simulated experimental data, except for a ratio of 0, which represents only PLSR. A larger ΔN_f seems to be consistently beneficial. The 0 ratio effectively represents the contribution of the PLSR in isolation, whereas the minimizer effectively realizes the remainder of the improvements. Note that a single optimization run is preferred, as consistently indicated by the better performance of the larger ΔN_f. It demonstrates the benefit of continuing the minimization after an appropriate initial guess has been provided. Additional PLSR regression points perform worse

than allowing additional iterations in the minimizer. However, an estimate of a proper initial point is important as minimization in isolation, similar to PLSR in isolation, performed the worst on average.
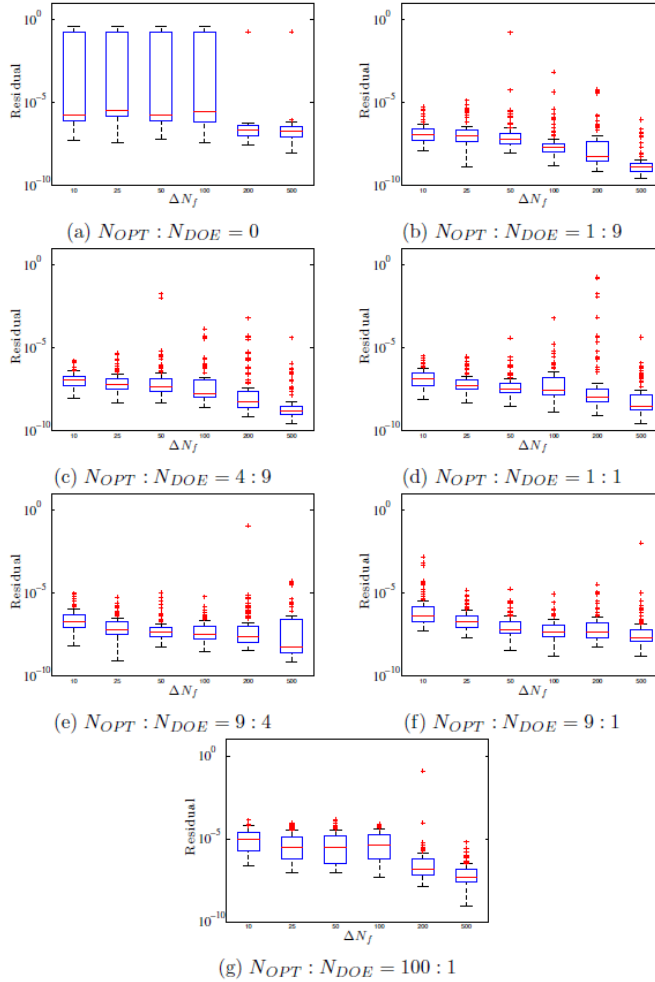

Figure 2

Residual box plots for 100 independent runs using the simulated experimental data without noise for the damage identification problem. The total number of function evaluations is 500 for the selected ratios $N_{OPT}{:}N_{ODE}$ (a)-(g). The choice ΔN_f is quantified in each subfigure.

This contrasts the simulated experimental data with noise, where the selection of a moderate ΔN_f yields better results on average. In addition, a ratio $N_{OPT}{:}N_{DOE}$ that favors the minimizer is beneficial. Note that suitable ratios $N_{OPT}{:}N_{DOE}$ allow for PLSR-estimated starting points instead of random initial starting points.

The implication is that multi-starts benefit this noisy problem, as indicated by a low to moderate value for ΔN_f.
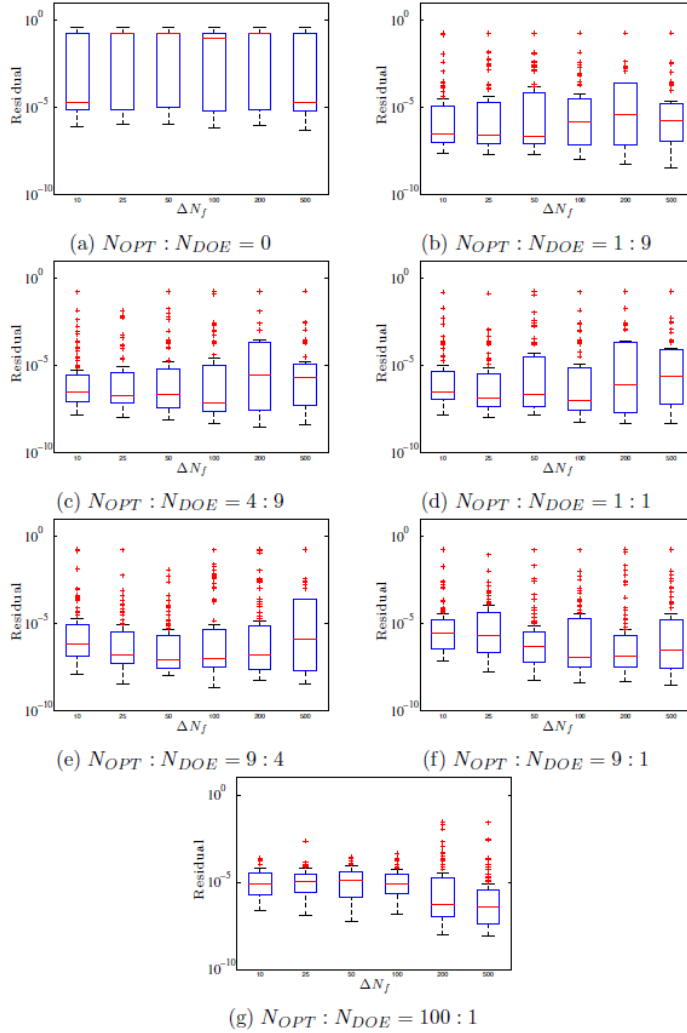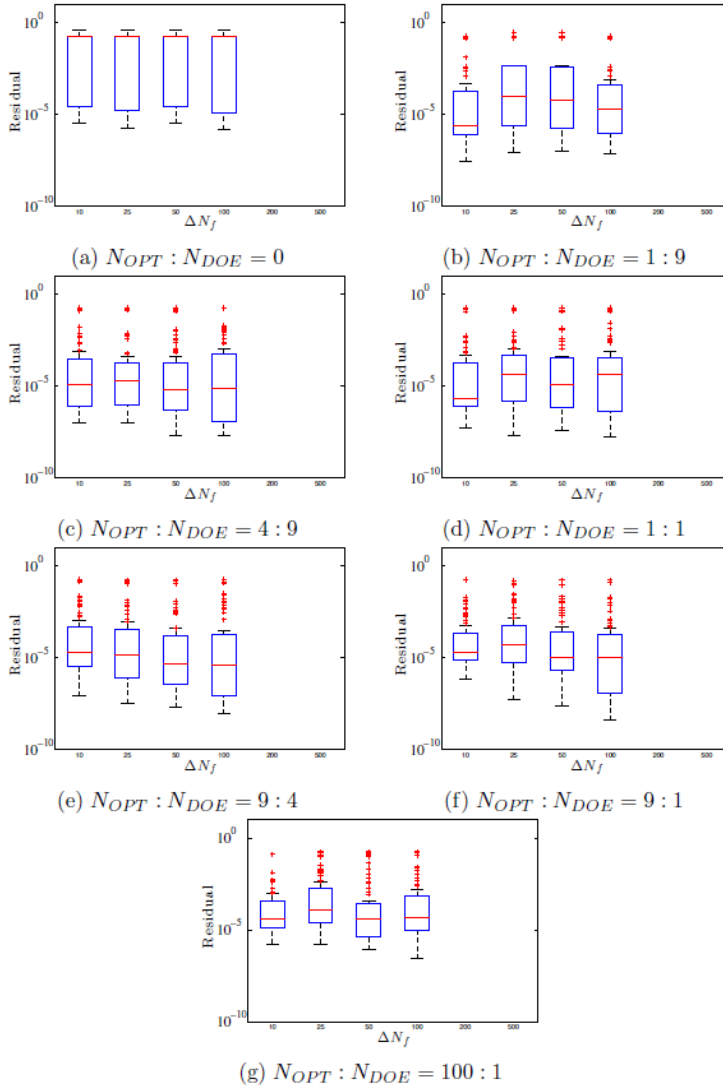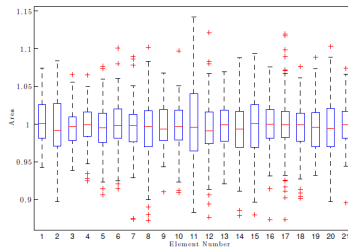

(a) $N_{OPT} : N_{DOE} = 0$

(b) $N_{OPT} : N_{DOE} = 1 : 9$

(c) $N_{OPT} : N_{DOE} = 4 : 9$

(d) $N_{OPT} : N_{DOE} = 1 : 1$

(e) $N_{OPT} : N_{DOE} = 9 : 4$

(f) $N_{OPT} : N_{DOE} = 9 : 1$

(g) $N_{OPT} : N_{DOE} = 100 : 1$

Figure 3

Residual box plots for 100 independent runs using the simulated experimental data with noise for the damage identification problem. The total number of function evaluations is 500 for the selected ratios $N_{OPT}{:}N_{ODE}$ (a)-(g). The choice ΔN_f is quantified in each subfigure.
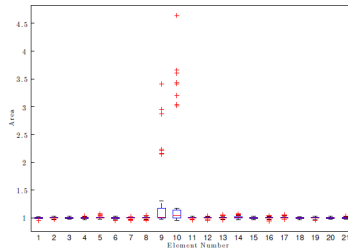
(a) $N_{OPT} : N_{DOE} = 0$

(b) $N_{OPT} : N_{DOE} = 1 : 9$

(c) $N_{OPT} : N_{DOE} = 4 : 9$

(d) $N_{OPT} : N_{DOE} = 1 : 1$

(e) $N_{OPT} : N_{DOE} = 9 : 4$

(f) $N_{OPT} : N_{DOE} = 9 : 1$

(g) $N_{OPT} : N_{DOE} = 100 : 1$

Figure 4

Residual box plots for 100 independent runs using the simulated experimental data with noise for the damage identification problem. The total number of function evaluations is 100 for the selected ratios $N_{OPT}:N_{ODE}$ (a)-(g). The choice ΔN_f is quantified in each subfigure.

Minimization in isolation ($N_{OPT}:N_{DOE}$ = 100:1) and PSLR in isolation ($N_{OPT}:N_{DOE}$ = 0) performs the worst. Notably, in isolation, the minimizer significantly reduces the number of outliers at the cost of a higher residual on average. The results obtained after 100 total function evaluations for the noisy simulated experimental

data are presented in Figure 4(a)-(g). This shows the progression of the decrease in residual and also how the various settings benefit from an additional 400 function evaluations that Figure 3(a)-(g) depicts.

We also present area variation as box plots in Figures 5(a) and 5(b) for a range of residual values. The solution is obtained when all the areas are 1, as seen in Figure 5(a). All values, including outliers, are within a 15% range of the solution. From Figure 5(b), the larger residuals are due to the minimizer poorly estimating the truss areas and not the PLSR-estimated initial guesses.

(a) Boxplot of Areas for each of the elements found by $N_{OPT} : N_{DOE} = 1{:}9$ and $\Delta N_f = 25$ with a range of residuals between 1.33×10^{-5} and 1.24×10^{-9}

(b) Box-plot of Areas for each of the elements found by $N_{OPT} : N_{DOE} = 1{:}1$ and $\Delta N_f = 200$ with a range of residuals between 0.1780 and 8.05×10^{-10}

Figure 5

Box-plots of the areas found by two different sets of data

To investigate the quality of the computed initial guesses as a function of the number of LHC points, we compute 100 initial guesses for various numbers of points in the regression set. The results are depicted in Figure 6. Note the significant benefit of a small sample size in the regression set.

The results presented demonstrate a computational benefit when unifying optimization-based inverse strategies and DIM. A benefit that is enhanced in the presence of experimental measurement noise.
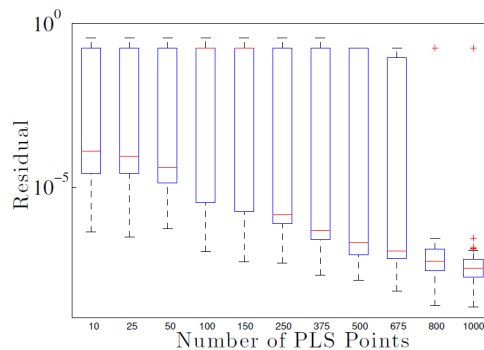
Figure 6

Boxplot of the residuals computed for 100 initial guesses for the optimization algorithm as the number of points in the regression set increases

Conclusion

This study demonstrated the benefit of unifying two inverse strategies: least squares minimization and the PLSR direct inverse map (DIM). Traditionally, these two strategies are considered separately, but this study demonstrates the benefits of unifying them into a complementary approach. Our proposed strategy unifies these two into a single strategy that allows each to be recovered in isolation. DIM is used to compute suitable initial guesses for the iterative optimization solver. For a practical inverse problem, we demonstrated that this combination results in computational benefits.

This unified approach demonstrated benefits when considering a sequential computing platform. The additional benefits of this approach on parallel computing platforms will only complement this strategy. This will be investigated in a future study to investigate and quantify each properly.

Future work will consider the benefits of this strategy in terms of robustness, as preliminary work on identifying ODEs on Calcium signaling pathways [14] only solves around 50% of the time when random starting points are used compared to 100% when combined with DIM. As future work will demonstrate, this unified approach can improve the robustness of the inverse problem when facing challenging problems or when limited resources are available.

References

[1]   Erfan Asaadi, Daniel N. Wilke, P. Stephan Heyns, and Schalk Kok. The use of direct inverse maps to solve material identification problems: Pitfalls and solutions. Struct. Multidiscip. Optim., 55(2):613-632, feb 2017

[2]   Wold S., Ruhe A., Wold H., and Dunn W. J. The collinearity problem in linear regression. the partial least squares (PLS) approach to generalized inverses. SIAM Journal on Scientific and Statistical Computing, 1984

[3]   W. J. Dunn III, D. R. Scott, and W. G. Glen. Principal components analysis and partial least squares regression. Tetrahedron Computer Methodology, 2(6):349-376, 1989

[4]   S. de Jong. SIMPLS: An Alternative Approach to Partial Least Squares Regression. Chemometrics and Intelligent Laboratory Systems, 18(6):251-263, 1989

[5]   I. Jolliffe. Principal Component Analysis. Springer-Verlag, 2nd edition, 2002

[6]   P. Geladi and B. R. Kowalski. Partial least-squares regression: a tutorial. Analytica Chimica Acta, 185:1-17, 1986

[7]   R. Rosipal and N. Kramer. Subspace, Latent Structure and Feature Selection: Statistical and Optimization Perspectives Workshop (SLSFS 2005). Lecture Notes in Computer Science 3940. Springer-Verlag, 2006

[8]   Hong-Dong Li, Yi-Zeng Liang, and Qing-Song Xu. Uncover the path from PCR to PLS via elastic component regression. Chemometrics and Intelligent Laboratory Systems, 104(2):341-346, 2010

[9]   F. Abbassi, T. Belhadj, S. Mistou, and A. Zghal. Parameter identification of mechanical ductile damage using artificial neural networks in sheet metal forming. Materials & Design, 45:605-615, 2013

[10]   M Rabinovich and D. M. Blei. The inverse regression topic model. In 31st International Conference on Machine Learning, 2014

[11]   Abeeb a. Awotunde. Estimation of well test parameters using global optimization techniques. Journal of Petroleum Science and Engineering, 125:269-277, 2015

[12]   Huber N. and Tsakmakis C. A neural network tool for identifying the material parameters of a finite deformation viscoplasticity model with static recovery. Computer Methods in Applied Mechanics and Engineering, 191:354-384, 2001

[13]   D. Dessi and G. Camerlengo. Damage identification techniques via modal curvature analysis: Overview and comparison. Mechanical Systems and Signal Processing, 52-53, 2015

[14]   C Solem, B Koebmann, and P R Jensen. Control analysis of the role of triosephosphate isomerase in glucose metabolism in Lactococcus lactis. IET systems biology, 2(2):64-72, 2008

[15]   K. Madsen and H. Schjaer-Jacobsen. Algorithms for worst case tolerance optimization. IEEE Transactions of Circuits and Systems, CAS-26, 1979

[16]   S. W. Doebling, C. R. Farrar, and M. B. Prime. A summary review of vibration-based damage identification methods. Structural Health Monitoring, 30, 1998

[17]   W. Fan and P. Qiao. Vibration-based damage identification methods: a review and comparative study. Structural Health Monitoring, 10, 2011

[18]   Y. M. Fu and L. Yu. A de-based algorithm for structural damage detection. Advanced Materials Research, 2014

[19]   L. Schmit and C. Fleury. Discrete-continuous variable structural synthesis using dual methods. AIAA Journal, 18, 1980

[20]   P. E. Gill, Murray W., and M. H. Wright. Practical optimization. Academic Press, 1981

[21]   DN Wilke, S Kok, AA Groenwold. The application of gradient-only optimization methods for problems discretized using non-constant methods. Structural and Multidisciplinary Optimization, 40, 2010

[22]   S Ben Turkia, DN Wilke, P Pizette, N Govender, NE Abriak. Benefits of virtual calibration for discrete element parameter estimation from bulk experiments. Granular Matter, 21, 2019

[23]   JA Snyman, DN Wilke. Practical mathematical optimization: Basic Optimization Theory and Gradient-Based Algorithms, Springer Optimization and Its Applications (SOIA, Volume 133), Springer, 2018

[24]   Y Chae, DN Wilke. Sub-dimensional surrogates to solve high-dimensional optimization problems in machine learning, Advances in Artificial Intelligence: Reviews, Volume 1, International Frequency Sensor Association Publishing, 2019

[25]   D Correia, DN Wilke. How we solve the weights in our surrogate models matters, Journal of Mechanical Design 141 (7), 074501, 2019

[26]   D Correia, DN Wilke. Purposeful cross-validation: a novel cross-validation strategy for improved surrogate optimizability, Engineering Optimization 53 (9), 1558-1573, 2021

An Investigation on Axial Force Reductions of High-strength Bolts by Induction Heating for Paint-coating Removal

Nakahara Tomonori[1], Hirohata Mikihito[2], Furuichi Toru[3]

[1] Japan Bridge Corporation, 1-9-1, Edohori, Nishi-ku, 5500002, Osaka, Japan, t-nakahara@nihon-kyoryo.co.jp

[2] Graduate School of Engineering, Osaka University, 2-1, Yamada-oka, 5650871, Suita, Japan, hirohata@civil.eng.osaka-u.ac.jp

[3] FURUICHI Co., Ltd., 1-13-4, Kishibe-kita, 5640001, Suita, Japan, t-furuichi@jcom.zaq.ne.jp

Abstract: Removal of anti-corrosion paint is key to the maintenance of aging structures. Previous investigations showed that heating high-strength bolts for coating removal reduces their axial strength. Herein, a series of experiments were conducted to investigate the effect of heating rate on axial force reduction, in search of possible methods to suppress this reduction. The high-strength bolts were heated to 200°C, at different heating rates, and the changes in axial force were estimated, by measuring the strain at the bolt shafts as the temperature increased. The mechanism of the axial force reduction could be explained by the strain behavior at the bolt shafts. The results showed that the shorter the heating time was, the more the axial force was reduced, suggesting that heating bolts over 15-30 seconds suppressed the axial force reduction to 5% of the initially installed axial force of the high-strength bolts.

Keywords: Paint-coating removal; induction heating; bolted joints; axial force

1 Introduction

The maintenance and management of bridge structures are important for their long-term use in sound condition. In the case of steel structures, corrosion is one of the main causes of damage and deterioration. Therefore, several corrosion protection methods have been established and applied to the steel structural members according to the importance of the structure, the expected service life, and the environmental conditions in which the structure is placed [1].

Paint-coating is used as a general corrosion protection method as it balances ease of manufacture, cost, and durability. Many paint-coating systems have been

proposed for steel structures in consideration of their environmental corrosion conditions and expected service life [2] [3]. However, deterioration of the paint coating is inevitable over the long-term use of steel structures regardless of the system used. The deteriorated paint coating is renewed at specified intervals to keep the soundness of the coated structures.

When renewing the paint coating, the removal of the existing coating and any rust on the structure significantly influences the performance of the newly applied coating. It has been demonstrated that the sufficient removal of deteriorated paint-coating and rust, and proper preparation of the substrate steel surface affects the durability of the renewed paint [4]. Power tools, blasting, and chemical agents are widely used in the removal of coatings and rust [5]. However, power tools and blasting generate noise and scatter dust in the air, so care is required to control these environmental impacts. Although the use of chemical agents is effective for reducing noise and dust, the amount of waste increases as both the removal agent and the removed paint coating mixed in the agent need to be disposed of. To address these problems, a new paint-coating removal method using a heating device has been developed.

In this method, the paint-coated steel structural members are heated to around 200ºC to soften the paint coating so it can be easily removed with scrapers or other hand tools. Induction heating (IH), which can quickly heat a localized part of the steel material, is used as the heat source for removing the paint-coating from steel structures [6-9]. IH is effective for removing the paint-coating on flat and wide steel members, such as the web plates or deck plates of steel girders. However, it is ineffective in removing coatings from members with complicated geometric shapes, such as connecting parts. This makes coating removal on high-strength bolted joints inefficient when using IH, as the bolts must be heated and the paint-coating removed individually. To facilitate more efficient removal, the authors previously developed an electric heating device capable of heating multiple bolts simultaneously. Although the heating device facilitated the removal of the paint-coating from bolted joints, there was a possibility that heating the bolts excessively would reduce the axial force in the bolts [10]. Possible methods to suppress this loss in bolt axial force and the mechanism for such loss have not been sufficiently elucidated.

This study aims to investigate the bolt axial force reduction mechanism when a bolt is heated for paint-coating removal. A series of heating experiments were conducted on the bolted joint specimens using an IH device. The changes in the axial forces of bolts were examined by measuring the bolt shaft strain before and after heating. Subsequently, a discussion on the reasons for the changes in the axial forces of bolts by heating was conducted based on the results from these measurements. Furthermore, based on the experimental results, suggestions were made for conditions to suppress axial force reduction in the paint-coating removal work.

2 Experiment

2.1 Pre-Heating of High-strength Bolts and Temperature-Correcting Strain Data

In this study, high-strength bolts were heated and the elongations of the bolts were measured by strain gauges attached to the bolt shafts. Previous investigations demonstrated that measured strain values obtained by the gauges included the expansion of the adhesive attaching the gauges to the specimens as temperature changed, and that pre-heating the specimens once after the application of adhesive minimized adhesive creep in subsequent strain measurements. Therefore, the bolts used in this study were pre-heated to compensate for the expansion of the adhesive with temperature affecting the strain measurement. Additionally, the relationship between strain value and temperature was obtained through a pre-heating experiment to examine the measurement accuracy of the real strain on the bolt.

Figure 1 shows the installation of heat-resistant strain gauges (applicable temperature: 350ºC) and thermocouples to the bolt shaft. F10T M22 high-strength bolts were used. Table 1 shows the mechanical properties of the bolt in the mill sheet. The opposite sides of the bolt shaft were machined. Then, two strain gauges and two thermocouples were placed symmetrically at the center of the bolt axis. The reason why the strain gauges were placed symmetrically was to eliminate the influence of bending on the bolt shaft by averaging the strain outputs on both sides of the bolt shaft. The wires were routed through the holes in the bolt head.
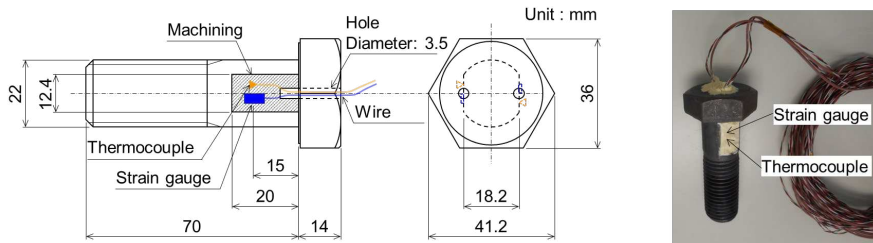

Figure 1

Installing strain gauges and thermocouples to a high-strength bolt

Table 1

Mechanical properties of the F10T M22 high-strength bolt

	Yield stress (N/mm^2)	Tensile strength (N/mm^2)	Elongation (%)	Drawing (%)	Rockwell hardness HRC
F10T M22	1033	1087	19	73	33

It has been reported that organic paint-coating materials, such as alkyd resin, deteriorate when heated over 170ºC [11] [12]. Furthermore, a previous study showed that the mechanical properties of high-strength bolts did not deteriorate when heated under 300ºC [13]. From these observations, the heating temperature for removing the paint-coating from high-strength bolts was set at 200ºC [10].

Three high-strength bolts, each attached with two strain gauges, were heated to 200ºC in an electric furnace. The strain was measured as the temperature increased. Figure 2 shows the relationship between the temperature, T, and the measured strain, $\Delta\varepsilon$. Due to the material characteristics of the polyimide resin adhesive used for attaching the strain gauges to the bolts, the measured strain varied with the temperature. The approximation curve of the relationship between the temperature, T, and the measured strain, $\Delta\varepsilon$, was fitted by Eq. (1).

$$\Delta\varepsilon = -6.74 \times 10 + 4.15 \times T - 6.44 \times 10^{-2} \times T^2$$

$$+ 2.43 \times 10^{-4} \times T^3 - 1.34 \times 10^{-7} \times T^4 \tag{1}$$
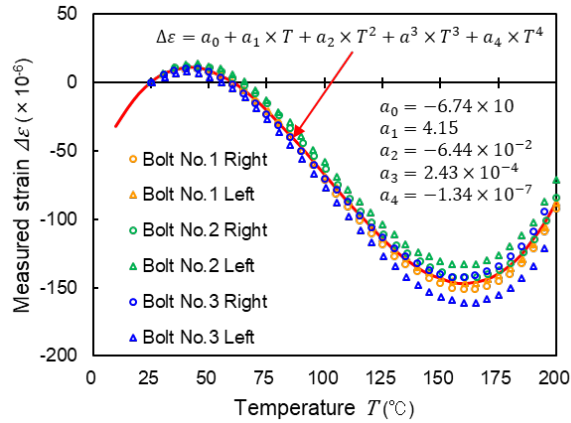
Figure 2
Relationship between the temperature and the measured strain

From the approximation curve, the strain data, ε_1, was corrected using Eq. (2) to obtain the corrected strain value.

$$\varepsilon = \varepsilon_1 - (\Delta\varepsilon_1 - \Delta\varepsilon_0) \tag{2}$$

Where ε is the corrected strain data corrected for temperature, ε_1 is the measured strain data at temperature T_1, $\Delta\varepsilon_1$ is the strain value calculated using Eq. (1) with temperature T_1, and $\Delta\varepsilon_0$ is the strain value calculated using Eq. (1) with temperature T_0, where the initial strain data was measured and set as zero.

2.2   Relationship between Bolt Axial Force and Strain

In this study, the bolt axial force was estimated from changes in bolt shaft strain. This estimation required the relationship between the bolt axial force and bolt shaft strain be obtained, and a calibration test was conducted to establish the formula for this estimation. To this end, tensile loads were applied to bolts with strain gauges. The bolts used in this test were pre-heated to 200ºC to eliminate the influence of adhesive expansion. After the temperature of the bolts cooled down to room temperature, the tensile test was conducted.

Figure 3 (a) shows how the calibration test was set up. Six high-strength bolts were used in the calibration test. Tensile loads of 40 kN, 80 kN, 120 kN, and 160 kN were gradually applied to the bolts three times. The magnitudes of the tensile loads were limited in the elastic range. Linear regression was applied to the relationship between the bolt axial force and the strain as shown in Figure 3 (b).
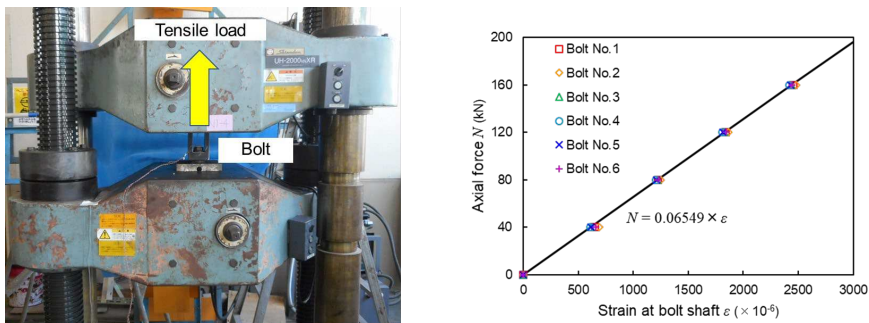
(a) Calibration test setup   (b) Relationship between axial force and strain

Figure 3

Calibration test to measure the relationship between bolt axial force and strain

Based on the regression formula shown by Eq. (3), the bolt axial force was estimated using the temperature-corrected strain described in the previous section.

$$N = 0.06549 \times \varepsilon \qquad\qquad\qquad\qquad\qquad\qquad (3)$$

Where, N is the estimated axial force (kN). ε is the strain with the temperature compensation.

2.3   Shape and Dimension of Joint Specimen

Figure 4 shows the specimen, an analogue for a high-strength bolted joint. A base plate was sandwiched by two splice plates. The material of the base plate and the splice plates was SS400. The thickness of the plates was 9 mm. Four high-strength F10T bolts were tightened to join the plates. The material properties and the chemical compositions of steel plates are shown in Table 2.

The purpose of this study is to investigate the influence of heating on the axial forces of high-strength bolts. Therefore, the specimens were not paint-coated and were merely heated under the same conditions as those for paint-coating removal. The surfaces of the plates were cleaned by blasting. The surfaces of the bolts were left covered with mill scale. Three specimens were used.
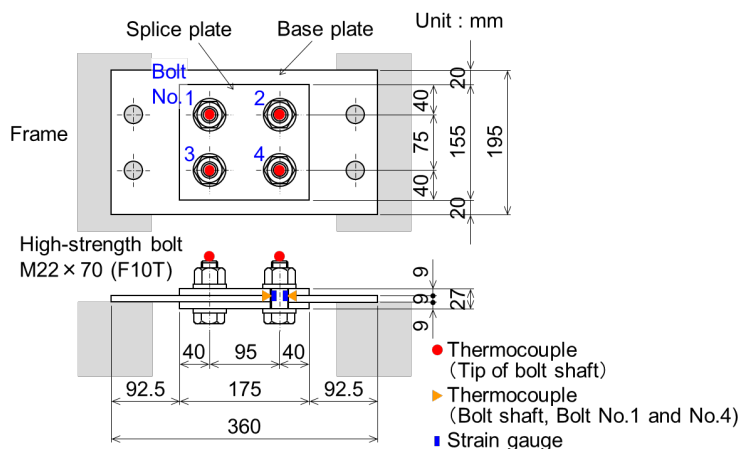

Figure 4
High-strength bolted joint specimen

Table 2
Mechanical properties and chemical composition of steel plate

	Yield stress (N/mm²)	Tensile strength (N/mm²)	Elongation (%)	Chemical compositions (mass %)				
				C	Si	Mn	P	S
SS400	334	477	27	0.16	0.14	0.74	0.024	0.006

As shown in Figure 1, strain gauges and thermocouples had been attached to six bolts for the calibration test in the previous section. Two of these bolts were installed on three specimens as bolts No. 1 and No. 4.

For bolts No. 2 and No. 3 in each specimen, strain gauges were attached to the bolt shafts. However, thermocouples were not attached to the bolt shafts due to the limited number of measuring channels of the data logger used in the heating experiment. A thermocouple was attached to the tip of each bolt shaft to measure the temperature from heating.

The high-strength bolts in the specimens were tightened to a specific axial force. The magnitude of the installed axial force was 226 kN, 10% higher than the designed axial force of 205 kN for F10T [14]. The high-strength bolts were manually tightened first, then tightened individually by an electric wrench to 60% of the target axial force. Finally, the bolts were tightened to the target axial force

by the electric wrench. After the tightening, relaxation and creep in the bolts reduced the axial forces. Therefore, the heating experiment was conducted over 2 weeks after the tightening. During this tightening process and waiting time, the strain was measured every 10 minutes.

2.4   Heating Experiment

Figure 5 shows how the heating experiment was set up. The IH device used in this study was RPR1032 [15]. The ring-type head of the device was applied to the nut side of the high-strength bolts in the specimens. The temperatures were measured by the thermocouples at the tips of the bolt shafts. The temperature required for paint-coating removal was around 200ºC. Although the target temperature was uniform across all experiments, the heating time was changed. Here, the heating times were parametrically changed while keeping the target temperature of 200ºC constant. The heating times were set to 3, 15, and 30 seconds by arranging the outputs of the IH device. The temperatures and strains of bolts No. 1 and No. 4 were measured at intervals of 0.1 seconds during the heating experiment. To complete the relaxation and creep of the bolts, the specimens were kept for over 2 weeks after the heating experiment.

The changes in the axial forces were evaluated by dividing the reduced axial forces by the initial axial forces (the axial force reduction ratio). Furthermore, the estimated axial forces were confirmed to be around zero when the bolts were completely released from the specimens after the experiment.
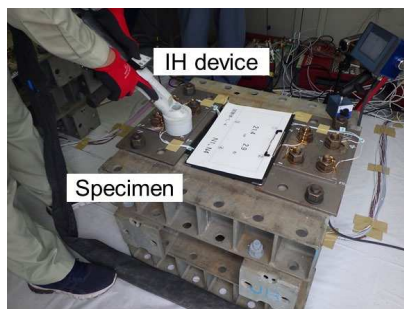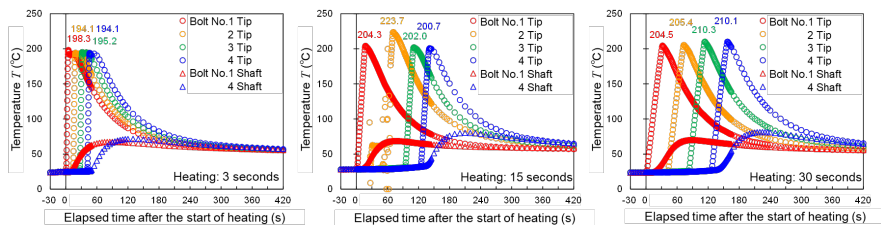

Figure 5
Heating experiment setup

3 Result and Discussion

3.1 Temperature History

Figure 6 shows the temperature histories of the bolts during the heating experiment. The maximum temperatures of the tips of the bolt shafts were observed 1 to 2 seconds after the heating routine was finished. The target temperature of 200ºC was achieved in all tested conditions. The temperatures at the middle of the bolt shafts (bolts No. 1 and No. 4) to which the strain gauges were attached reached maximum temperatures of 70 to 80ºC. The maximum temperatures at the middle of the bolt shafts were observed 40 to 60 seconds after the time when the maximum temperatures at the tips of the bolt shafts were observed.

In specimen No. 2, the temperature of bolt No. 2 changed discontinuously because the IH device was accidentally stopped shortly after the start of heating. The heating routine was briefly restarted, resulting in the maximum temperature at the tip of this bolt shaft being around 20ºC higher than those of other bolts.

It was expected that the temperature of the bolts would cool to room temperature more quickly under faster heating conditions than slower long heating conditions. However, the temperature of the bolts became uniform 300 to 400 seconds, after heating was finished, for all conditions.

(a) Heating time of 3 seconds   (b) Heating time of 15 seconds   (c) Heating time of 30 seconds

Figure 6

Temperature histories

3.2 Change in Bolt Axial Force

Figure 7 shows the changes in bolt axial forces estimated by the strain measurement. The strain measurement at the bolt shafts was started before the bolts were tightened. Measurement continued during the heating and after releasing the bolts. The bolt axial forces were estimated by Eqs. (1), (2) and (3).

Although the installed axial forces to the bolts by tightening were slightly reduced by creep and relaxation, the axial forces became uniform within approximately 3 days. The axial forces increased temporarily when the bolts were heated. However, the axial forces decreased after the heating. This phenomenon will be discussed later.

The axial forces after the heating were uniform, then the axial forces became almost zero when the bolts were released from the specimens.

In all specimens, the strains at the bolt shafts were measured at intervals of 0.1 seconds in bolts No. 1 and No. 4 during the heating. Figure 8 shows the changes in the axial forces of bolts No. 1 and No. 4 over time, focusing on the period around the heating process. The axial forces increased shortly after the start of heating and decreased when the heating was finished. The axial forces then decreased gradually during the cooling process.

A greater change in the bolt axial forces was observed when the bolts were heated to the target temperature over 3 seconds compared to when the bolts were heated over 30 seconds. An intermediate result between the two was observed when the bolts were heated over 15 seconds. The bolt axial forces increased by 16 kN, 12 kN, and 8 kN for heating times of 3 seconds, 15 seconds, and 30 seconds, respectively. The subsequent decreases in the bolt axial forces during cooling were 36 kN, 25 kN, and 21 kN for heating times of 3 seconds, 15 seconds, and 30 seconds, respectively.
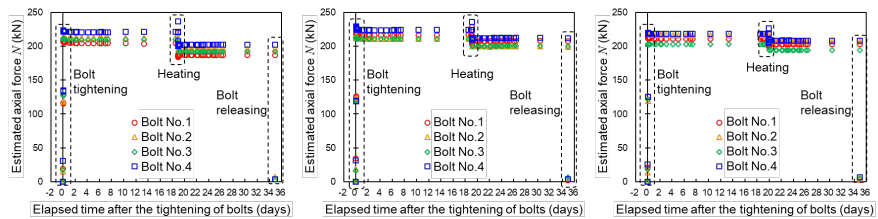
| (a) Heating time of 3 seconds | (b) Heating time of 15 seconds | (c) Heating time of 30 seconds |

Figure 7

Change in bolt axial force
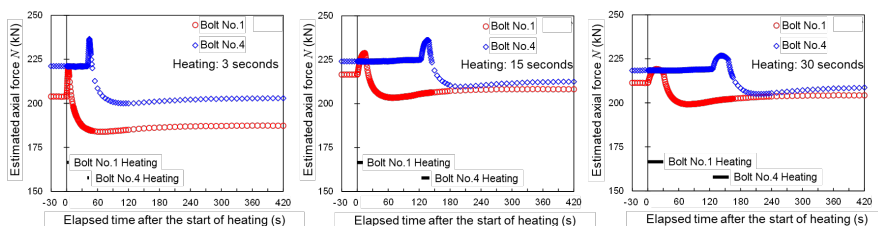
| (a) Heating time of 3 seconds | (b) Heating time of 15 seconds | (c) Heating time of 30 seconds |

Figure 8

Change in bolt axial force before and after heating

Figure 9 shows the relationship between the heating time and the reduction of the bolt axial force (also the reduction ratio of the bolt axial force). There is a clear correlation between the reduction of the bolt axial force and the heating time, and for paint-coating removal, high-strength bolts should be heated to the target temperature over a longer period of time to suppress the axial force reduction. Although the experimental conditions in this study were limited, the axial force reduction of high-strength bolts could be kept within 5% of the initial axial force when the heating time was over 15 seconds for a bolt being heated to 200ºC for the purposes of paint-coating removal.

(a) Axial force reduction

(b) Reduction ratio of axial force
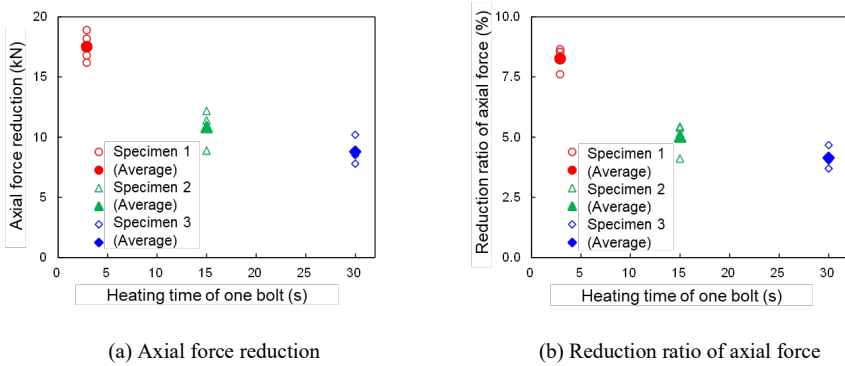
Figure 9

Relationship between heating time and axial force reduction

3.3 Mechanism of Change in Bolt Axial Force

Figure 10 shows a potential mechanism explaining the increase and decrease in bolt axial force during the heating and cooling processes.
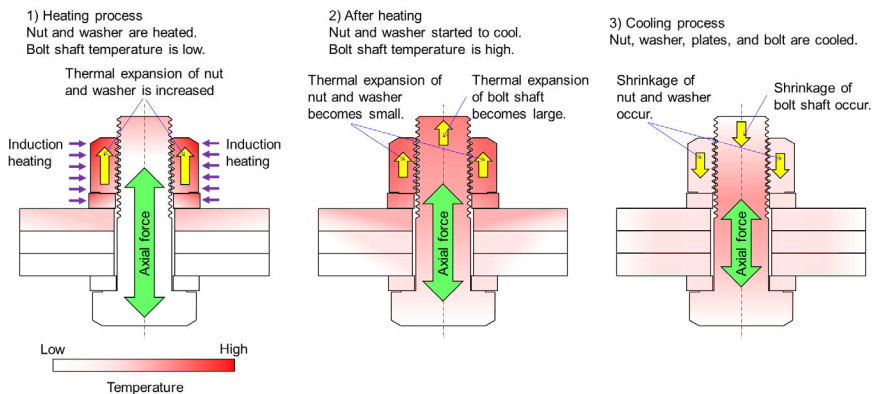

Figure 10

Mechanism of axial force reduction by heating

In this study, the nut side of the joint was heated by the IH device, resulting in a rapid increase in temperature for the nut. The heat had yet to reach the bolt shaft, so the bolt shaft was stretched by the expansion of the nut. We propose this as a possible explanation, as to why the bolt axial force increased during the heating process. After heating, the temperature of the bolt shaft increased gradually via thermal conduction from the nut, while there was no further temperature increase in the nut itself. As shown in Table 3.1 in EN 1993 1-2, the elastic modulus of carbon steel decreases by 10% at 200ºC compared to room temperature [16]. When the temperature of the bolt reached 200ºC, it might be slightly softened due to the temperature rise. A possible explanation as to why the bolt axial force decreased shortly after heating is that there was more expansion in the bolt shaft relative to the expansion of the nut as heat was no longer being applied. In the cooling process, the shrinkage of the nut and the bolt shaft occurred. In the early stage of the cooling, the shrinkage of the nut might be larger than that of the bolt shaft. Due to the difference in shrinkage between them, the bolt axial force slightly increased during the cooling process. However, the axial force might not recover to the initial state after the joint had cooled sufficiently, to the point where there was a negligible temperature difference between the nut and the bolt shaft.

Based on the experimental results, the reduction of the bolt axial force occurred shortly after heating, with maximum reduction of the bolt axial force when the temperature difference between the nut and the bolt shaft are potentially at their greatest.

A quicker heating process increased the temperature difference between these two components, therefore justifying why the axial force reduction was larger when the specimen was heated over 3 seconds compared to the case when the specimen was heated over 30 seconds.

As shown in Table D.1 in EN 1993 1-2, the strength reduction factor for bolts at 200ºC is 0.935 [16] times that at room temperature [16]. The reduction ratio of the bolt axial force obtained in this study was similar to this value for a heating time of 3 seconds as shown in Figure 9 (b). However, the reduction of bolt axial force could be suppressed by prolonging the heating time to 15 seconds or 30 seconds. This is a new finding that can be applied to paint-coating removal processes that use heating in order to preserve the axial force of bolts.

Conclusions

A series of heating experiments were conducted on high-strength bolted joint specimens using an IH device for paint-coating removal. The changes in the axial forces of bolts were examined and the reason for these changes was discussed. The main results obtained are as follows:

(1)   An experimental procedure for estimating from the strain at the bolt shaft the bolt axial force as temperature changed was examined. Bolts with strain gauges attached with a resin adhesive were pre-heated to 200ºC to

eliminate the influence of the adhesive expansion on the measurement accuracy. With the influence of adhesive expansion eliminated, the linear relationship between the bolt axial force and the strain value was established by a calibration test.

(2)   The nuts of the high-strength bolted joint specimens were heated to 200ºC with varying heating times from 3 seconds to 30 seconds using an IH device for paint-coating removal. It was observed that the longer the heating time was, the larger the reduction of the bolt axial force. The reduction ratio of the bolt axial force was defined as the ratio of the magnitude of the axial force reduction to the initial axial force. The reduction ratios of the axial force were 8.3% when heated over 3 seconds, 5.0% when heated over 15 seconds and 4.1% when heated over 30 seconds.

(3)   Based on the experimental results, the mechanism of bolt axial force reduction from heating was estimated. The temperature difference between the nut and the bolt shaft, which was enlarged by the short heating time, might decrease the axial force greatly. As the mechanism of bolt axial force reduction from heating shown in this study was merely an assumption, more investigation will be performed by numerical simulation in future work to prove the validity of this mechanism.

The mechanism of bolt axial force reduction, by heating, as shown, is an assumption based on the experimental results. To prove the validity of this mechanism, more investigations will be performed by numerical simulation in future work.

Acknowledgment

References

[1]   Kline, E. S. (2008): Steel Bridges: Corrosion Protection for 100 Years, *Journal of Protective Coatings & Linings*, 20-31

[2]   Kage, I., Matsui, K., Kawabata, F. (2005): Minimum maintenance steel plates and their application technologies for bridge – life cycle cost reduction technologies with environmental safeguards for preventing social infrastructure assets -. *JFE Technical Report*, 5, 37-44

[3]   Kreisolva, K., Geiplova, H. (2012): Evaluation of corrosion protection of steel bridges. *Procedia Engineering*, 40, 229-234

[4]   Itoh, Y., Hirohata, M., Hosoi, A., Sugiura, Y. (2013): Anticorrosive performance of repair painting as remedy for deterioration in metallised steel. *Corrosion Engineering, Science, and Technology*, 48, 537-551

[5]   Hopwood II, T., Oberst, C. M. (1993): The removal of lead-based paint from steel bridges. Research Report KTC-93-3, Commonwealth of Kentucky: Kentucky, US, 20-23

[6]   Nakamura, M., Hirohata, M., Inoue, K., Konishi, H. (2017): Applicability of Induction Heating on Paint Coating Removal of Steel Bridge Member. *Proceedings of 9ᵗʰ International Symposium on Steel Structures*, Jeju, Korea, November 1-4, Korean Society of Steel Structures, 401-403

[7]   Konishi, H., Suzuki, N., Tanaka, M., Sameshima, C., Nishitani, T., Hirohata, M. (2017): Application of induction heating for removal coating in Kyoda steel bridges. *Bridge and Foundation Engineering*, 7, 14-20 (in Japanese)

[8]   Konishi, H., Ihaya, T., Fukushima, N., Matsui, T., Hayashi, M., Hirohata, M. (2020): Field test of coating removal by induction heating in Ichikawa bridge. *Bridge and Foundation Engineering*, 6, 18-23 (in Japanese)

[9]   Hirohata, M., Nakahara, T., Jármai, K. (2021): Life cycle cost analysis on anti-corrosion coatings for steel bridges in Japan, *microCAD International Multidisciplinary Scientific Conference*, 11(5), 92-103

[10]   Nakahara, T., Hirohata, M., Kondo, S., Furuichi, T. (2021): Paint Coating Removal by Heating for High-Strength Bolted Joints in Steel Bridge and Its Influence on Bolt Axil Force, *Applied Mechanics*, 2, 728-738

[11]   Gündüz, G., Kisakürek, D., Kayadan, S. (1999): Flame retardant alkyd paint. *Polymer Degradation and Stability*, 64, 501-504

[12]   Gonçalves, G. S., Baldissera, A. F., Rodrigues Jr., L. F., Martini, E. M. A., Ferreira, C. A. (2011): Alkyd coatings containing polyanilines for corrosion protection of mild steel. *Synthetic Metals*, 161, 313-323

[13]   Kodur, V., Yahyai, M., Rezaeian, A., Eslami, M., Poormohamadi, A. (2017): Residual mechanical properties of high strength steel bolts subjected to heating-cooling cycle. *Journal of Constructional Steel Research*, 131, 122-131

[14]   Uno, N., Nagata, M., Kanisawa, H., Azuma, K. (2008): Super-high-strength bolt, ''SHTB®''. *Nippon Steel Technical Report*, 97, 95-104

[15]   RPR Technologies. Available online: https://www.rprtech.com/ (accessed on 20 March 2023)

[16]   European Standard (2005): Eurocode 3: Design of steel structures – Part 1-2: General rules – Structural fire design

Optimal Design of Wind Wheel Column

Imre Timár, Ákos Gergely Horváth

University of Pannonia, Egyetem u. 10, H-8200 Veszprém, Hungary
timar.imre@mk.uni-pannon.hu

Abstract: The paper deals with the optimal design of a wind wheel column. Have been determined the forces acting on the column. The inner diameter and wall thickness of circular tube are unknown. The minimum of mass was determined in the case of non-linear design constraints. The constraints relate to the maximal stresses and stability of column. A numerical solution to this problem is given by genetic optimization algorithm.

Keywords: wind wheel column; optimal design; weld

1   Introduction

An important structural element of wind turbines is the support column. In the following, we present the optimal design of a wind wheel column with a tubular cross-section (Figure 1). The inner diameter and wall thickness of the pipe are considered unknown. After defining the loads acting on the column, we formulate the objective function and the restrictions, and then solve the optimization problem with a genetic algorithm. We calculate the connecting fillet weld of the column based on the EUROCODE 3 standard.

2   Optimal Design of the Column

2.1   Mathematical Optimization

The optimum design procedure can be formulated mathematically as follows

$$\min f(\boldsymbol{x}), \qquad \boldsymbol{x} \in R^n;$$

$$0 \leq g_j(\boldsymbol{x}), \qquad j=1,2,...,m,$$

where $\boldsymbol{x} = [x_1,x_2,...,x_n]^T$ the vector of the unknown quantities and m is the number of constraints.

In our case we define the dimensions of cross-sections: inner diameter $x(1)$ and wall thickness $x(2)$ (Figure 1).

2.2 Genetic Algorithm

Global optimization procedures include the genetic algorithm (GA), which in certain cases can be used for optimal search more advantageously than traditional search algorithms. The structure and operating principle of the GA differ greatly from the previously applied procedures.

The basis of the method is the natural selection, which can also be observed in nature. This principle is used by the genetic algorithm to solve mathematical problems. Based on the principle, the weaker individual dies, on the other hand, the vigorous one lives on, and the latter can reproduce.

Possible solutions of the search space are called individuals. These have different importance from the point of view of the optimum search. After running the algorithm, the best solution will emerge from these individuals, but there are "elements" among them that are less, but there are also some that do not even come close to the optimal value.

Individuals can be coded in several ways, which basically determines how the algorithm works. The advantage of the bit sequence representation is that it is easy to perform operations with it and requires little storage space. Each bit in the bit sequence can take the value 0 or 1.

When describing the genetic algorithm, the term population refers to the set of individuals that make up the search space. This changes over time as the algorithm creates a new population at each iteration. Populations built up from different individuals over time are called generations.

The selection of the fitness function is one of the most important steps in the optimization with the genetic algorithm. The search time is significantly affected by the fitness function. In practice, this only means a large increase in the case of many variables. In the user interface of the program, the objective function of the problem to be optimized must be specified under the name fitness function.

The creation of the elements of the next generation is preceded by the operation of selection, which basically determines the quality and fitness value of the newly created individuals.

The members of the new population, the new individuals, are created during the genetic operations. Crossover and mutation operations are listed here. Genetic operations, like selection, are extremely important. From the point of view of the search, an important parameter is the relative ratio of mutation and crossover. Basically, the use of crossover means the use of the results of previous iterations, while the search space can be widened with the help of mutation.

Many variations of the crossover operation are known. Its operating principle is to cut the bit sequences representing the parent units at an arbitrary location and join the opposite bit sequences together.

Mutation, like recombination, belongs to genetic operations. The main purpose of its application is to avoid the narrowing of the search space, since in that case it may happen that we get only a local extreme value instead of the global one. During the operation, the algorithm slightly changes the individual. This is usually done by randomly changing a gene on the chromosome that describes the individual. The chance of a change is so small because a significant change could result in the loss of previously earned work.

2.3   Formulation of the Stress Constraints

The column is subjected to the following forces:

- the horizontal force acting on the wind wheel,

- the force resulting from the wind load and whirling acting on the column,

- and the compressive force resulting from the self-weight of the wind generator and the column.
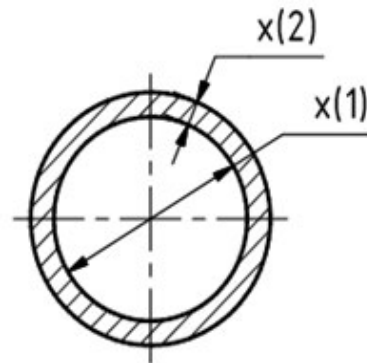
Figure 1
The self-supporting steel column [1] and its cross-section

The force acting on the wind wheel can be determined based on the following relationship [2]

$$F_k = A_k v_a \rho_a (v_1 - v_2) \qquad (1)$$

where $A_k = D_k^2 \pi / 4$ area of the wind wheel,

D_k the diameter of the wind wheel,

v_a the average velocity of the air, entering and exiting (v_1 and v_2) the wind wheel,

ϱ_a air density.

The output value of the wind speed

$$v_2 = \sqrt{1 - \eta} \; v_1 \tag{2}$$

where

η is the efficiency of the wind wheel.

The moment of the force acting on the wind wheel (F_k)

$$M_{hk} = F_k h \,, \tag{3}$$

where

h is the height of the column.

The wind pressure can be determined with the following equation [3]

$$p = q_p(z)c \,, \tag{4}$$

where

$q_p(z)$ the value of dynamic pressure,

c the shape factor, the value of which can be determined based on table 11 of the MSZ 15021 standard.

Force acting on the projection area of a cylindrical column

$$F_w = Dhp \,, \tag{5}$$

where

D is the outer diameter of the column, ($D = x(1)+2x(2)$, Figure 1).

This force is considered to be acting at half the height of the holder, thus the moment at clamping

$$M_{hw} = F_w \frac{h}{2}. \tag{6}$$

Force of the whirl burling [4]

$$F_{rez} = \frac{\pi \rho_l v_{cr}^2 c_y Dh}{2\delta} \,, \tag{7}$$

where

v_{cr} the critical wind speed can be calculated based on the literature [4],

δ is the damping factor,

c_y is the transverse form factor.

The bending moment of the F_{rez} force at the clamped end of column

$$M_{hrez} = F_{rez} \frac{h}{2}. \qquad (8)$$

The bending stress at the clamped end

$$\sigma_b = \frac{M_k + M_w + M_{rez}}{W}, \qquad (9)$$

where

W is the elastic section modulus of column.

At the lower cross-section of the column the compressive stress from the weight of the nacelle (G_g) and the weight of the column (G_o) arises

$$\sigma_N = \frac{G_g + G_o}{A_o}, \qquad (10)$$

where

A_o is the cross-sectional area of the column.

Unidirectional stresses can be added

$$\sigma_{max} = \sigma_b + \sigma_N. \qquad (11)$$

The maximum of stresses (σ_{max}) must be lower than the admissible stress (σ_{adm})

$$\sigma_{max} \leq \sigma_{adm} \qquad (12)$$

2.4   Formulation of the Stability Constraint

Elements subjected to combined bending and axial compression must satisfy the following conditions (EUROCODE 3). Since in our case it is a column with a ring cross section and the bending takes place around an axis, the stability conditions according to the standard will be as follows

$$\frac{N_{Ed}}{\dfrac{\chi_y N_{Rk}}{\gamma_{M1}}} + k_{yy}\frac{M_{y,Ed} + \Delta M_{y,Ed}}{\gamma_{LT}\dfrac{M_{y,Rk}}{\gamma_{M1}}} \le 1, \tag{13}$$

$$\frac{N_{Ed}}{\dfrac{\chi_z N_{Rk}}{\gamma_{M1}}} + k_{zy}\frac{M_{y,Ed} + \Delta M_{y,Ed}}{\gamma_{LT}\dfrac{M_{y,Rk}}{\gamma_{M1}}} \le 1, \tag{14}$$

where

$N_{Ed}=G_g+G_o$ is the design value of the compression force,

$M_{y,Ed}=M_{hk}+M_{hw}+M_{hrez}$ the maximum moment about y-y axis along the member,

$\Delta M_{y,Ed}$ is the moment due to the shift of the centroidal axis, in our case $\Delta M_{y,Ed}=0$,

$\chi_y = \chi_z$ are the reduction factors due to flexural buckling,

χ_{LT} is the reduction factor due to lateral torsional buckling, in our case

$\chi_{LT} = 1$,

k_{yy} and k_{zy} are the interaction factors, the interaction factors depend on the method, which is chosen. The interaction factors have been derived from two alternative approaches. Values these factors may be obtained from Annex A (alternative method 1) or from Annex B (alternative method 2) - EUROCODE 3,

$N_{Rk} = f_y A_o$ is the characteristic resistance to normal force of the critical cross-section,

f_y yield strength,

$M_{y,Rk}=f_y W$ characteristic value of resistance to bending moments about y-y axis.

In our case, the cross section is not sensitive to torsion, therefore the recommended value of the interaction factor

$$k_{yy} = C_{my}\left[1+(\bar{\lambda} - 0,2)\frac{N_{Ed}}{\dfrac{\chi_y N_{Rk}}{\gamma_{M1}}} \right]. \tag{15}$$

According to the standard are the values of $k_{zy} = 0.6k_{yy}$, and $C_{my} = 0.6$ from table 5.18. The non-dimensional slenderness ($\bar{\lambda}$) can be calculated as follows

$$\bar{\lambda} = \frac{\lambda}{\lambda_1}\sqrt{\beta_A}\,,$$
(16)

where

$$\lambda = \frac{\beta l}{i}\,, \quad i = \sqrt{\frac{I}{A}}\,, \quad \lambda_1 = \pi\sqrt{\frac{E}{f_y}}\,,$$
(17)

where

λ slenderness ratio,

l length of column,

βl effective column length,

i radius of gyration,

I second moment of area,

A area of cross-section,

λ_1 slenderness value to determine the relative slenderness,

E modulus of elasticity,

$\beta_A = 1$, if the cross-section is 1st, 2nd, or 3rd class.

The safety factor $\gamma_{M1}=1,1$ and $\chi_{LT}=1$.

2.5 Formulation of the Objective Function

We choose the mass of the column as the objective function (Figure 1)

$$m = h\,\rho_{ac}\,\frac{\left[(x_1 + 2x_2)^2 - x_1^2\right]\pi}{4}\,,$$
(18)

where

ϱ_{ac} steel density,

x_1 inner diameter of the pipe,

x_2 pipe wall thickness.

2.6 Solving the Optimization Problem with Genetic Algorithm

A lot of optimization problem will combine technical and economical requirements against the product or the component, so functional and economical requirements must be equally considered. When specifying the technical and economical approach, product and process optimization is defined. The product optimization can be specified further [5]

product optimization:

- topology optimization [6],

- form optimization [7],

- dimension optimization [8],

- material optimization.

Recent years the evolutionary algorithms are used frequently as optimization procedures [9]. Evolutionary algorithms are stochastic search methods, which are based on the principles of the biological evolution. Three optimization directions of the evolutionary algorithms were developed independently from each other: the evolutionary programming, the evolution strategies and the genetic algorithms. All these methods use the variation and selection operations as the basic elements of the evolution process, but they differ in the development of these elements [10]. The usage of these algorithms will increase in the coming years due to the various application possibilities. The calculation of the actual restriction values can be computed in many applications only by numeric methods.

In our case of *dimension optimization* the dimensions of cross-sections *x(1)* and *x(2)* are computed.

The following data were used for optimization:

D_k = 16 m; ϱ_a = 1,2045 kg/m³ at 20 °C; v_I = 25 m/s; η = 30 %; h = 25 m; $q_p(z)$ = 1,154 kN/m²; c = 1; v_{kr} = 8,63 m/s; c_y = 0,225; δ = 0,05; $q_p(z)$ = 1,15 kN/m²; c =1; G_g = 6000 N; steel qualities: f_y = 235; 275 and; 355 MPa; n =2; χ_{LT} = 1; β_A = 1; β = 2; E = 210 GPa; ϱ_{st} = 7800 kg/m³.

We solved the formulated optimization problem with a genetic algorithm. Table 1 shows the optimal inner diameters and wall thicknesses of the pipe column, as well as the mass minimums for different steel qualities. Figure 2 illustrates the change in column mass as a function of steel quality.

Table 1
The results of the optimization

Steel qualities	S235		S275		S355	
Wind velocity [m/s]	8	25	8	25	8	25
Inner diameter [mm]	585,6	897,2	506,8	796,8	398,7	641,1
Wall thickness [mm]	8,9	14,2	8,8	13,8	9,0	14,5

Outer diameter [mm]	603,4	**925,6**	524,4	824,4	416,7	670,1
Admissible stress [MPa]	117,5	117,5	137,5	137,5	177,5	177,5
Generated stress [MPa]	117,5	117,5	137,5	137,5	177,5	177,5
Mass [kg]	**3115,27**	**7647,84**	**2674,75**	**6611,75**	**2169,37**	**5609,55**
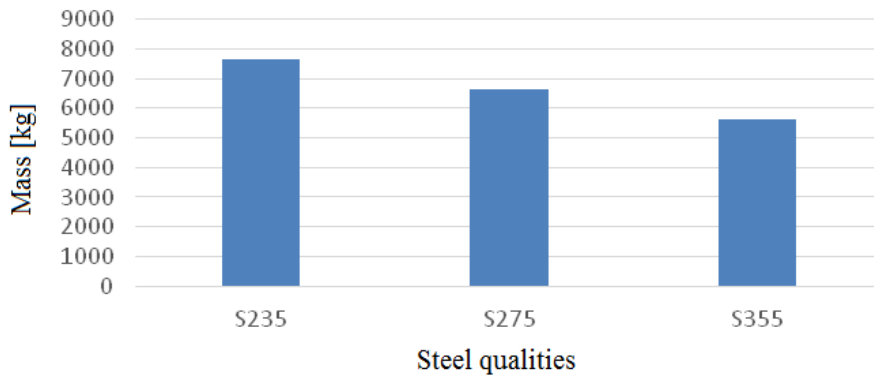
Figure 2

The change in column mass depending on the steel quality

3　Design Resistance of Fillet Welds

In this method, the forces transmitted by a unit length of weld are resolved into components parallel and transverse to the longitudinal axis of the weld and normal and transverse to the plane of its throat. The design throat area should be taken as

$$A_w = \sum a\, l_{\mathit{eff}}\,,\qquad(19)$$

where

　　a throat thickness of a fillet weld,

　　l_{eff} the effective length of a fillet weld.
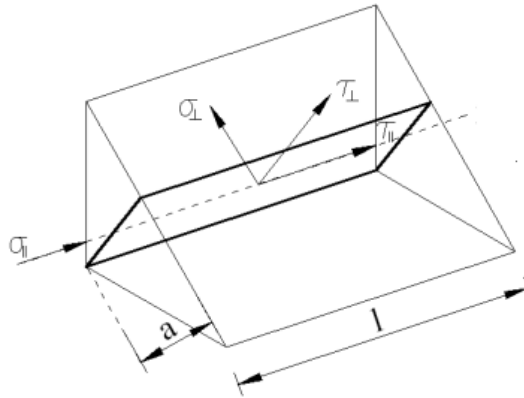
Figure 3
Stresses on the throat section of a fillet weld (EUROCODE 3)

The location of the design throat area should be assumed to be concentrated in the root. A uniform distribution of stress is assumed on the throat section of the weld, leading to the normal stresses and shear stresses shown in Figure 3, as follows:

$\sigma_\perp$ is the normal stress perpendicular to the throat,

σ_{II} is the normal stress parallel to the axis of the weld,

$\tau_\perp$ is the shear stress (in the plane of the throat) perpendicular to the axis of the weld,

τ_{II} is the shear stress (in the plane of the throat) parallel to the axis of the weld.

The normal stress σ_{II} parallel to the axis is not considered when verifying the design resistance of the weld.

The design resistance of the fillet weld will be sufficient if the following are both satisfied:

1.)

$$\sqrt{(\sigma_\perp)^2 + 3(\tau_{II}^2 + \tau_\perp^2)} \le \frac{f_u}{\beta_w \gamma_{M2}}, \tag{20}$$

2.)

$$\sigma_\perp \le \frac{f_u}{\gamma_{M2}}, \tag{21}$$

where

f_u is the nominal ultimate tensile strength of the weaker part joined,

β_w is the appropriate correlation factor,

γ_{M2} is the partial safety factor (resistance of welds).

Welds between parts with different material strength grades should be designed using the properties of the material with the lower strength grade.
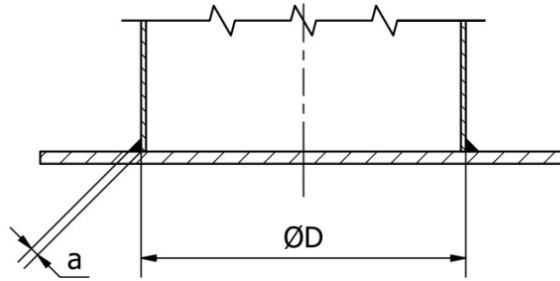
Figure 4
The fillet weld of the column

The following data were used for calculation of fillet weld:

the size of fillet weld is $a = 10$ mm; the outer diameter of column is $D_o = D + 2a = 925,6$ mm $+ 2 \cdot 10$ mm $= 945,6$ mm; $A_k = 200,96$ m².

Calculation of elastic section modulus

$$W = \frac{[(D + 2a)^4 - D^4]\pi}{32(D + 2a)} = \frac{[(945,6\text{mm})^4 - (925,6\text{mm})^4]\pi}{32(945,6\text{mm})} = 6,7995 \cdot 10^6 \text{mm}^3$$

The force acting on the wind wheel is according to equation (1) $F_k = 22,66$ kN.

The moment of this force according to equation (3) is $M_k = 551,5$ kNm. Force acting on the projection area of a cylindrical column according to equation (5) is $F_w = 26,7$ kN. The moment of this force according to equation (6) is $M_w = 333,79$ kNm. The force of the whirl burling according to equation (7) is $F_{rez} = 14,67$ kN. The moment of this force according to equation (8) is $M_{rez} = 183,38$ kNm.

Stresses due to bending can be determined according to equation (9)

$$\sigma_b = \frac{5,5150 \cdot 10^8 \text{Nmm} + 3,3379 \cdot 10^8 \text{Nmm} + 1,8932 \cdot 10^8 \text{Nmm}}{6,7995 \cdot 10^6 \text{mm}^3} = 157,2 \text{ MPa}.$$

In the fillet weld the stress components can be determined as follows

$$\sigma_\perp = \tau_\perp = \sigma \cos 45° = 157,2 \frac{\text{N}}{\text{mm}^2} \cos 45° = 111,2 \text{ MPa},$$

and

$$\tau_{II} = 0 \, .$$

Substituting the values in equations (20) and (21) gives that

$$\sqrt{(111{,}2 \text{ MPa})^2 + 3(111{,}2 \text{ MPa})^2} \leq \frac{360 \text{ MPa}}{0{,}8 \cdot 1{,}25} \, ,$$

222,4 MPa < 360 MPa, the first condition is met.

$$111{,}2 \text{ MPa} \leq \frac{360 \text{ MPa}}{1{,}25}$$

, the second condition is met.

Conclusions

We developed the optimal design of the support column of a 20 kW wind wheel with a tubular section, taking into account the requirements of the EUROCODE 3 steel structure standard. We chose the mass of the construction as the objective function. In the restrictions, in addition to the stresses from pressure and bending, we also took into account the interaction of the two stresses. In the case of different steel qualities, we determined the minimum mass of the column, as well as its optimal inner diameter and wall thickness. The fillet weld of the column was adjusted according to the EUROCODE 3 standard.

References

[1]   www.stahlbaustudium.de/druck9.pdf *(2018.08.09)*

[2]   Cs. Hetyei, Cs: The energetic situation of wind wheel. Military engineer. 12(2017) No. 3, pp.: 265-278

[3]   Dynamic design of load-bearing structural elements of buildings. Hungarian Standard. MSZ 15021/1-86

[4]   Tóth, L, .Horváth,G: Alternative energy. Wind motors, wind generators: Expertise Publishing House, Budapest, 2003

[5]   Bendsoe, M. P.: Optimization of structural topology, shape, and material. Springer. Berlin, 1995

[6]   Merke, R., Sauter, J., Gülzer, Ph.: Topology optimization with TOSCA and ABAQUS for linear guide. Konstruktion. No. 9, pp. 52-54 (2001) (In German)

[7]   Klein, M: Form optimization with higher-order finite element methods FEM of continuum structures. VDI Verlag. Düsseldorf, 2000 (In German)

[8]   Timar, I., Horvath, P., Borbely, T.: Optimization of sandwich beams with shaped section. Stahlbau, 72 (2003) No. 2, pp. 109-113 (In German)

[9]   Geike, T., Parchem, R.: Genetic algorithms for optimization of bolted joints. Konstruktion, No. 1/2, pp. 48-52, 2003 (In German)

[10]   Pohlheim, H.: Evolutionary Algorithms, Berlin, Springer, 1999 (In German)

Comparison of Different Water Tank Leg Cross Sections, when exposed to a Fire

Máté Petrik, Károly Jármai

Institute of Energy Engineering and Chemical Machinery, University of Miskolc, H-3515 Miskolc, Hungary
mate.petrik@uni-miskolc.hu; karoly.jarmai@uni-miskolc.hu

Abstract: The target of the investigation is a water tank with an internal volume of 1.5 m³. This pressure vessel is supported by legs. This study compares four different cross sections of the support, when exposed to fire. Different steel grades were used for the comparison. During the fire, the temperature rises continuously, and with it, the yield strength of the steel decreases. The purpose of the calculation is to determine how long the structure can withstand buckling.

Keywords: pressure vessel support; fire load; buckling

1 Introduction

Relatively small water tanks are widely used in industry and households and usually supported by legs. These leg supports are very simple steel structures. They are usually a circular hollow section (CHS), rectangular hollow section (RHS) or I-section. Under normal operating conditions, the load on the leg support is due to the mass of the vessel and the liquid, which causes a compressive force. This means that the leg must be checked for buckling. The load on the bottom of the vessel in the support environment, which superposes the membrane stress state on the shell of the vessel, should be checked according to the EN 13445-3 standard.

In the case of fire exposure, two main features affect the temperature increase: The shape and the material of the leg support. The material properties (yield stress, Young modulus) required for the calculations decrease with increasing temperatures. In this present paper, different types of steel, structural and pressure steels have been investigated [1]. The other main parameter is the shape of the support, more specifically the ratio of the perimeter to the cross-sectional area.

Many researchers are involved in the investigation of the fire load of steel structures. Silva *et al.* [2] investigated an I-section using finite element method

(FEM) and compared the results for different fire loads (four-sided fire, three-sided fire). Xing *et al.* [3] investigated the local buckling mechanism of plates. Analytical and numerical calculations are established. Laím *et al.* [4] and Yang *et al.* [5] performed experiments on compressed columns. They both investigated cold-formed I-sections and demonstrated the typical failure mechanism with buckling modes during compression load.

2 Mechanical and Thermal Properties of the Steel Grades

2.1 Mechanical Properties

The two important mechanical properties in the heat transfer process are the yield strength and Young's modulus of the steel. These values are highly dependent on temperature, as shown in Figure 1.
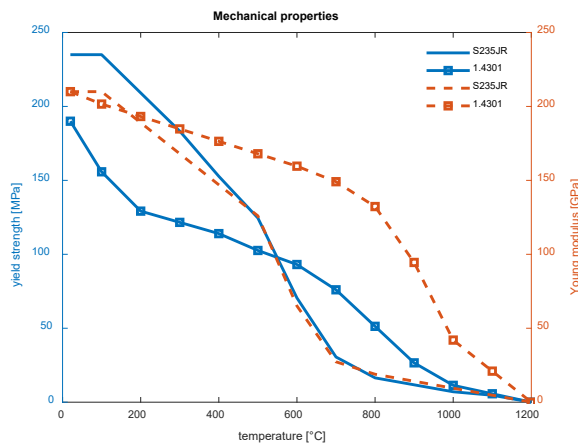
Figure 1

Temperature dependence of steel grades [6]

2.2 Thermal Properties

On the other hand, in this case not only the mechanical properties but also thermal properties, specific heat, density and thermal conductivity are important. These properties have a great influence on the heat transfer process; their values affect the rate of heating. In the solid state, temperature has no effect on density; its

value is constant at 7850 kg/m^3. However, specific heat and thermal conductivity highly dependent on temperature and microstructure [6]. The following graphs show the values of these two properties.
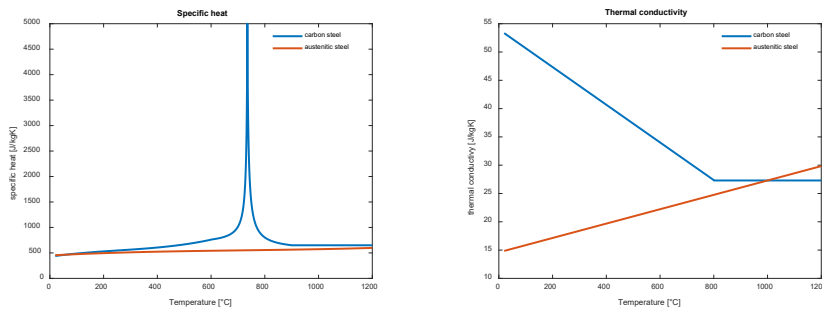
Figure 2
Temperature dependence of the thermal properties [6]

The specific heat graph shows that in the case of carbon steel, a phase transformation occurs in the steel structure and value of specific heat increases significantly near this temperature. This phenomenon slows down the heating of the legs. In the case of austenitic steel, there is no phase change and the value rises slightly as a function of temperature. The thermal conductivity also shows an interesting behavior. At room temperature, the thermal conductivity of carbon steel is more than 3,5 times higher than that of austenitic steel. However, as the temperature rises, the value of the carbon steel decreases, while that of austenitic will increases. Above 1000°C, the value of austenitic steel is higher. Both thermal properties have a strong influence on the temperature rise of the legs.

The value of the linear thermal expansion is an important material property for strength. In this case, the two grades of steel behave similarly, increasing in value with increasing temperature. Carbon steel has a value of 0.24 1/K and austenitic steel 0.33 1/K at room temperature. In this present study, this variation was not considered, since no additional collateral load from inhibited thermal expansion was assumed.

3　Thermal Calculation Method

The lumped heat capacity method was used to determine the duration of the load limit state (the value of time when the buckling occurs). In fire loading, heat from the fire is transferred to the structural material by convection and radiation. If the supports are facing the fire load and the vessel is also facing, the question may arise whether the bottom of the vessel should be checked. The high heat capacity

of the filled water causes the shell temperature to rise very slowly. The water cools the steel, so the present paper only deals with the buckling mechanism of the supports involved.

3.1   Convection and Radiation

In the case of fire loads, heat transfer is by convection and radiation. Since the velocity is negligible, an empirical Nu number correlation must be used to determine the convective heat transfer coefficient (α_c). However, the calculation is cumbersome and its value is almost neglectable when compared to the radiative heat transfer coefficient; this value is 20 W/m^{2}K according to the literature [7].

For the determination of the radiative heat transfer coefficient, which is much more decisive in this process, the modified form of Stefan-Boltzmann law is used, which is

$$\alpha_R(t) = \frac{\varepsilon_f \cdot \varepsilon_s}{\varepsilon_f + \varepsilon_s - \varepsilon_s \cdot \varepsilon_f} \cdot \sigma \left[T_f^2(t) + T_s^2(t) \right] \left[T_f(t) + T_s(t) \right], \tag{1}$$

where the different tags have the following meanings:

- ε_f is the emissivity of the fire [-], assuming 0.8

- ε_s is the emissivity of the surface of the support [-], assuming 1.0

- σ is the Stefan-Boltzmann constant ($5{,}67 \cdot 10^{-8}$ W/(m^{2}K^4))

- T_f is the temperature of the fire [K]

- T_s is the temperature of the leg support [K]

Eq. 1 shows that temperatures vary over time, but not in the same way. The fire temperature was determined using empirical correlation described in ISO 834 standard.

$$T_f(t) = 345 \cdot \log_{10}(8t + 1) + 20°C \tag{2}$$

In Eq. 2 the t time is given in minutes, and T temperature is given in °C. Based on these facts, the total heat flux from fire to legs is

$$\dot{q}(t) = \dot{q}_c(t) + \dot{q}_r(t) = \left[\alpha_c(t) + \alpha_r(t) \right] \cdot \left[T_f(t) - T_s(t) \right] \tag{3}$$

Each term in Eq. 3 depends on the time parameter. At lower temperatures the convective heat transfer method dominates, while at higher temperatures radiation can take orders of magnitude higher values.

3.2   Lumped Heat Capacity Method

Calculating the transient heat transfer can be difficult, especially for complex geometries. However, in the case of leg support, the cross-sectional area does not vary along its axis, so the complex method can be used. The simplification is based on comparing convection and radiation heat flux from fire to support and conduction through the wall. For this purpose, the heat transfer system is constructed in a similar way to an electrical network. There is a potential difference between the temperatures (analogous to the electrical voltage or potential), which indicates the heat flux from the higher temperature to the lower temperature (equivalent to electrical current). The proportional factor is the value of the resistance. The procedure described in the calculation is applicable when the Bi number, which is the ratio of the resistances, is less than 0.1 [7].

$$\text{Bi} = \frac{R_{cond}}{R_{conv}} = \frac{s_{wall}/\lambda_{wall}}{1/(\alpha_c + \alpha_r)} \tag{4}$$

In case when some sections are investigated, Eq. 4 changes to the following shape:

$$\text{Bi} = \frac{(\alpha_c + \alpha_r) \cdot \dfrac{V}{A}}{\lambda_{wall}} \tag{5}$$

In Eq. 5, the *V/A* value is a section factor, which is the ratio of the cross-sectional area to the surface perimeter exposed to the fire.
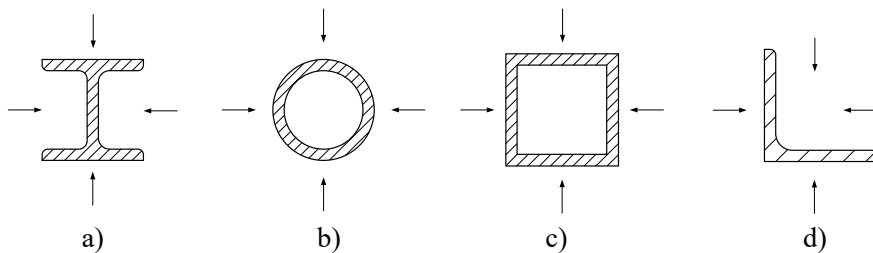
Figure 3

The investigated sections

a) I-beam, b) circular hollow section, c) square hollow section, d) hot rolled equal leg angles

Figure 3 shows the sections under consideration. All of them are standardized: DIN 1025 for I-beams, EN 10219-2 for circular and square hollow sections and EN 10056-1 for equal leg angles.

This Bi number must be less than 0.1. For a higher value, the outlined model cannot be applied. If the conditions are fulfilled, the average temperature increment of the investigated section can be calculated as follows:

$$\Delta T_s = \frac{\frac{A}{V}}{\rho_s \cdot c_{ps}} \cdot \dot{q} \cdot \Delta t,$$

(6)

where ρ_s is the density of steel [kg/m^3], c_s is the specific heat of steel [J/(kgK)], A/V is the section factor [1/m], $\dot{q}$ is the heat flux (calculated from Eq. 3), and Δt is the time step [s].

4   Thermal Calculation Method

When a compressive load is applied to a long and thin (or slender) rod, there is always a risk of buckling. The theory was developed initially by Euler (1778) to deal with this phenomenon and was extended by Tetmayer. The result of their research was the buckling curve shown in Figure 4.
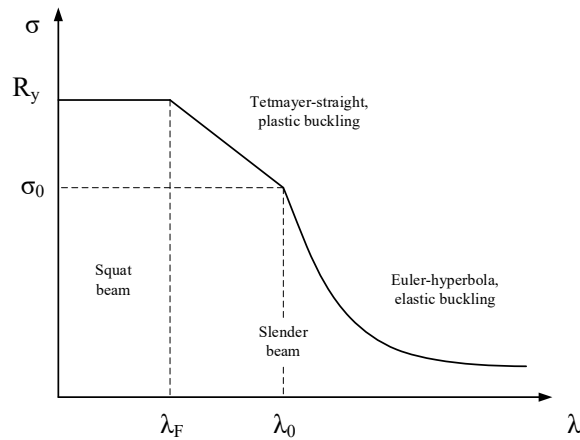
Figure 4
The buckling curve

The λ is the slenderness ratio and can be calculated in the equation below, describing the ratio between the length of the beam and the radius of gyration:

$$\lambda = \frac{K \cdot L}{r},$$

(7)

where K is the effective length factor, describing the effect of the supports on buckling (L_0 often symbolized by the $K \cdot L$ product and represents the length of the beam after the buckling), σ_0 is the elastic limit stress, R_y is the yield strength of the steel. The radius of gyration is

$$r = \sqrt{\frac{I}{A}} \tag{8}$$

where I is the second moment of inertia of the cross-section, calculated according to the axis of the buckling, and A is the area of the cross-section.
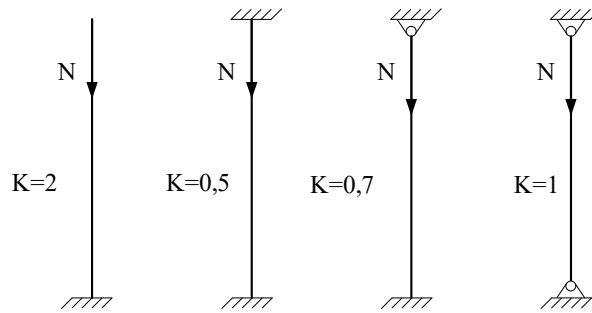
The value of K can be seen in Figure 5.

Figure 5
Buckling cases

The purpose of the calculation is to determine the value of σ_{limit} and compare it with the stress from the compressive load. The classical theory distinguishes two cases of plastic buckling, where the λ, in this case, is between λ_0 and λ_F:

$$\sigma_{\lim} = a - b \cdot \lambda \tag{9}$$

where a and b are material constants. If the λ is above λ_0, then the buckling is elastic, then the stress limit is

$$\sigma_{\lim} = \left(\frac{\pi}{\lambda}\right)^2 \cdot E \tag{10}$$

where E is the Young's modulus of steel. The last possibility is when λ is below λ_F. In this case, the beam is stubby, there is no chance of buckling, and the limit stress is equal to the yield strength of the steel.

The classical theory assumes that the beam is perfectly straight, the cross-section is free from deformation, and the residual stress is 0. Nowadays, the buckling calculations are performed according to different standards, for example, Eurocode-3, JRA, API, AISC etc. In this study, calculations have been carried out according to Eurocode-3 part 1-1 (EN 1993.1.1-2005). This standard considers the effect on initial inaccuracy, the theory developed by Ayrton and Perry (1886), and the effect of the residual stresses from the welding, the theory developed by Beer and Schulz (1970). These were the first and the second additions to Euler's classical theory. The third and last addition was carried out by Maquoi and Rondal (1978), which resulted in a complex parameter describing the effect of initial curvature and residual stresses [8].

EC-3 classifies cross-sections into four classes; the curves are shown in Figure 6:
  a) Welded I-beams, where $f_y>420$ MPa, and the flange plate thickness is less than 40 mm (Curve a_0)
  b) Hot-formed hollow sections (Curve *a*)
  c) Cold-formed hollow sections, welded box beams, and welded I-beams for buckling around the x-axis, if the flange plate thickness is less than 40 mm (Curve *b*)
  d) Welded I-beams for buckling around the y-axis (this is the axis which is parallel to the web plate) when the flange plate thickness is less than 40 mm, and I-beams for buckling around the x-axis when the flange plate thickness is above 40 mm, moreover U, L and T beams and solid bars (Curve *c*)
  e) Welded I-beams for buckling around the y-axis when the flange plate thickness is above 40 mm (Curve *d*)
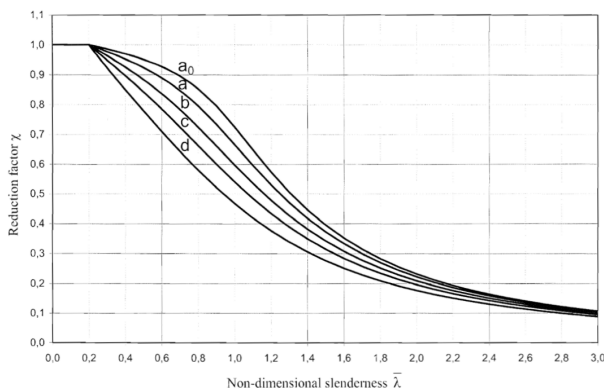
Figure 6
The reduction factor as a function of the slenderness ratio

The imperfection factor α is also given in Eurocode 3, and its value is shown in Table 1.

Table 1
The value of the imperfection factor

Buckling curve	a_0	*a*	*b*	*c*	*d*
Imperfection factor	0.13	0.21	0.34	0.49	0.76

For the leg supports, the Curve *c* applies, so the imperfection factor for the calculations is 0.49. Although the EN 1993-1-1 standard recommends Curve *b* for angle steels, this study used Curve *c* as a uniform curve due to the comparability of the significantly different geometries.

The following quantities should be introduced for the calculations:

$$\lambda_E = \pi \cdot \sqrt{\frac{E}{f_y}} \tag{11}$$

$$\bar{\lambda} = \frac{\lambda}{\lambda_E} \tag{12}$$

According to the standard, the next step is to calculate the factor Φ

$$\varphi = \frac{1}{2} \cdot \left[1 + \alpha \cdot \left(\bar{\lambda} - 0.2 \right) + \bar{\lambda}^2 \right]. \tag{13}$$

The buckling factor:

$$\chi = \frac{1}{\varphi + \sqrt{\varphi^2 - \bar{\lambda}^2}} \tag{14}$$

The inequality of the verification process:

$$\sigma = \frac{F}{A} \leq \chi \cdot f_y \tag{15}$$

The maximal value of χ is always 1, and if it is below 0.2, as χ=1, then the beam is squat, and there is no real possibility of buckling. The equations are valid for cross-section classes 1,2 and 3 but not for class 4. These classes are:

Class 1: Those cross-sections which can form the plastic joint with the rotational capacity required by the plastic analysis without loss of the resistance.

Class 2: Those cross-sections which are capable of forming their plastic moment capacity but have limited rotational capacity due to local buckling.

Class 3: Cross-sections in which, assuming an elastic stress distribution, the stress in the extreme compressive strength of the steel structure can reach the yield strength, but local buckling may prevent the development of plastic moment resistance.

Class 4: Cross-sections in which buckling occurs in one or more parts of the cross-section before reaching the yield point.

For cross-section Class 4, the effective area is used instead of A in equation (6). The calculation method is described in EN 1993.1.5 2006. The calculations are performed under the assumption that the stress can reach the yield point without local buckling.

4.2 Buckling during the Fire Load

In the calculations, the yield strength and Young's modulus must be calculated at a given temperature due to the fire load. Eurocode 3 does not give an exact value for the yield strength at a given temperature; instead, it uses a factor k multiplied

by the yield strength, which is given at 20 °C. The values of the factor are shown in Table 2 and are given in EN 1993.1.2.

Table 2

Values of the modification factors

Steel Temperature	The reduction factor for the yield strength of 1.4401 steel	The reduction factor of Young's modulus of 1.4401 steel	The reduction factor of the yield strength of carbon steel	The reduction factor of Young's modulus for carbon steel
20°C	1	0.05	1	1
100°C	0.88	0.049	1	1
200°C	0.76	0.047	0.807	0.9
300°C	0.71	0.045	0.613	0.8
400°C	0.66	0.03	0.42	0.7
500°C	0.63	0.025	0.36	0.6
600°C	0.61	0.02	0.18	0.31
700°C	0.51	0.02	0.075	0.13
800°C	0.4	0.02	0.05	0.09
900°C	0.19	0.02	0.0375	0.0675
1000°C	0.1	0.02	0.025	0.045

A linear interpolation between the values of the factors at a given temperature is used. The interpolation equation is as follows:

$$k_y = \frac{T - T_1}{T_2 - T_1} \cdot \left(k_{y2} - k_{y1}\right) + k_{y1} \tag{16}$$

In the equation, T is the temperature at which the calculation is made, and it is between T_1 and T_2. At these temperatures the yield strength and Young's modulus are given; these values are represented by k_{y1} and k_{y2}.

The buckling calculations with the reduction factor at the elevated temperature are as follows. The $\bar{\lambda}$ slenderness ratio at a given temperature is

$$\bar{\lambda}_T = \bar{\lambda} \cdot \sqrt{\frac{k_y}{k_E}} \tag{17}$$

where the $\bar{\lambda}$ is the slenderness ratio given by Eq. 10, k_y is the yield strength reduction factor, and the k_E is the reduction factor of the elastic modulus.

The α modification ratio (this is similar to the ε factor in case of buckling):

$$\alpha = 0.65 \cdot \sqrt{\frac{235\text{MPa}}{f_y}} \tag{18}$$

The reduced value of the factor φ:

$$\varphi_T = \frac{1}{2} \cdot \left(1 + \alpha \cdot \bar{\lambda}_T + \bar{\lambda}_T^2\right). \tag{19}$$

The modified reduction factor:

$$\chi_T = \frac{1}{\varphi_T + \sqrt{\varphi_T^2 - \bar{\lambda}_T^2}} \tag{20}$$

At elevated temperatures, the limit for buckling is as follows:

$$\sigma_T = \chi_T \cdot f_{y.} \cdot k_{y,\Theta} \tag{21}$$

This factor reduces the allowable stress on the support. This value is a function of the temperature, which is a function of time, just as the yield strength of steels is a function of temperature and time. The relationship between time and temperature is given by Eq. 2. When the two curves (yield strength-time and limit stress-time) cross, this point is the point of collapse due to the buckling.

5   Cases Studied and the Results

This section contains the results of the investigations. The lumped heat transfer analysis was set to the following functions:

- Material properties of the leg (which can be S235JR carbon steel grade or austenitic 1.4301 steel grade)
- Cross-section of the leg (shown in Figure 2)
- Geometric dimensions of the sections (diameter, height, width, wall thickness)

The length of the legs was the same, 1000 mm, and the diameter of the plate pads was also constant, at 140 mm. This present study compares the effect of the cross-section of the legs under fire load for a standard water vessel so that all other parts of the vessel are identical to not affect the results.

5.1   The Investigated Vessel
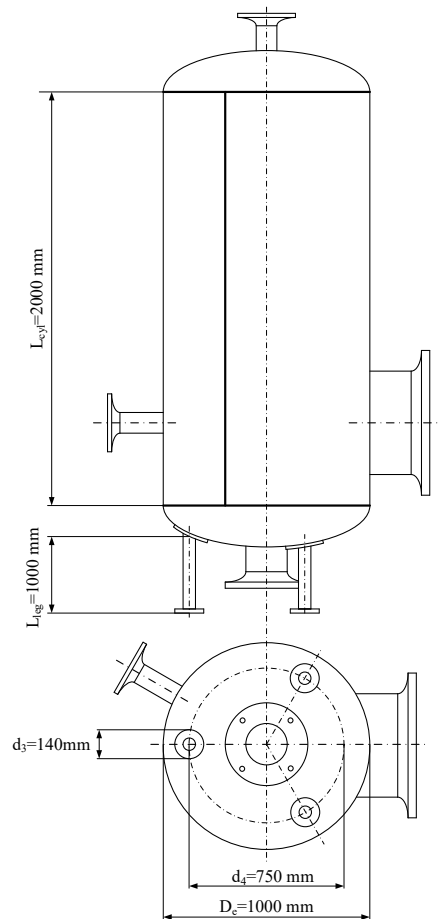
Figure 7
Schematic drawing of the investigated vessel

Figure 7 shows the geometric dimensions of the investigated water vessel. The vessel is made of P235GH steel grade, which is constant throughout the cases (and has no effect on the buckling of the legs). The external diameter is 1000 mm, the height is 2000 mm, the ends are thorispherical and are related to DIN 28011 standard, and the nominal wall thickness is 8 mm. With these data, the weight of the vessel is 550 kg, the volume of the vessel is 1.57 m^3, and the weight of the water is 1570 kg. While three legs were investigated, the force in one leg was 6935 N. This load was also constant for all leg cross-sections.

5.2   Results

5.2.1   Circular Hollow Sections

DN40 tube (Ø48.3x2.6 mm)
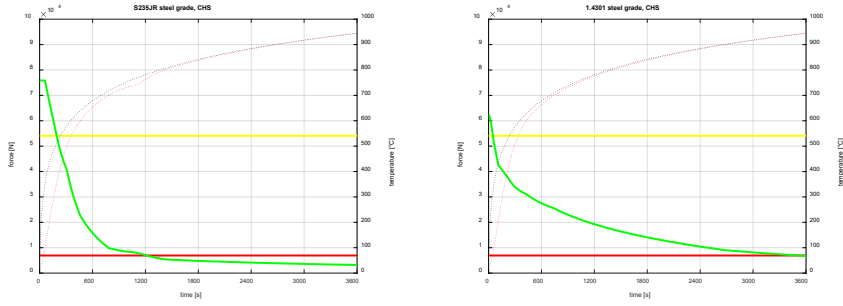
Figure 8
Force-time diagrams for DN40 tubes

DN50 tube (Ø60.3x2.9 mm)
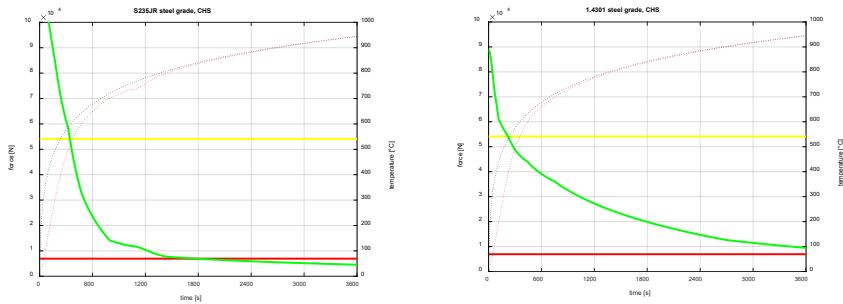
Figure 9
Force-time diagrams for DN50 tubes

DN65 tube (Ø76.1x2.9 mm)
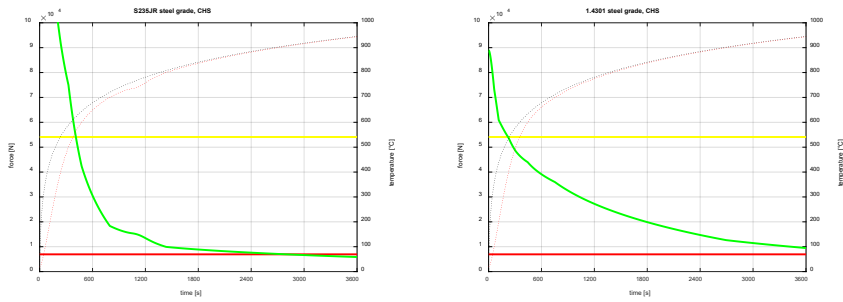
Figure 10
Force-time diagrams for DN65 tubes

5.2.2   Square Hollow Sections

40x2.5 mm
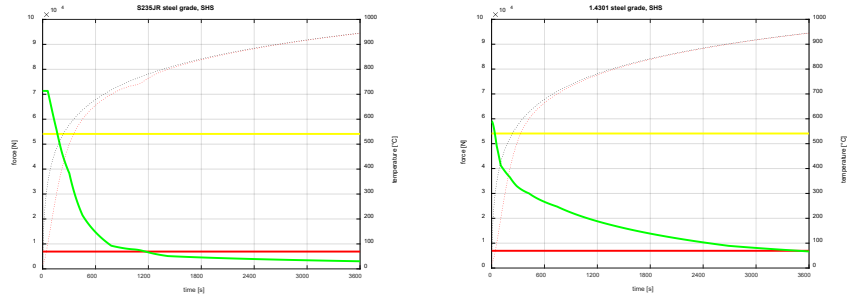
Figure 11
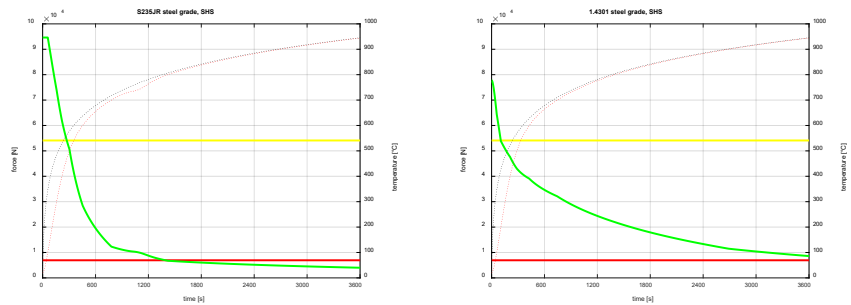Force-time diagrams for 40x2.5 square hollow sections

50x2.5 mm

Figure 12
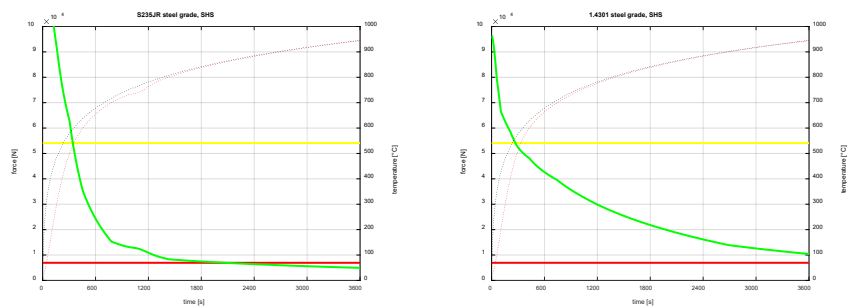Force-time diagrams for 50x2.5 square hollow sections

60x2.5 mm

Figure 13
Force-time diagrams for 60x2.5 square hollow sections

5.2.3   Square Hollow Sections

I80 section
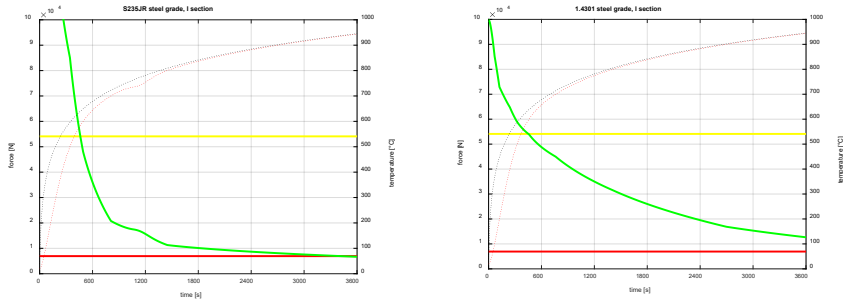
Figure 14
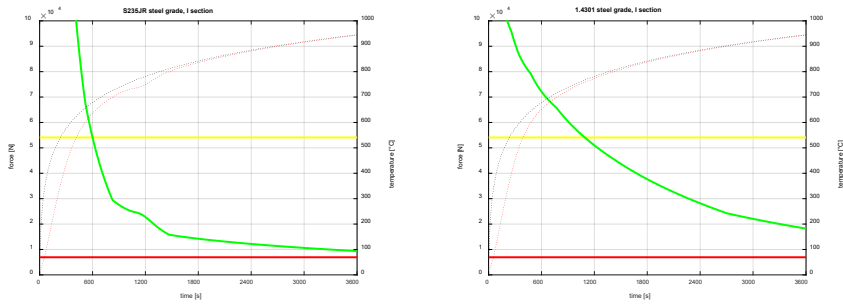Force-time diagrams for I80 sections

I100 section

Figure 15
Force-time diagrams for I100 sections

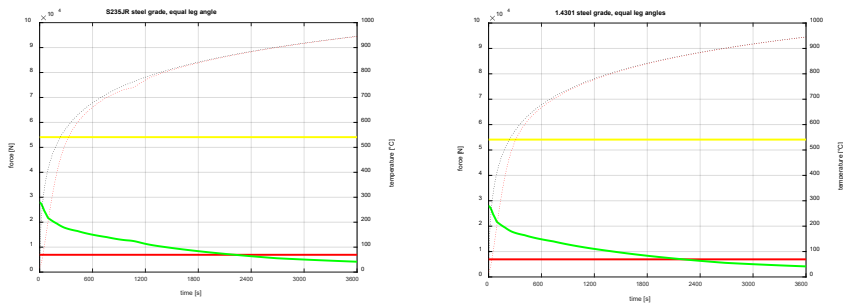### 5.2.4   Equal Leg Angles

35x4 mm

Figure 16
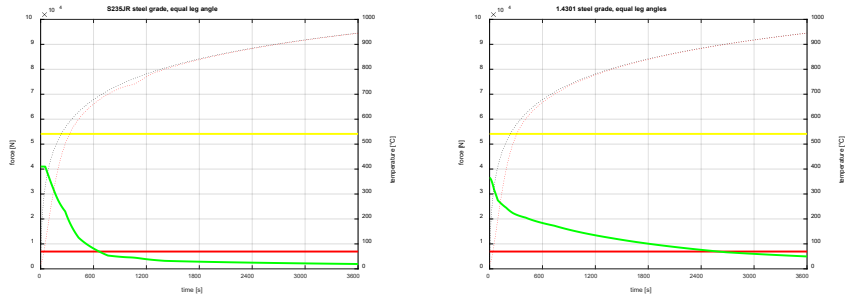Force-time diagrams for 35x4 mm equal leg angles

40x4 mm

Figure 17
Force-time diagrams for 40x4 mm equal leg angles
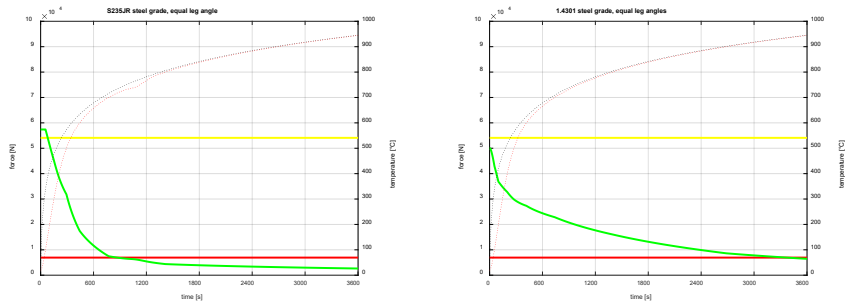
45x4.5 mm

Figure 18
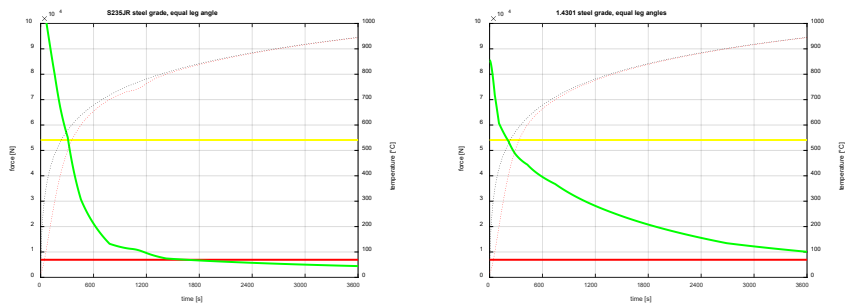Force-time diagrams for 45x4.5 mm equal leg angles

60x5 mm

Figure 19
Force-time diagrams for 60x5 mm equal leg angles

From Figure 8 to Figure 19, the red lines are the forces in the legs, the yellow lines are the forces in the shell, and the green lines are the buckling limits. These belong to the left axis. The black dashed lines are the fire temperatures, the red dashed

lines are the temperature of the legs, and these belong to the right axis. It is clear from the figures that austenitic steels are preferable in all cases, but the use of this grade of steel is not recommended. This depends on the steel grade of the vessel. If the vessel is made of carbon steel, the reinforcing plate and the leg should also be made of carbon steel. In the case of austenitic vessels, both should also be austenitic. The explanation is the difficulty welding the two types of steel grade. Making a mixed carbon-austenitic weld is also difficult, and this weld will likely be the weak point of the device.

Furthermore, hollow sections are more favorable than open sections. This is because hollow sections have the smallest section factor, so that the temperature dependence will be the slowest in these hollow sections. The section factors will be much higher for I-sections or equal-leg sections. These will reach the buckling limit fastest. From Figures 14 and 15, I-sections seem to be the solution but note that they have a much larger cross-sectional area, as we used standard sections, of which these were the smallest. The following, Figure 20, simply compares these sections according to their degree of heating [9].
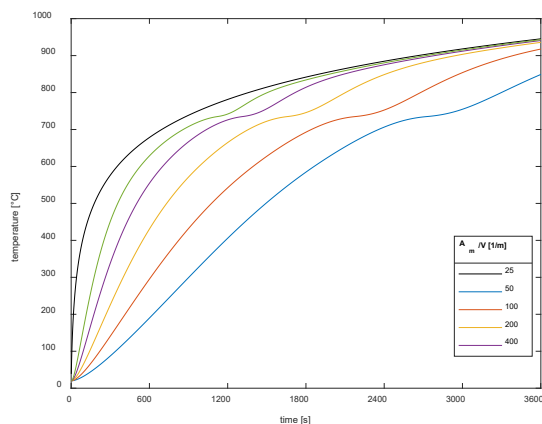

Figure 20

Comparison of section factors

5.2.5   Buckling Time

Figures 8-19 show the load on the legs, the buckling limit of the leg and the temperate of the fire and the leg support. At this point, the temperature of the vessel and the water in it were not calculated because the relatively high value of the specific heat of the water would cool the shell temperature. This 1-hour period is not long enough to cause considerable problems inside the vessel (high temperature, high value, phase change or BLEVE, which is the abbreviation for boiling liquid expanding vapor explosion). The following table shows the time interval at which the buckling occurred and the cross-section areas associated with them.

Table 3
Comparison of the buckling times

	S235JR	*1.4301*	*cross-section area*
CHS			
DN40	1214 s	3509 s	3.73 cm^2
DN50	1775 s	3600+ s	5.23 cm^2
DN65	2802 s	3600+ s	6.67 cm^2
SHS			
40x2.5	1166 s	3482 s	3.75 cm^2
50x2.5	1394 s	3600+ s	4.75 cm^2
60x2.5	2074 s	3600+ s	5.75 cm^2
I section			
I80	2291 s	3600+ s	7.57 cm^2
I100	3600+ s	3600+ s	10.6 cm^2
equal leg angle			
35x4	547 s	2207 s	2.67 cm^2
40x4	664 s	2596 s	3.08 cm^2
45x4.5	868 s	3371 s	3.9 cm^2
60x5	1655 s	3600+ s	5.82 cm^2

It is clear from Table 3 that austenitic steel is in all cases more favorable than carbon steel, even if the yield strength at room temperature is lower. In practice, CHS sections are the most commonly used, since the vessels are connected with pipelines and the leg support could be made from the remains of these pipes. I-section should be used for higher vessels and other steel structures, while equal leg angles are the weakest sections. By dividing the buckling time by the area of the cross-section for nearly equal cross-sections for carbon steel, the results are as follows.

Table 4
Comparison of the effectiveness of different sections

	CHS	*SHS*	*equal right angle*
section	DN50	60x2.5	60x5
t/A	339.42 s/cm^2	360.69 s/cm^2	284.36 s/cm^2

Conclusions

Based on the experimental study on different leg sections of the water tank exposed to elevated temperatures, as described earlier, the following conclusions can be drawn:

- The smaller the cross-sectional view factor examined, the slower the raw material heats up. This implies that the hollow sections are more favourable than the open sections and that the rate of heating can be reduced by the application of some protective material (paintings, hollow encasement, thermal insulation, and thermally foaming paint).

- In case of buckling, it does not matter how the foot was installed; it will bend along its weakest axis. In this respect, the circular hollow sections (CHS) and square hollow sections (SHS) are the best, as these do not have protruding axes.

- In the function of the steel structure, the temperature-dependent mechanical properties vary differently. In this respect, austenitic steels are much more suitable to withstand fire loading.

- Using the mathematical model presented, we can give a very accurate prediction of the expected failure. By drawing up a protection plan, we can guarantee which protection devices are recommended for fire penetration.

Acknowledgement

References

[1]   CEN, "Eurocode 3 : Design of steel structures - Part 1-1: General rules and rules for structures," Eurocode 3, Vol. 1, No. 2005. p. 91 pp, 2005

[2]   T. Silva, M. Carić, C. Couto, P. Vila Real, N. Lopes, and D. Skejic, "Buckling Analysis of Steel Frames Exposed to Natural Fire Scenarios," Structures, Vol. 10, pp. 76-88, 2017

[3]   Z. Xing, M. Kucukler, and L. Gardner, "Local buckling of stainless steel plates in fire," Thin-Walled Struct., Vol. 148, No. November 2019, p. 106570, 2020

[4]   L. Laím, H. D. Craveiro, R. Simões, A. Escudeiro, and A. Mota, "Experimental analysis of cold-formed steel columns with intermediate and edge stiffeners in fire," Thin-Walled Struct., Vol. 146, No. February 2019, 2020

[5]   J. Yang, W. Wang, Y. Shi, and L. Xu, "Experimental study on fire resistance of cold-formed steel built-up box columns," Thin-Walled Struct., Vol. 147, No. May 2019, p. 106564, 2020

[6]   CEN, "Eurocode 3: Design of steel structures - Part 1-2: General rules - Structural fire design," Eurocode 3, Vol. 1, No. 2005. p. 20 pp, 2005

[7]   C. Zhang and A. Usmani, "Heat transfer principles in thermal calculation of structures in fire," Fire Saf. J., Vol. 78, pp. 85-95, 2015

[8]   J. Farkas and K. Jármai, Analysis and Optimum Design of Metal Structures. Rotterdam, Hollandia: Balkema Publishers, 1997

[9]   J. Farkas, "Nyomott körcsőszelvényű rúd optimális méretezése tűzállóságra," Acélszerkezetek, vol. Különszám, pp. 13-16, 2008